Stony Brook University

The Molecular Basis of Diatomic Molecule Binding by H-NOX Domains

A Dissertation Presented

by

Zhou Dai

to

The Graduate School

in Partial Fulfillment of the

Requirements

for the Degree of

Doctor of Philosophy

in

Chemistry

Stony Brook University

August 2011

Stony Brook University

The Graduate School

Zhou Dai

We, the dissertation committee for the above candidate for the

Doctor of Philosophy degree, hereby recommend

acceptance of this dissertation.

Elizabeth M. Boon - Dissertation Advisor
Assistant Professor, Department of Chemistry

Peter J. Tonge - Chairperson of Defense
Professor, Department of Chemistry

Lisa M. Miller - Third Committee Member of Defense
Biophysical Chemist, Brookhaven National Laboratory

Jennifer Bohon – Outside Committee Member of Defense
Beamline Scientist, Brookhaven National Laboratory
Instructor, Case Western Reserve University

This dissertation is accepted by the Graduate School

Lawrence Martin
Dean of the Graduate School

Abstract of the Dissertation

The Molecular Basis of Diatomic Molecule Binding by H-NOX Domains

by

Zhou Dai

Doctor of Philosophy

in

Chemistry

Stony Brook University

2011

Heme-Nitric oxide and/or OXygen binding (H-NOX) proteins are a family of recently discovered heme-based sensor proteins for diatomic molecules. Crystal structures of the H-NOX domain from *Thermoanaerobacter tengcongensis* (*Tt* H-NOX) have greatly aided the study of the molecular basis of diatomic molecule sensing by H-NOX proteins.

In our work, we employ X-ray Absorption Spectroscopy (XAS) to study the local electrostatic and structural properties of the heme-iron center in H-NOX proteins. XAS spectra of various ligands bound to H-NOX have been analyzed. The iron K-edges indicate effective charges on the iron center and report on the electronic environment of heme iron. The ligand field indicator ratio (LFIR), which is extracted from the X-ray Absorption Near-Edge Structure (XANES) analysis, provides an understanding of ligand field strength, spin state of the central iron, movement of the iron atom upon ligation, and ligand binding properties for each complex. In particular, the LFIRs demonstrate that the heme iron is dramatically displaced towards the

distal pocket when ligand binds, which is expected to be the mechanistic link between ligand binding and subsequent changes in heme and protein conformation. Furthermore, bond lengths and bond angles of the H-NOX complexes were determined by analyzing the Extended X-ray Absorption Fine Structure (EXAFS) spectra, providing detailed structural information into the heme pocket. These results are extrapolated to gain insight into changes in heme and protein conformation during a signaling event.

It is also discovered that *Tt* H-NOX can be used to selectively detect cyanide with a limit as low as 0.5 μM and an upper detection range that is adjustable with protein concentration. Engineering of the cyanide binding pocket through site-directed mutagenesis improves the detection selectivity and enables the visual detection of cyanide with this sensing system. Thus we demonstrate the ability to fine-tune the affinity and selectivity of *Tt* H-NOX for cyanide, suggesting that *Tt* H-NOX can be readily tailored into a practical cyanide sensor. Here we present our efforts to describe the molecular details that dictate small molecule sensing by H-NOX proteins.

Dedication

This dissertation is lovingly dedicated to my mother, Jianyuan Zhou, and my father, Dingqi Dai, who raised me with unconditional love. Their constant support and encouragement have sustained me throughout my life.

This dissertation is also dedicated to my wife, Ci Yang, and my lovely daughter, Angela Yang Dai, for their love, support and all the happiness they have been bringing into my life.

Table of Contents

List of Figures

List of Tables

List of Scheme

List of Equation

List of Abbreviations

– CN	nitrile
5c	5-coordinate
6c	6-coordinate
BNL	Brookhaven National Laboratory
c-di-GMP	cyclic-diguanosine monophosphate
cGMP	cyclic guanosine monophosphate
CN^-	cyanide anion
CO	carbon monoxide
DGC	di-guanylate cyclase
DTNB	5,5'-dithiobis(2-nitrobenzoic acid)
DTT	dithiothreitol
EDTA	ethylenediaminetetraacetate
EXAFS	extended X-ray absorption fine structure
Fe-Ct displacement	the movement of iron relative to the mean plane of the four porphyrin nitrogens
GTP	guanosine triphosphate
H-NOX	heme-nitric oxide and/or oxygen binding domain
HEPES	4-(2-hydroxyethyl)-1-piperazineethanesulfonic acid

IPTG	Isopropyl β-D-1-thiogalactopyranoside
IR	infrared
$KClO_4$	potassium perchlorate
KCN	sodium cyanide
L. pneumophila	*Legionella pneumophila*
LFIR	ligand field indicator ratio
MALDI	matrix-assisted laser desorption/ionization
Mb	myoglobin
MCP	methyl-accepting chemotaxis protein
MS	mass spectroscopy
MWCO	molecular weight cut off
$Na_2C_2O_4$	sodium oxalate
Na_2SO_4	sodium sulfate
NaBr	sodium bromide
NaCl	sodium chloride
NaF	sodium fluoride
NaH_2PO_4	monosodium phosphate
$NaHCO_3$	sodium bicarbonate
NaI	sodium iodide
$NaNO_3$	sodium nitrate

NaSCN	sodium thiocyanate
NaOAc	sodium acetate
NO	nitric oxide
N_p	$N_{pyrrole}$
Ns	*Nostoc sp*
NSLS	National Synchrotron Light Source
O_2	molecular oxygen
P. atlantica	*Pseudoalteromonas atlantica*
Pa	*Pseudoalteromonas atlantica*
PAS	per-arnt-sim
ppb	parts per billion
ppm	parts per million
SDS-PAGE	sodium dodecyl sulfate-polyacrylamide gel electrophoresis
sGC	soluble guanylate cyclase
SHE	standard hydrogen electrode
S. oneidensis	*Shewanella oneidensis*
S. woodyi	*Shewanella woodyi*
Sw	*Shewanella woodyi*
T. tengcongensis	*Thermoanaerobacter tengcongensis*
TNB	2-nitro-5-thiobenzoate

TOF	time of flight
Tt	*Thermoanaerobacter tengcongensis*
UV	untra-violet
V. cholerae	*Vibrio cholerae*
WT	wildtype
XANES	X-ray absorption near-edge structure
XAS	X-ray absorption spectroscopy
YC-1	3-(5'-hydroxymethyl-2' furyl)-1-benzyl indazole

Acknowledgments

This dissertation would not have been possible without the guidance and support of many people who in one way or the other have helped me during my Ph.D. study.

First and foremost, I would like to extend my utmost gratitude to my advisor, Dr. Elizabeth M. Boon, who taught me all the basic biochemistry experiment skills and guided me throughout my Ph.D. study. It is truly a privilege to work with Dr. Boon. She is knowledgeable, patient, and always ready to offer constructive advices for my research. Her enthusiasm has greatly influenced me. Without her perpetual guidance and help, I would not be able to make my way to the highest academic education level. The training and experience I had at the Boon group shall benefit me throughout my life.

Next, I want to express my sincere thanks to Dr. Peter J. Tonge, the chairperson of my dissertation committee. Dr. Tonge attended most, if not all, of my presentations, always providing valuable suggestions for my research. I also learned a lot when Dr. Tonge was helping me with the Raman project.

In addition, I would like to heartily thank Dr. Lisa M. Miller, my current third member of dissertation committee and my mentor on XANES studies, whose sincerity and kindness I will never forget.

I am also thankful to my former third member of my dissertation committee, Dr. Michelle M. Millar, who encouraged me and helped a lot in both my research and my presenting skills.

Further, I am grateful for all the support that I got from Dr. Jennifer Bohon, the outside member of my dissertation committee, who helped to set up my XAS experiment and taught me the data analysis skills.

I need to thank the X3B beamline staff at National Synchrotron Light Source at Brookhaven National Laboratory for kindly setting up the equipments for me, and especially Dr. Erik Farquhar, who also did all the EXAFS fitting for me and gave me the precious extra beamtime.

The previous and current Boon group fellows are like my brothers and sisters. We studied together, worked together, and partied together. I have got a lot of great suggestions from them. I thank for all the assistance from them in my work and in my personal life.

My very special thanks go to all my friends at Stony Brook. It is really a great honor to meet them. I feel extremely blessed and lucky to have them in my life.

Last but not least, I sincerely thank my family. Without their selfless love and constant support, I would never be able to accomplish my Ph.D. study.

Publications

Dai, Z.; Boon, E. M. Probing the Local Electronic and Geometric Properties of the Heme Iron Center in an H-NOX Domain. *J. Inorg. Biochem.* **2011**, *105*, 784-792.

Dai, Z.; Boon, E. M. Engineering of the Heme Pocket of an H-NOX Domain for Direct Cyanide Detection and Quantification. *J. Am. Chem. Soc.* **2010**, *132*, 11496-11503.

Chapter 1. Introduction

1.1. Heme-Based Sensor Proteins

The ability to respond to internal and external signals is critical for the survival of all organisms. Diatomic molecules like nitric oxide (NO), carbon monoxide (CO) and molecular oxygen (O_2) have been increasingly recognized as important signaling molecules that induce signal transduction through selectively binding with specific sensor proteins.[1-10] For example, upon the binding of NO (produced by nitric oxide synthase) to the heme domain of human soluble guanylate cyclase (sGC), the activity of sGC is enhanced by over 200-fold leading to a significant increase in the conversion from guanosine triphosphate (GTP) to cyclic guanosine monophosphate (cGMP). Through its interactions with downstream signaling systems, cGMP subsequently regulates important biological processes, such as neurotransmission, smooth muscle relaxation, and inhibition of platelet aggregation *etc.* (Figure 1-1). Malfunction of this NO-sGC signaling leads to devastating human diseases, including arterial and pulmonary hypertension, heart failure, thrombosis, erectile dysfunction as well as renal fibrosis and failure.[1,8,11] Therefore, understanding the detailed molecular mechanism of how these diatomic molecules are sensed is of crucial importance for both fundamental knowledge discovery and drug development purpose.

Hemoproteins are well suited for diatomic molecule sensing due to their binding affinity for and selectivity to these molecules. Heme-based sensor proteins can be generally classified into four distinct families on the basis of their protein scaffolds and ligand specificities. O_2 sensors like HemAT and FixL,[2-4,7] and CO sensors like CooA,[5,6] represent three of the four

hemoprotein sensor groups. Crystal structures have been solved for each of these classes of sensors. These structures have led to insight into their signaling mechanisms. The fourth group of heme-based sensor proteins are the Heme-Nitric oxide and/or OXygen binding (H-NOX) protein family,[12,13] whose members include soluble guanylate cyclase, the only confirmed eukaryotic NO sensor.

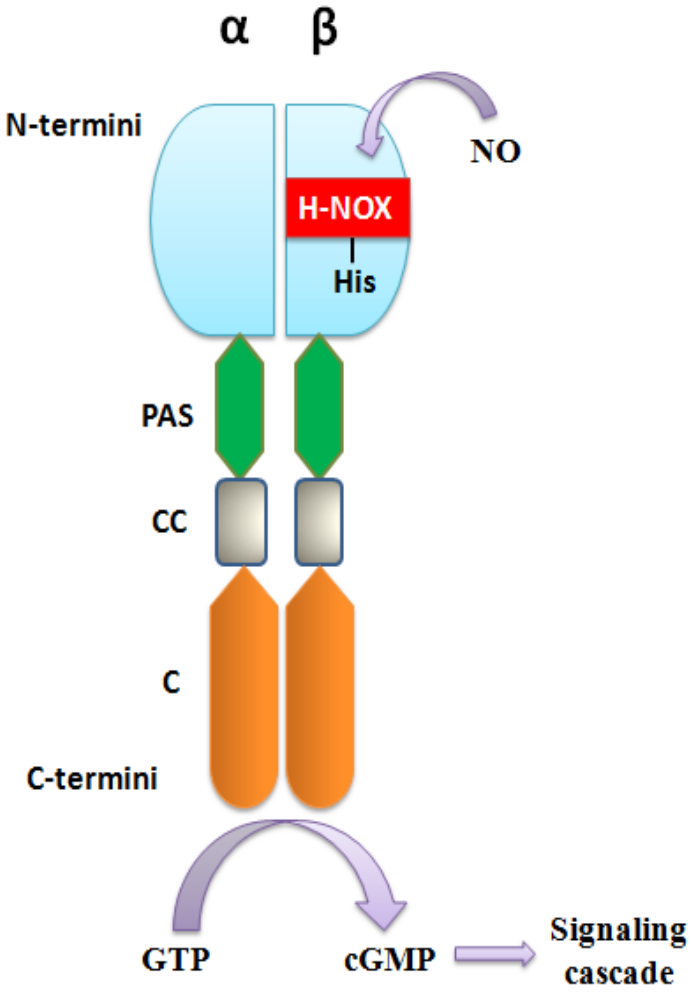

Figure 1-1. Schematic representation of sGC structure and function. The sensing N-termini of sGC are connected to the catalytic (C) C-termini through a PAS (Per-Arnt-Sim) domain and a coiled-coil (CC) domain.

Heme-based sensor proteins typically contain two distinct domains: a heme-containing sensor domain that senses O_2, CO or NO, and an effector domain that generates an output signal (usually a second messenger) and induces a downstream signal cascade.[9,10] Soluble guanylate cyclase is a heterodimeric ($\alpha1/\beta1$ or $\alpha2/\beta1$) hemoprotein (Figure 1-1).[14,15] The α and β subunits are highly homologous except that only the β subunit binds heme. Specifically, the heme-containing domain of sGC is localized to the N-terminal ~200 amino acids of the $\beta1$ subunit,[16,17] whereas the effector domain that catalyzes the production of cGMP, is located in the C-termini of both the α and β subunits.[15,18,19] It is proposed that the conformational changes caused by ligand binding at the sensing domain are transmitted to the catalytic site at the effector domain through "cross-talk" between the two domains.[15,19] As sGC activation by NO is mediated through particular interactions between NO and the heme domain, characterization of the heme environment changes in sGC upon NO binding is key to the understanding of the activation mechanism.

1.2. The H-NOX Protein Family

Critical to understanding diatomic gas sensing by hemoprotein is to determine the molecular details of gas-heme binding. Truncations of the sGC heme-containing $\beta1$ subunit, $\beta1$ (1-385) and $\beta1$ (1-194), have been characterized through multiple spectroscopic techniques.[16,17] However, despite great interest and considerable effort, there has been no success in crystallizing the heme domain of sGC to date, severely hampering understanding the NO-sGC signaling mechanism. Therefore, alternative hemoprotein model systems that can be used to probe the

molecular details of NO-sGC signaling pathway are highly desirable, and some have been identified and used for NO signaling studies.[12,13,20-27]

Primary sequence analysis has shown that the heme-containing domain of sGC shares significant homology (15-40% identity) with a recently discovered family of heme proteins in prokaryotes.[20] Based on ligand binding spectroscopic and kinetic characterization of several of these new sGC-like heme proteins, this hemoprotein family has been named H-NOX, for Heme-Nitric oxide and/or OXygen binding domain.[12] Though these prokaryotic H-NOXs are not fused to a guanylate cyclase domain like sGC, they are proposed to be also involved in essential signaling pathways within their own biological systems and recent studies support this hypothesis.[24-27]

1.3. The Function of H-NOX in Prokaryotes

The H-NOX domain widely exists in both aerobic and anaerobic bacteria (Figure 1-2). Based on analysis of bacterial genomes, H-NOX proteins in facultative aerobes are usually predicted to be isolated proteins, but found in the same operon with enzymes like di-guanylate cyclases (DGC, that catalyze the conversion of two molecules of GTP to cyclic-diguanosine monophosphate (c-di-GMP)) or histidine kinases (that catalyze protein phosphorylation), which are commonly involved in bacterial signaling pathways. For example, in *Shewanella woodyi*, an H-NOX gene is located upstream of a gene encoding a di-guanylate cyclase within the same putative operon. Recent biochemical and genomic studies in our group have suggested that NO regulates *S. woodyi* biofilm formation through binding with H-NOX. It is shown that NO modulates a protein-protein interaction of H-NOX with the DGC, thus regulating the production

of c-di-GMP. C-di-GMP is a second messenger that has been confirmed to control bacterial biofilm formation. Furthermore, NO/H-NOX regulation of biofilm formation through c-di-GMP has also been found in another facultative aerobe, *Legionella pneumophila*.[25]

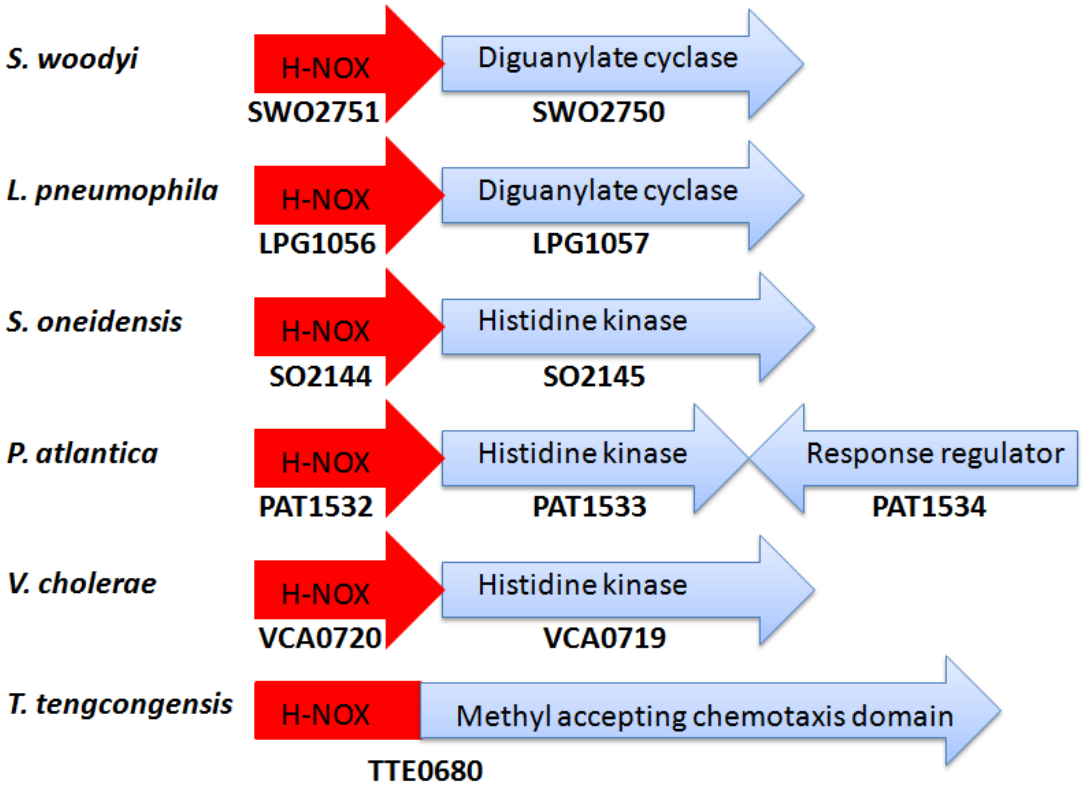

Figure 1-2. Genome organization of H-NOX proteins in prokaryotes.

Genes encoding H-NOX have also been found to be adjacent to histidine kinase genes in several bacteria (Figure 1-2). Histidine kinases are a group of enzymes central to the bacterial two-component signaling systems which typically involve a sensor-kinase protein that detects the environmental changes, and a response regulator that is usually a transcription factor regulating relevant gene transcription and protein expression. Studies on the *Shewanella oneidensis* H-NOX (SO2144) have indicated that NO bound H-NOX inhibits the kinase activity of the kinase (SO2145) adjacent to H-NOX in the genome of *S. oneidensis*.[23,26] More recently,

work on the bacterium *Pseudoalteromonas atlantica* in our group, has not only thoroughly identified the regulatory effect of H-NOX on a downstream histidine kinase, but also suggested that this H-NOX – histidine kinase interaction affects the biofilm formation of this bacterium. What is more, in the *Vibrio* species, such H-NOX – histidine kinase pairs modulate essential physiological processes like symbiotic colonization and quorum sensing.[24]

On the other hand, in obligate anaerobes like *Thermoanaerobacter tengcongensis*, H-NOX domains are fused to a methyl-accepting chemotaxis protein (MCP) through a transmembrane domain (Figure 1-2).[21] MCPs are important transmembrane receptors that detect environment stimuli and translate them into cellular signals. Even though the H-NOX regulated signaling pathways in these strict anaerobes are not clear, it is expected that these H-NOXs serve as oxygen sensors, helping to avoid high concentrations of oxygen that would be toxic to these organisms. Oxygen sensation by an H-NOX protein has already been observed in the nematode *Caenorhabditis elegans*, which serves to guide the nematode to its preferred 5-12% oxygen environment, avoiding too high or too low oxygen concentrations.[27]

As shown above, H-NOX is a newly discovered family of heme-based sensor proteins that diversely exist in eukaryotes and prokaryotes, and there has been an increasing amount of interest in uncovering the molecular mechanisms of the H-NOX signaling pathways. A thorough understanding of how small gaseous molecules are sensed by H-NOXs, and how such sensations are transmitted within the organisms and lead to physiological responses could suggest a new paradigm for signal transduction with heme-based senor proteins.

1.4. H-NOX Structure and Molecular Insights into the Roles of Essential Residues

High-resolution crystal structures of three bacterial H-NOX proteins, H-NOXs from *Thermoanaerobacter tengcongensis*, *Nostoc sp* and *Shewanella oneidensis*, have recently been solved.[12,13,22,23] This has greatly aided studies on the mechanisms of H-NOX involved signaling pathways. The availability of these crystal structures makes systematic conformational and electrostatic analysis of H-NOX protein signaling at a molecular level possible. In particular, crystal structure of the O_2-binding H-NOX domain from *Thermoanaerobacter tengcongensis* (*Tt* H-NOX) was solved to a resolution of 1.77 Å (Figure 1-3) in 2004, which has greatly boosted the progress in understanding the structure-function correlation the H-NOX family.[12] This *Tt* H-NOX structure has been widely used to model the sGC heme domain and other H-NOX proteins. These studies have identified new or confirmed previously proposed important residues/sub-domains of this protein family, and have generated a great amount of valuable molecular insights into the mechanism of H-NOX involved signaling.[15,18,22,28-30]

H-NOX protein fold and heme coordination. As seen from the crystal structure, the *Tt* H-NOX protein fold consists of seven α-helices at its N-terminus and one four-stranded antiparallel β-sheet at its C-terminus (Figure 1-3).[12] Such a protein fold is not related to any other protein families based on protein structure database search. The protoporphyrin IX heme group is tightly sandwiched in a cavity between the α-helices and β-sheet. Other than coordination with the four porphyrin nitrogens, the heme iron is ligated to His102, invariant among all H-NOX as an endogenous ligand, at the proximal side of the heme plane. Helix αF, which contains His102, is slightly strained probably due to the ligation. The distal side of heme is where the 6th (exogenous) ligand binding pocket is located. Diatomic gases (like NO, CO, O_2) bind H-NOX here to initiate signal transduction.

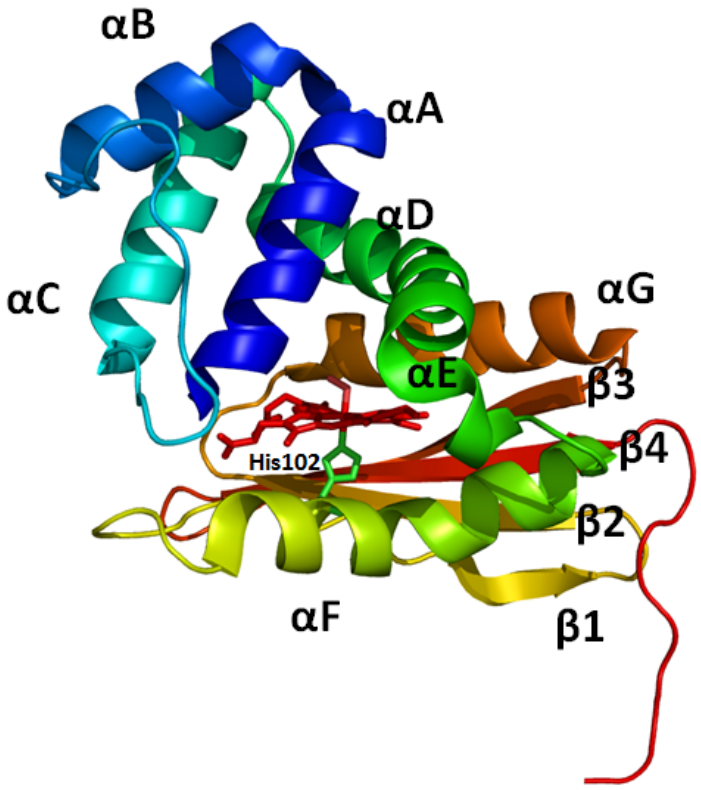

Figure 1-3. Crystal structure of wildtype (WT) *Tt* H-NOX (adapted from PDB 1U55: *Tt* H-NOX Fe(II)-O_2 complex[12]).

Ligand discrimination in H-NOX proteins. Ligand discrimination by H-NOX proteins is of fundamental importance for the sensing of correct physiological signals. Nature has taken millions of years to tune the ligand binding specificities of H-NOX proteins. A significant difference between the H-NOXs from facultative aerobes and those from obligate anaerobes lies in their ligand specificity. In facultative aerobes like *S. woodyi* and *P. atlantica*, H-NOX proteins bind NO and CO, but do not bind O_2. This ligand binding feature is the same as sGC. Yet in obligate anaerobes like *T. tengcongensis*, H-NOX not only binds NO and CO, but also shows high affinity for O_2.[21] The fact that the H-NOX family uses the same protein fold to bind NO and exclude O_2 in some members, while binding O_2 very tightly in other members, makes H-NOX a

unique heme sensor system with intriguing ligand discrimination properties. Such ligand selectivity is essential for the NO-specific sGC activation, as sGC needs to discriminatively sense a physiological NO concentration of ~10 nM in the presence of 20-40 μM intracellular O_2.

In the crystal structure of ferrous-oxy complex of *Tt* H-NOX, Tyr140 forms 2.74 Å H-bond with the bound O_2, and distal pocket residues Asn74 and Trp9 are involved in a H-bond network with the same hydroxyl group of Tyr 140 (Figure 1-4A); such a H-bonding system was proposed to be important for stable O_2 binding to H-NOX proteins.[21] Sequence alignments support this idea because these three residues only exist in obligate anaerobic H-NOXs, such as *Tt* H-NOX which has been shown to bind O_2. In order to further confirm the role of Tyr140 in O_2 binding, mutagenesis studies were performed. It was shown that the O_2 binding properties are largely altered in the *Tt* H-NOX Y140L mutant. Restoration of a distal pocket tyrosine by making the Y140L/F78Y double mutant rescues the O_2 binding of *Tt* H-NOX (F78 is located at a reasonable position for H-bond in the distal pocket).[18,28,29] These results demonstrate that the lack of a H-bond donor residue (like tyrosine) in the distal pocket of sGC is a key factor for it to discriminatively sense picomolar NO even in the presence of micromolar O_2. Subsequent studies have shown that, besides this H-bond network, distal pocket bulkiness and domain interactions between H-NOX and the rest of sGC are also contributing to the ligand discrimination.[31]

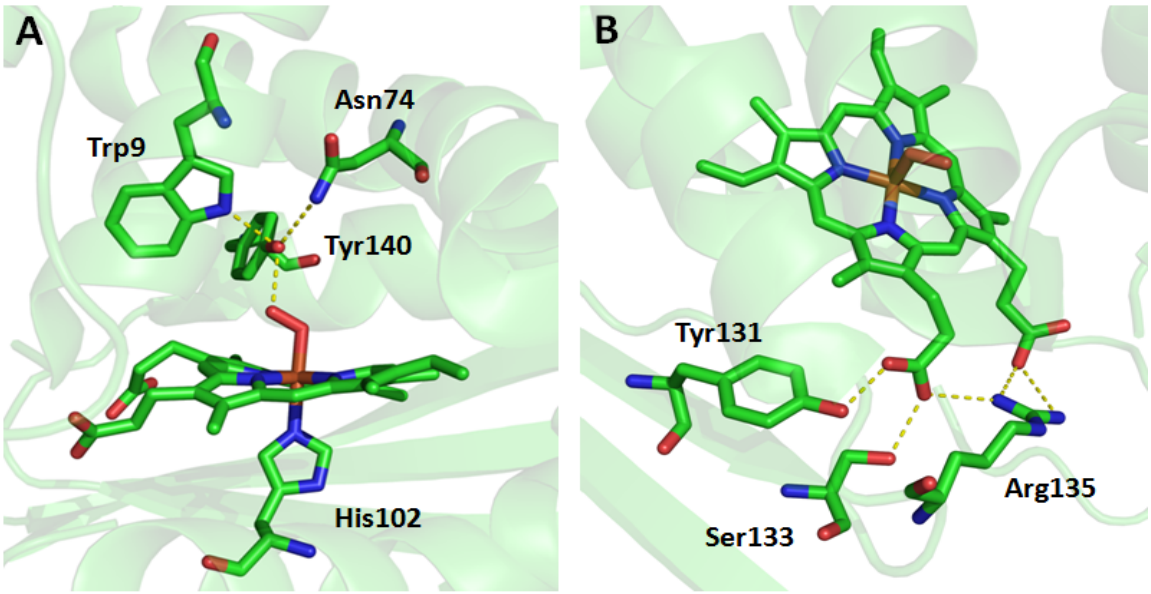

Figure 1-4. Important residues at the heme pocket of *Tt* H-NOX.

Protoporphyrin heme - protein matrix interactions and sGC activation. In the H-NOX domain, the propionate side chains of the heme are buried in the protein and intimately interact with the surrounding residues, anchoring the heme inside the protein matrix. Along the propionate groups, Tyr131, Ser133 and Arg135 together form a conserved Y-S/T-R motif among all H-NOX proteins. These residues build up a complex H-bonding network with carboxylate groups from propionate side chains as shown in Figure 1-4B.[12] This network has been reported to be important for heme binding in human sGC as well as for transmitting changes in heme electronics and geometry to sGC conformation during enzyme activation.[32]

In addition, during sGC activation, the Fe-histidine bond breaks upon NO binding to sGC; this has been proposed to be an essential step for the signal initiation.[33] Though NO binding to *Tt* H-NOX does not lead to Fe-His bond breakage, it is expected that this binding greatly lengthens the Fe-His bond, causing a conformational change to the αF helix as well as a rearrangement of the N-terminal subdomains. The synergism of all these interactions is key to

the communication between heme properties and H-NOX protein conformation which plays fundamental role in the H-NOX signal transduction.

1.5. Heme Distortion and Heme-Driven Protein Conformational Changes

Tt H-NOX wildtype O_2-bound complex has been crystallized in two different crystal forms, orthorhombic and monoclinic, with two molecules per asymmetric unit in both crystal forms, yielding four independent views of the protein.[12] One of the particularly striking features of the H-NOX fold revealed by these structures is the severe distortion in the protoporphyrin IX heme group. Three of the four structures have non-planar heme groups with approximately -1 Å saddling and -1.2 Å ruffling. The fourth molecule, however, has only approximately -0.7 Å displacement for both saddling and ruffling. The severely distorted heme structure, combined with the flexibility in the heme conformation reflected from the crystal structures, implies that changes in heme planarity could be critical for heme functioning and heme-driven conformational changes to the whole H-NOX domain.

The involvement of heme conformational changes in hemoprotein functioning is not a new idea. Cytochrome c complexes isolated from various species have almost identical non-planar heme structures, suggesting a unique role for that specific heme distortion.[34] Besides, for the oxygen sensor FixL, changes in heme planarity caused by O_2 binding have been implicated in the signaling mechanism.[4] Therefore, H-NOX involved signaling may be different in terms of initial ligand discrimination, downstream coupling effector proteins and eventual physiological responses, but it is likely that they all share heme distortion and heme-driven protein conformational changes as common steps in respective signaling pathways.

Energy minimizations predict that there are mainly two structural elements of *Tt* H-NOX protein matrix contributing to the severe heme distortion.[12] While one of them involves the Y-S/T-R conserved motif which forms a network of H-bonding with the propionate side chains of the heme group as mentioned above, the other important structural factor that leads to heme deformation comes from the packing of several hydrophobic residues at the heme pocket, including Ile5, Pro115 and L144, all of which are highly conserved among H-NOX proteins (Figure 1-5A). These hydrophobic residues locate very closely to the heme plane and have been suggested to be primarily responsible for forcing the heme into its strained conformation in *Tt* H-NOX.

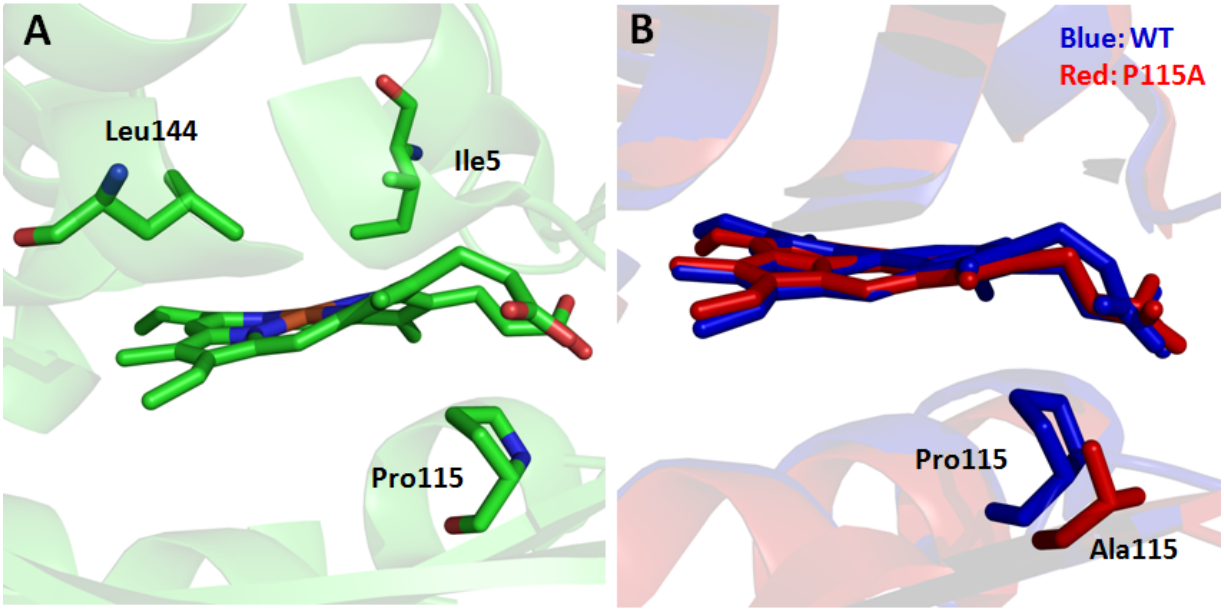

Figure 1-5. Heme distortion in *Tt* H-NOX. A. Residues Ile5, Pro115 and L144 pack against the heme and generate a great heme distortion; B. Removal of the bulky side chain of Pro115 leads to a significant heme flattening and relaxation.

Indeed, subsequent structural and spectroscopic characterizations have confirmed the importance of these closely packed hydrophobic residues, among which the role of Pro115 is

best characterized.[35-39] Crystallographic characterization of the O_2-bound *Tt* H-NOX P115A mutant revealed significant heme relaxation in this mutant (Figure 1-5B). In particular, *Tt* H-NOX P115A crystallized with four different molecules in the unit cell. Two of the four structures have significantly flatter heme structure than wildtype, with approximately 0 Å saddling and -0.5 Å ruffling; the other two molecules are flatter than wildtype, but not dramatically so, with approximately -0.4 Å saddling and -0.6 Å ruffling each.[37] Besides, solution resonance Raman spectra of *Tt* H-NOX mutants, I5L, P115A and I5L/P115A, have also suggested a significant relaxation in the heme plane as compared to WT. The broadening of several vibration modes at high frequency in the resonance Raman spectra implies the heme conformation heterogeneity which agrees well with the existence of multiple molecules in the crystal structures, demonstrating the increased flexibility and dynamic feature of H-NOX protein conformation in the mutants.[38] Furthermore, it was also found that there are dramatic changes in the reduction potential and ligand binding affinity upon the P115A mutation, as well as a shift in the conformation of the N-terminal region of the protein.[35-37] These results suggest that while H-NOX heme structure is dynamic, there is a clear link between heme conformation and *Tt* H-NOX structure, and that heme distortion is an important determinant for maintaining biochemical properties in H-NOX proteins.

The results obtained with P115A *Tt* H-NOX have led to a hypothesis that changes in heme structure are responsible for initiating signaling in the H-NOX family of proteins. Although it is commonly observed that ligand binding causes heme distortion and protein conformational changes in heme proteins,[12,30,40] the molecular details of how ligand binding, the initial step in signal induction, leads to heme and protein structural changes in H-NOX has not been established. Understanding the molecular impacts of ligand binding is critical to developing

a full understanding of signal transduction in this important family of heme sensors. Therefore, my research is focused on identifying the signaling molecule ligation-induced molecular factors that dictate conformational and electronic changes to the heme group and the whole H-NOX domain.

1.6. Overview of Research Projects Included in this Dissertation

In Chapter 2 to Chapter 4, X-ray Absorption Spectroscopy (XAS) studies of H-NOX proteins will be thoroughly discussed. Specifically, in Chapter 2, X-ray Absorption Near-Edge structure (XANES) spectroscopy of *Tt* H-NOX is analyzed for ferrous and ferric complexes of the protein. This work provides specific structural characterization of the solution state of several *Tt* H-NOX ferrous complexes (-unligated, -NO, and -CO) that were previously unavailable. The iron K-edges indicate effective charge on the iron center in the various complexes and report on the electronic environment of heme iron. We analyzed the ligand field indicator ratio (LFIR), which is extracted from XANES spectra, for each complex, providing an understanding of ligand field strength, spin state of the central iron, movement of the iron atom upon ligation, and ligand binding properties. In particular, our LFIRs indicate that the heme iron is dramatically displaced towards the distal pocket during ligand binding. Based on these results, we propose that iron displacement towards the distal heme pocket is an essential step in signal initiation in H-NOX proteins. This provides a mechanistic link between ligand binding and the changes in heme and protein conformation that have been observed for H-NOX family members during signaling.

In Chapter 3, we focus on using the Extended X-ray Absorption Fine Structure (EXAFS) analysis to obtain structural details of the heme pocket for the Fe(II)-unligated and Fe(II)-NO

complexes of H-NOX proteins from *Thermoanaerobacter tengcongensis* (*Tt* H-NOX), *Shewanella woodyi* (*Sw* H-NOX), and *Pseudoalteromonas atlantica* (*Pa* H-NOX). It was found that NO binds to *Tt* H-NOX in a 6-coordinate manner, and to *Sw* H-NOX and *Pa* H-NOX in a 5-coordinate manner with the proximal histidine dissociated, which is exactly the same as that for sGC. In the *Tt* H-NOX Fe(II)-NO complex, the Fe-histidine bond is substantially lengthened although it is not broken. This coordination chemistry has also been confirmed by their UV/visible spectra and iron K-edge values. On the basis of detailed EXAFS fitting for all three H-NOX Fe(II)-unligated complexes, we noticed a ~0.07 Å shortening in the Fe-N_p bond lengths upon NO binding; such a contraction in Fe–N_p bond lengths could be important for the signal initiation step of NO sensing.

In Chapter 4, we use *Tt* H-NOX as a hemoprotein model system to identify how the conformation and properties of heme cofactor are affected. In this work, we performed EXAFS structural analysis and ligand binding characterization to *Tt* H-NOX wildtype and P115A mutant. Results show that P115A mutation leads to a significant change to the iron-ligand bond lengths in Fe(III)-H_2O complex causing an increased electron density on heme iron, which makes the *Tt* H-NOX water-complex exit as Fe(III)-H_2O in P115A as compared to Fe(III)-OH^- in WT. While for ferrous complexes, the heme coordinations are relatively similar between WT and P115A. This finding provides molecular basis for the greater changes in ferric *Tt* H-NOX that have been observed before. Furthermore, our data illustrates how protein matrix and heme ligation state modulate heme structure and properties, and how these modulations affect hemoprotein functionalities.

In Chapter 5, we explore the potential of using *Tt* H-NOX as a new cyanide sensing system. With straightforward UV/vis absorbance-based detection, we have achieved a cyanide

detection limit of 0.5 μM (~10 ppb) with an upper detection range that is adjustable with protein concentration. We find a linear correlation of multiple spectroscopic features with cyanide concentration. These spectroscopic features include the Soret band maximum and absorbance changes in both the Soret and α/β band regions of the spectrum. Multiple probes for cyanide detection make sensing with *Tt* H-NOX unique compared to other cyanide sensing methods. Furthermore, using site-directed mutagenesis, we have rationally engineered the heme pocket of *Tt* H-NOX to improve its cyanide sensing properties. We were able to introduce colorimetric detection and enhance anion selectivity in P115A *Tt* H-NOX. Through substituting phenylalanine 78 with a smaller (valine, F78V) or a larger residue (tyrosine, F78Y), we demonstrate a correlation with distal pocket steric crowding and affinity for cyanide. In particular, F78V *Tt* H-NOX shows a significant increase in CN^- binding affinity and selectivity. Thus, we demonstrate the ability to fine-tune the affinity and specificity of *Tt* H-NOX for cyanide, suggesting that *Tt* H-NOX can be readily tailored into a practical cyanide sensor.

In Chapter 6, we explore the potential of using a nitrile group (–CN) to probe the electrostatic environment changes to H-NOX proteins during a signaling event. So far, we have successfully introduced the nitrile group into *Tt* H-NOX proteins and have detected an IR signal of the –CN group. The IR spectra of –CN modified protein complexes show the nitrile stretch at 2152 cm^{-1}. However, we did not observe a signal shift in the –CN IR absorption when we further introduced the P115A mutation. This is likely because either P115A does not cause a significant change to the electrostatic environment of heme pocket as evidenced from the resonance Raman and XANES results, or Met98 is not an appropriate site for incorporating the nitrile stretch. Further studies include rationally selecting sites for nitrile introduction and/or inducing a larger electrostatic change in H-NOX, so that the –CN probe can sensitively pick up electric field

changes in the protein. Once the technique of –CN incorporation into H-NOX is optimized, we will use it to study the heme electric field changes caused by the binding of signaling molecules as well as downstream signal transduction.

Chapter 2. XANES Studies on the Local Electronic and Geometric Properties of *Tt* H-NOX

Abstract: Heme-Nitric oxide and/or OXygen binding (H-NOX) proteins are a family of diatomic gas binding hemoproteins that have attracted intense research interest. Here we employ X-ray absorption near-edge structure (XANES) spectroscopy to study the nitric oxide (NO) binding site of H-NOX. This is the first time this technique has been utilized to examine the NO/H-NOX signaling pathway. XANES spectra of wildtype and a point mutant (proline 115 to alanine, P115A) of the H-NOX domain from *Thermoanaerobacter tengcongensis* (*Tt* H-NOX) were obtained and analyzed for ferrous and ferric complexes of the protein. This work provides specific structural characterization of the solution state of several *Tt* H-NOX ferrous complexes (-unligated, -NO, and -CO) that were previously unavailable. Our iron K-edges indicate effective charge on the iron center in the various complexes and report on the electronic environment of heme iron. We analyzed the ligand field indicator ratio (LFIR), which is extracted from XANES spectra, for each complex, providing an understanding of ligand field strength, spin state of the central iron, movement of the iron atom upon ligation, and ligand binding properties. In particular, our LFIRs indicate that the heme iron is dramatically displaced towards the distal pocket during ligand binding. Based on these results, we propose that iron displacement towards the distal heme pocket is an essential step in signal initiation in H-NOX proteins. This provides a mechanistic link between ligand binding and the changes in heme and protein conformation that have been observed for H-NOX family members during signaling.

2.1. Introduction

Soluble guanylate cyclase is a heterodimeric heme sensor responsive to nitric oxide, an important signaling molecule in eukaryotic organisms.[1,11,41,42] The heme-binding domain of sGC has been localized to the N-terminal ~200 amino acids of its β subunit.[16,43] This heme domain shares significant homology (15-40% identity) with a recently discovered family of heme proteins in prokaryotes.[12,18,29] Based on spectroscopic and kinetic characterization of several of these new sGC-like heme proteins,[21,22,28,44] this family has been named H-NOX, for Heme-Nitric oxide and/or OXygen binding domain. Although sGC and other H-NOX family members have been the subject of intense investigation,[1,11,12,16,18,21,22,28,29,37,38,41-45] the molecular details of the H-NOX involved signaling mechanism are currently unclear.

The structure of the H-NOX domain from *Thermoanaerobacter tengcongensis* was solved to a resolution of 1.77 Å (Figure 2-1) [12] with a particularly striking feature that the protoporphyrin IX heme group in the H-NOX is severely distorted. Energy minimizations predict proline 115, invariant among H-NOX proteins, to be primarily responsible for forcing the heme into its strained conformation.[12] Indeed, crystallographic characterization of the *Tt* H-NOX P115A mutant revealed significant heme relaxation in this mutant.[37] Spectroscopic and structural studies of *Tt* H-NOX, however, indicate that the heme is quite flexible and can likely assume more than one solution conformation in both wildtype and the P115A mutant.[12,37]

A prevalent hypothesis of H-NOX signaling is that changes in heme structure are responsible for initiating signal transduction in the H-NOX family of proteins. However, because the crystal structure of ferrous-unligated protein complex has not been solved for *Tt* H-NOX, previous studies have focused on the changes in heme structure that are caused by the P115A mutation, as opposed to changes to heme structure that are caused by ligand binding. Although it

is commonly observed that ligand binding causes heme distortion and protein conformational changes in heme proteins,[12,30,40] the molecular details of how ligand binding, the initial step in signal induction, leads to heme and protein structural changes in H-NOX has not been established. Understanding the molecular impacts of ligand binding is critical to developing a full understanding of signal transduction in this important family of heme sensors.

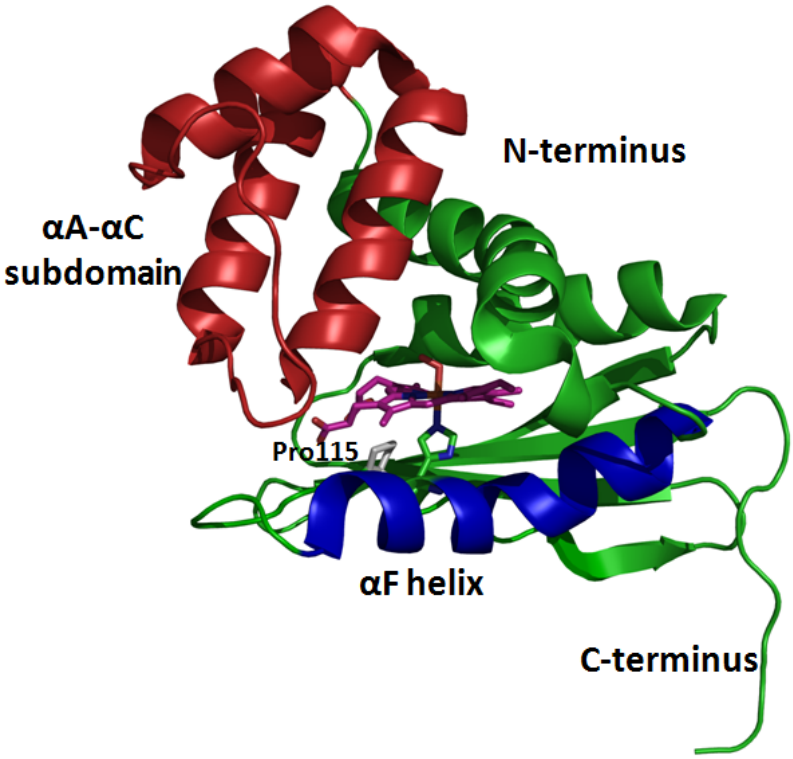

Figure 2-1. Structure of wildtype *Tt* H-NOX (figure was generated using PDB 1U55: Fe(II)-O_2 complex, resolution 1.77 Å).[12] The heme is shown in purple while proline 115 is shown in gray. The αA-αC subdomain and αF helix are color coded in red and blue, respectively.

In this work, X-ray absorption spectroscopy (XAS) is employed, for the first time, to explore the role of ligand binding on heme conformation and electronic structure during signal initiation in the H-NOX family. Although crystal structures are critical for understanding protein

conformation and function, they do not always accurately represent the solution state. XAS reveals the local solution structure of the X-ray absorbing atom. Thus it is used to confirm and correct available crystal structures as well as to characterize species for which crystallography data is not yet available. The XAS spectrum of a metalloprotein provides information about metal oxidation state, metal spin state, the number and type of ligands bound to the metal, and metal-ligand bond lengths; as such, XAS has been widely used to examine the solution-state structure of metal centers in numerous metalloproteins.[46-51] In order to study the effect of heme conformation on H-NOX signaling, we use XAS to obtain accurate and precise changes to the heme pocket caused by ligand binding.

There are generally three important features in a typical X-ray absorption spectrum: the edge, the X-ray Absorption Near-Edge Structure (XANES) region and the Extended X-ray Absorption Fine Structure (EXAFS) region as shown in Figure 2-2. Specifically for hemoproteins, the position of the X-ray absorption iron K-edge, which represents the excitation energy of the core shell (1s) electron, is determined by the maximum of the first derivative spectrum. It is directly related to the oxidation state of the iron in the protein and can indicate the flow of electron density between the metal center and surrounding ligands. Higher oxidation states have higher X-ray edges, due to an increase in the core shell electron binding energy. For example, met-Mb [Fe(III)] has an X-ray edge that is ~4 eV higher than deoxy-Mb [Fe(II)].[51] The iron K-edge 1s to 3d pre-edge features have also been shown to vary with oxidation state, spin state and centrosymmetry of the heme iron center.[52-54]

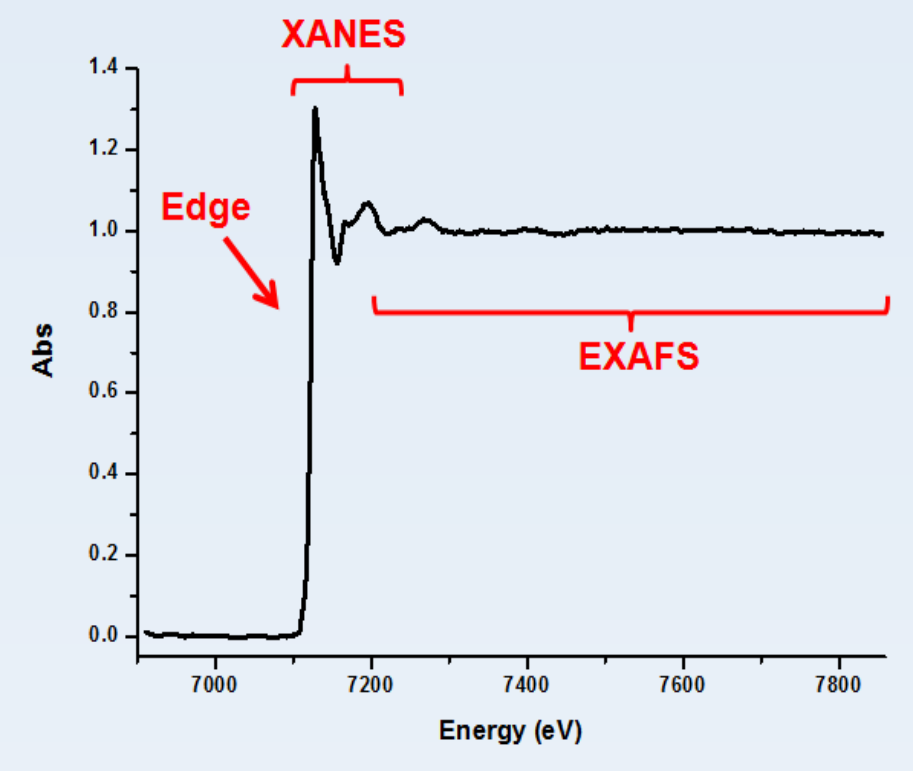

Figure 2-2. X-ray absorption spectrum of an H-NOX protein. A typical XAS spectrum includes three key regions: the Edge, the XANES region and the EXAFS region.

The XANES region of a XAS spectrum is highly predictive of the local environment of the X-ray absorbing atom. The ligand field indicator ratio (LFIR) is an empirical number that is extracted from the XANES region at about 30-100 eV above the K-edge. LFIR analysis of XANES spectra was developed about 25 years ago using hemoproteins.[47] Here we reintroduce it as a powerful method to analyze changes in heme structure and electronics upon ligation. LFIR is correlated with the magnetic susceptibility, an indicator of the spin state, and with metal-heme displacement.[47,50,51] Metal-heme displacement is an important parameter in heme conformation, which has implications in determining the conformational state of the entire protein. LFIR analysis is especially useful for studying changes in metal position among closely related porphyrin species (e.g., various complexes of the same protein or wildtype and mutant proteins),

as demonstrated in this work. In addition, the development of XANES theory is still in progress, procedures like *MXAN* have been used to model the XANES near-edge features of heme-iron and explore the heme pocket structure of hemoproteins.[48,55,56] Lastly, the EXAFS region provides detailed geometric information on the coordination environment of the heme iron, which will be discussed in following chapters.

Here, we present a XANES study on the local electronic and geometric properties of the heme-iron in *Tt* H-NOX WT and P115A mutant proteins in a variety of Fe(II) and Fe(III) complexes. The solution states of several key *Tt* H-NOX ferrous compounds (-unligated, -NO, and -CO), which have not been crystallographically studied, were characterized detailing their structural and electronic features. The X-ray absorption edge of each complex is determined, indicating the effective charge on the iron center. We focus on LFIR analysis to obtain electronic and structural information such as ligand field strength, spin state of the central iron, and movement of the iron upon ligand binding. This information is extrapolated to gain insight into changes in heme distortion and protein conformational change upon heme ligation during a signaling event.

2.2. Materials and Methods

Plasmid preparation and protein expression. Cloning of the *Tt* H-NOX domain into a pET-20b (Novagen) vector has been described previously.[21] For ease of purification, a C-terminal 6×His tag was incorporated to the plasmid ahead of the stop codon. P115A mutagenesis of the 6×His tagged protein construct was carried out using the QuikChange® protocol from Stratagene. Cell culture preparation and expression procedures of H-NOX proteins were carried

out as previously described,[21] except that upon induction with Isopropyl β-D-1-thiogalactopyranoside (IPTG), overnight protein expression took place at 18 °C.

Protein purification. Cell lysis and thermal denaturation treatments were carried out as described.[21] The supernatant after thermal denaturation was filtered through a 0.45 µm membrane and the filtrate was applied to a 1 mL HisTrap HP column (GE Life Sciences) pre-equilibrated with buffer A [50 mM sodium phosphate, 300 mM NaCl, pH 7.5]. The column loaded with *Tt* H-NOX was washed using 30 mL buffer A and then three more washes were performed using 20 mL buffer A with 10 mM imidazole, 20 mL buffer A with 20 mM imidazole, and 10 mL buffer A with 50 mM imidazole. The protein was ultimately eluted using buffer A with 250 mM imidazole. The flow rate was controlled at 1 mL/min. The protein was then exchanged into buffer B [50 mM HEPES, 50 mM NaCl, 5% glycerol and 5 mM DTT, pH 7.5] using a PD-10 column (GE Healthcare), aliquoted, and stored at -80 °C. This procedure (thermal denaturation plus affinity chromatography) resulted in protein that was >95% pure as estimated by SDS-PAGE.

Electronic spectroscopy. All UV/visible spectra were recorded on a Cary 100 Bio spectrophotometer equipped with a constant temperature bath set to 20 °C. Preparation of ferrous complexes was carried out as previously published.[21] Ferric complexes were prepared as described below.

XAS sample preparation. Ferrous (-unligated, -O_2, -CO, and -NO) complexes of H-NOX were prepared in the glove bag as previously described.[21] The Fe(III)-H_2O complex was prepared by oxidizing the protein sample with 10-20 mM potassium ferricyanide followed by desalting with a PD-10 column. Addition of ~50 mM of KCN to the Fe(III)-H_2O complex produced the

Fe(III)-CN^- complex. Protein samples were exchanged into buffer C [50 mM HEPES, 50 mM NaCl, 10% glycerol, pH 7.5] and concentrated to 1-2 mM using spin columns from Millipore [Microcon Ultracel YM-3, 3000 molecular weight cut off (MWCO) and 0.5 mL maximum volume]. The concentrated protein samples were transferred to copper sample holders with Mylar windows (10 mm wide × 5 mm high × 0.5 mm thick), frozen in liquid nitrogen and stored at -80 °C before XAS experiments.

X-ray absorption spectroscopy. XAS data collection was carried out at the National Synchrotron Light Source (NSLS) at Brookhaven National Laboratory (BNL), on beamline X3B with a sagittally focused Si (111) crystal monochromator. Samples were cooled to at least 40 K before scanning in a closed-cycle liquid helium diplex and kept frozen during data collection. K_α fluorescence was detected with a Canberra 13-element germanium detector. An iron foil was used as a reference to determine the X-ray absorption edge for each spectrum and to account for any shifts in the monochromator. The step size at the edge region was set to 0.2 eV. 4-6 scans for each sample were taken and averaged for data analysis. In all cases, the first and last scans overlap well, which indicates that X-ray damage was insignificant. Furthermore, as we collected data only in the XANES region, the amount of time the samples were exposed to the X-ray beam was relatively short. XAS data were aligned and merged using Athena. The K-edge positions were determined from the first derivative of the average XANES spectra after smoothing. The derivative spectra were smoothed using Origin 7.0. In order to extract the ligand field indicator ratios, Origin 7.0 was used to smooth the averaged XANES spectra and OMNIC was applied subsequently to determine the height of the two peaks as described.[51]

Cyanide association kinetics. All kinetic studies were performed in buffer D [50 mM HEPES, 50 mM NaCl, pH 7.5]. Cyanide (CN^-) association to the ferric heme was measured

using stopped-flow (for *Tt* H-NOX WT) or scanning kinetics (for *Tt* H-NOX P115A) at 20 °C. For *Tt* H-NOX WT, stopped-flow data were acquired on an Applied Photophysics SX 18MV stopped-flow spectrophotometer equipped with a constant temperature bath set to 20 °C. Difference absorption spectra of *Tt* H-NOX WT were collected at 424 nm with various cyanide concentrations (0.45-18.16 mM). We collected at least 3 scans for each cyanide concentration. The average difference spectrum was fitted to a single-exponential curve to give observed association rate constant k_{obs}. k_{obs} values were then plotted versus corresponding cyanide concentrations, and the slope of the line revealed the association rate constant (k_{on}) for WT *Tt* H-NOX.

For *Tt* H-NOX P115A, scanning kinetics data for various cyanide concentrations (10 mM to 100 mM) were acquired on a Cary 100 Bio spectrophotometer with temperature control set to 20 °C. Each scan started at 480 nm and ended at 370 nm with a 600 nm/min scanning rate and a 1 nm step size. Difference spectra were calculated by subtracting the first scan (t = 0 min) from each subsequent scan. The maximal change of each difference spectrum as a function of time was fitted to a single-exponential curve to generate the k_{obs}, which was subsequently used to calculate k_{on} for *Tt* H-NOX P115A as was described for wildtype.

2.3. Results

UV/visible spectroscopy. UV/visible spectra of each sample were obtained before XAS sample preparation to confirm the ligand binding states (Figure 2-3). The Soret and α/β bands absorption maxima are listed in Table 2-1. Electronic spectra of the *Tt* H-NOX WT and P115A Fe(II) complexes (-unligated, -CO, -O_2, and -NO) have been reported previously.[21,38] Here we

also present the spectra for Fe(III) complexes (-H_2O and -CN^-) of *Tt* H-NOX WT and the P115A mutant.

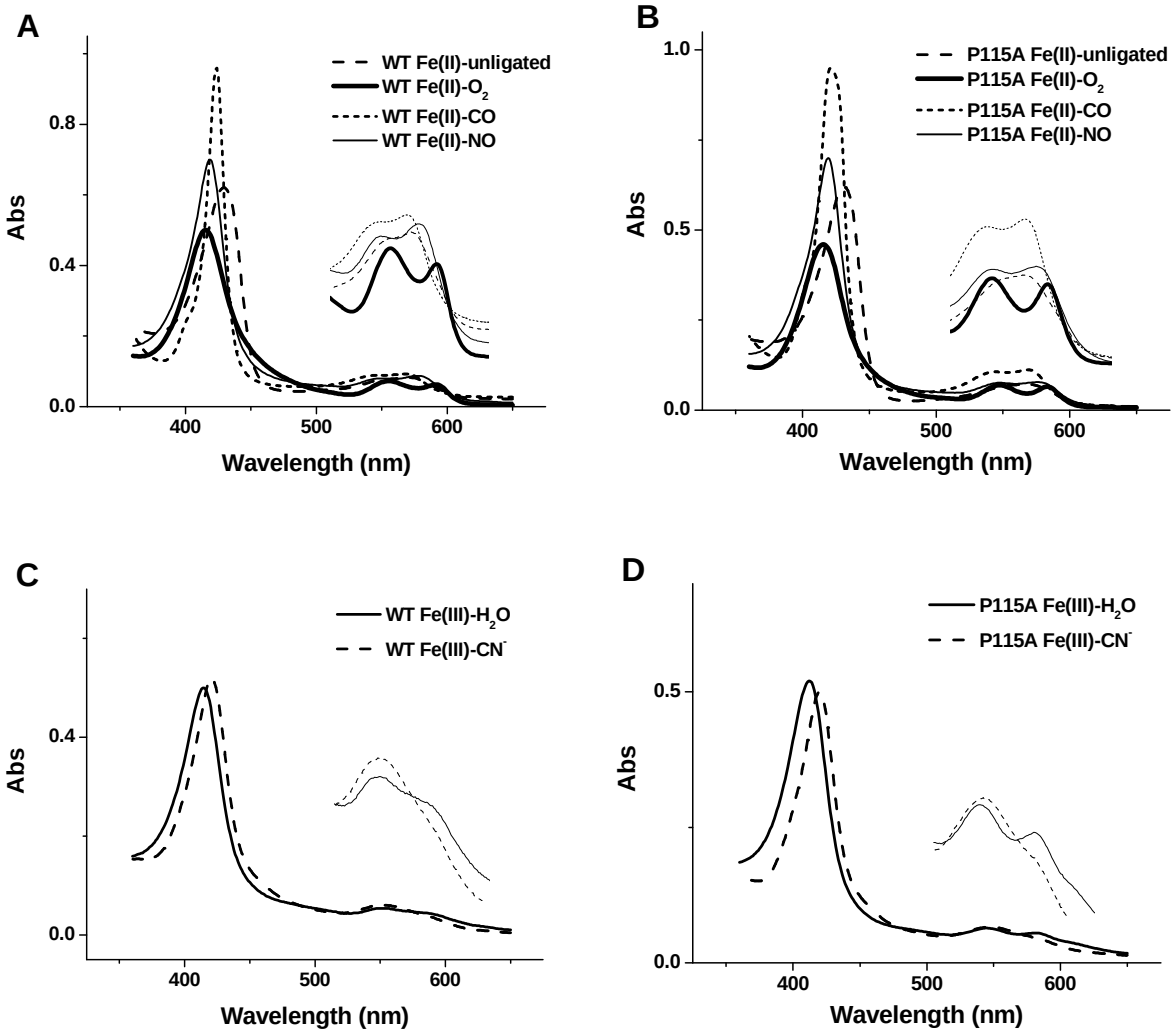

Figure 2-3. UV/visible spectra of WT and P115A *Tt* H-NOX complexes. Electronic spectra for (A) WT and (B) P115A H-NOX ferrous complexes: Fe(II)-unligated (dash), Fe(II)-O_2 (thick solid), Fe(II)-CO (dot), Fe(II)-NO (solid). Spectra for (C) WT and (D) P115A *Tt* H-NOX ferric complexes: Fe(III)-H_2O (solid), Fe(III)-CN^- (dash). Insets show enlarged spectra of the α/β bands area.

Table 2-1. Soret and α/β band absorption maxima of various *Tt* H-NOX complexes (unit: nm).

	Soret	β	α
WT Fe(II)-unligated	429	560	
WT Fe(II)-CO	424	545	568
WT Fe(II)-NO	419	547	577
WT Fe(II)-O_2	415	555	591
WT Fe(III)-H_2O	415	552	587
WT Fe(III)-CN^-	421	550	-
P115A Fe(II)-unligated	431	561	
P115A Fe(II)-CO	423	544	568
P115A Fe(II)-NO	419	547	577
P115A Fe(II)-O_2	415	547	583
P115A Fe(III)-H_2O	405	545	581
P115A Fe(III)-CN^-	420	550	-

As shown in Figure 2-3 and Table 2-1, our electronic spectra results are the same as those published for the ferrous complexes of *Tt* H-NOX WT and P115A.[21,38] In the ferric oxidation state, water-bound [Fe(III)-H_2O] *Tt* H-NOX WT exhibits a Soret band maximum at 415 nm and split α/β bands at 587 nm and 552 nm. Water-bound *Tt* H-NOX P115A exhibits a Soret band maximum at ~405 nm and split α/β bands at 581 nm and 545 nm, representing a blue shift of ~7 nm from those for WT, an indication of the change in heme structure and electronic environment induced by the mutation. Addition of CN^- replaces water from the binding pocket and produces the Fe(III)-CN^- complex, giving a Soret band maximum at ~421 nm for both WT and P115A. The α bands for Fe(III)-CN^- complexes diminish to a shoulder on the β bands at ~550 nm. Overall, we observe minor changes in the electronic spectra of these ferric complexes upon the P115A mutation, which is consistent with what has been observed for the ferrous complexes.[38]

K-edge absorption energy. We obtained XAS spectra for each ferrous (-unligated, -O_2, -NO, -CO) and ferric (-H_2O, -CN^-) complex of both WT and P115A *Tt* H-NOX. In addition, as controls, we collected spectra for Fe(II) (-unligated, -O_2, -CO) and Fe(III)-H_2O complexes of Mb (Figure 2-4).

A summary of iron K-edge absorption energies is presented in Table 2-2. Determined by the maximum of the derivative XAS spectrum, the X-ray absorption iron K-edge represents the excitation energy of the 1s core shell electron. All edge energies obtained for Mb are within error of those published.[51] Among all *Tt* H-NOX WT complexes, the Fe(II)-unligated compound, as expected, has the lowest edge energy at 7124.1 eV, since it has the lowest effective charge on heme iron. Binding of CO and NO to the ferrous heme leads to an increase of 1.4 eV in each edge position. When O_2 binds, the edge shifts from 7124.1 eV to 7126.5 eV, indicating more extensive electron flow from iron to O_2 (or the histidine or heme ligands). Ferric state complexes generally have higher energy edge positions than ferrous species, due to greater charges on the heme iron. The *Tt* H-NOX WT Fe(III)-CN^- complex has a slightly larger edge than WT Fe(III)-H_2O. When comparing the edge values of WT and P115A, we can see that *Tt* H-NOX P115A complexes edge positions are generally similar with those of WT species, and they follow the same trend: Fe(II)-unligated < Fe(II)-CO ~ Fe(II)-NO < Fe(II)-O_2 ~ Fe(III)-H_2O < Fe(III)-CN^-.

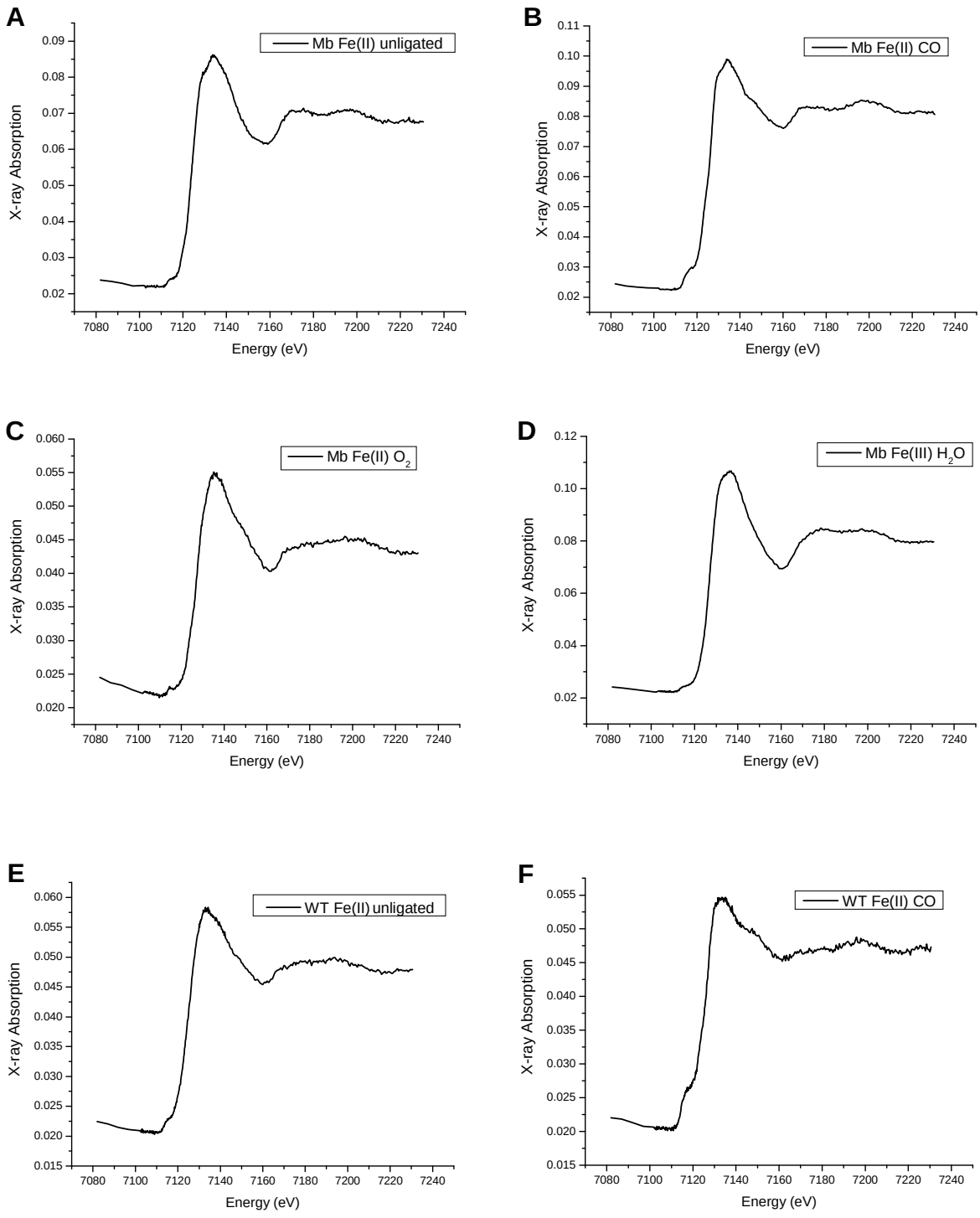
A
Mb Fe(II) unligated
X-ray Absorption
Energy (eV)
B
Mb Fe(II) CO
X-ray Absorption
Energy (eV)
C
Mb Fe(II) O2
X-ray Absorption
Energy (eV)
D
Mb Fe(III) H2O
X-ray Absorption
Energy (eV)
E
WT Fe(II) unligated
X-ray Absorption
Energy (eV)
F
WT Fe(II) CO
X-ray Absorption
Energy (eV)

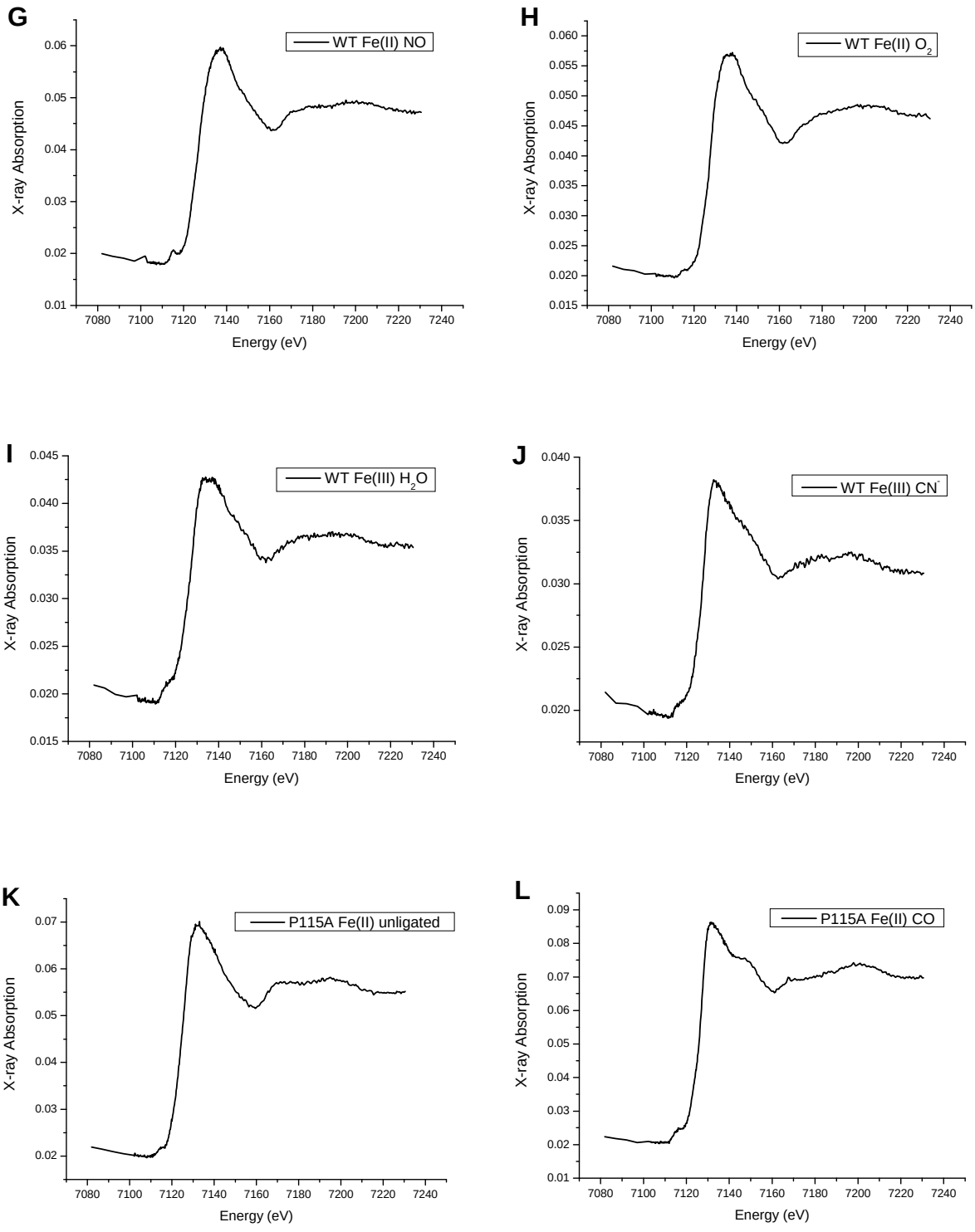
G
WT Fe(II) NO
X-ray Absorption
Energy (eV)
H
WT Fe(II) O2
X-ray Absorption
Energy (eV)
I
WT Fe(III) H2O
X-ray Absorption
Energy (eV)
J
WT Fe(III) CN-
X-ray Absorption
Energy (eV)
K
P115A Fe(II) unligated
X-ray Absorption
Energy (eV)
L
P115A Fe(II) CO
X-ray Absorption
Energy (eV)

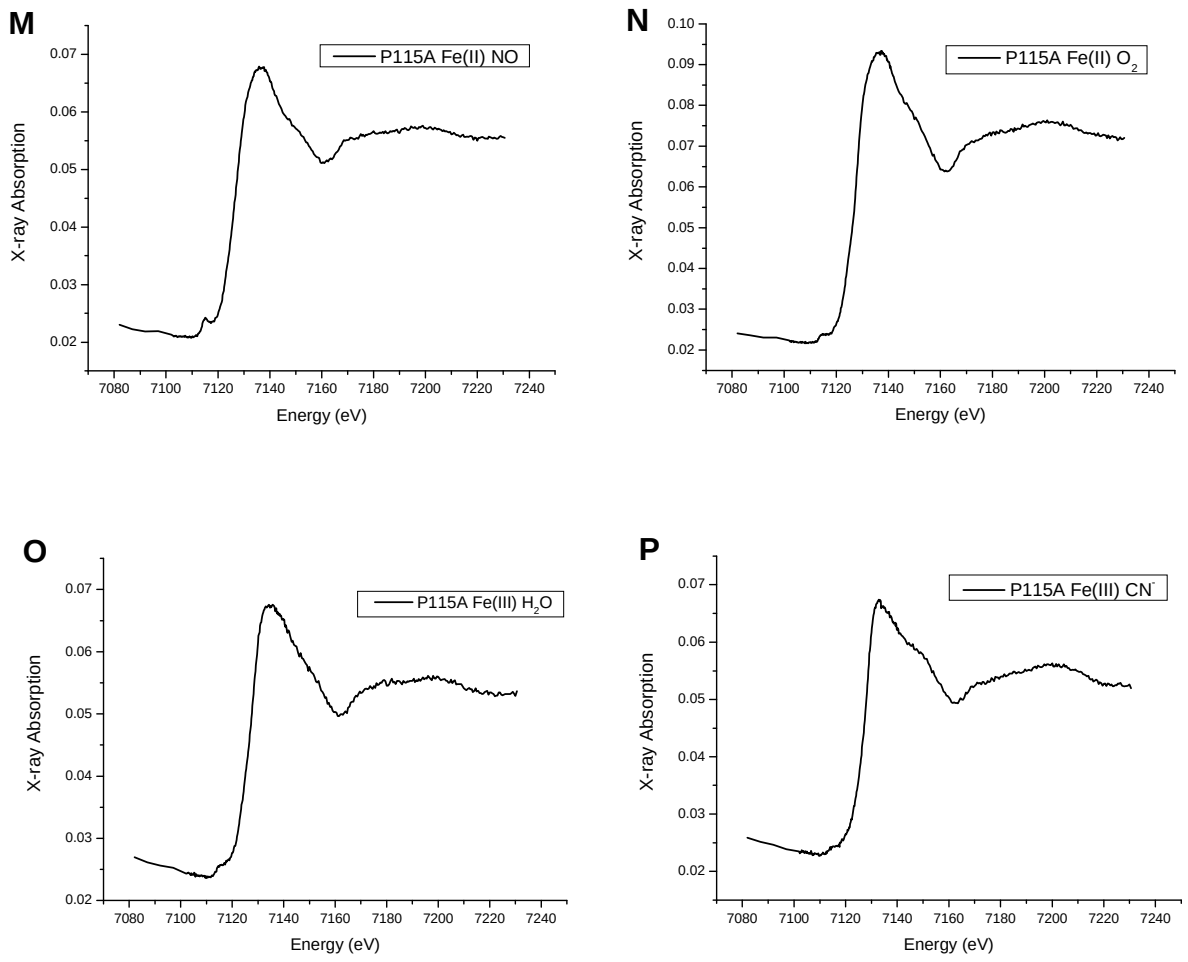

Figure 2-4. XANES spectra of all 16 hemoprotein complexes. Myoglobin samples: A. Mb Fe(II)-unligated; B. Mb Fe(II)-CO; C. Mb Fe(II)-O_2; and D. Mb Fe(III)-H_2O. *Tt* H-NOX samples: E. WT Fe(II) unligated; F. WT Fe(II)-CO; G. WT Fe(II)-NO; H. WT Fe(II)-O_2; I. WT Fe(III)-H_2O; J. WT Fe(III)-CN^-; K. P115A Fe(II) unligated; L. P115A Fe(II)-CO; M. P115A Fe(II)-NO; N. P115A Fe(II)-O_2; O. P115A Fe(III)-H_2O; and P. P115A Fe(III)-CN^-.

Table 2-2. X-ray absorption edge, LFIR value, and Fe-Ct displacement for Mb and *Tt* H-NOX complexes.

	Edge (eV)[a]	LFIR	Fe-Ct (Å)	
			From Crystallography	From LFIR
Mb Fe(II)-unligated	7123.1 (7123.0)[b]			
Mb Fe(II)-CO	7125.0 (7125.5)[b]			
Mb Fe(II)-O_2	7126.0 (7126.0)[b]			
Mb Fe(III)-H_2O	7125.9			
Tt WT Fe(II)-unligated	7124.1	0.98		-0.08
Tt WT Fe(II)-CO	7125.5	0.46		0.16
Tt WT Fe(II)-NO	7125.5	0.94		-0.06
Tt WT Fe(II)-O_2	7126.5	0.88	-0.03[c]	-0.03
Tt WT Fe(III)-H_2O	7126.5	0.94	-0.06[c]	-0.06
Tt WT Fe(III)-CN^-	7126.7	0.82		0.00
Tt P115A Fe(II)-unligated	7124.4	1.08		-0.12
Tt P115A Fe(II)-CO	7125.7	0.43		0.18
Tt P115A Fe(II)-NO	7125.9	0.90		-0.04
Tt P115A Fe(II)-O_2	7126.5	0.85	-0.02[c]	-0.02
Tt P115A Fe(III)-H_2O	7126.5	0.94		-0.06
Tt P115A Fe(III)-CN^-	7126.9	0.60		0.10

[a] X-ray absorption edges were determined assuming the edge for an iron foil is 7112.0eV; errors on edges are ±0.2eV. [b] Mb X-ray absorption edge values previously determined.[51] [c] Average Fe-Ct distances for all available crystal structures; negative values indicate the iron atom sits in the proximal heme pocket and positive values indicate the iron atom sits in the distal heme pocket.

Ligand field indicator ratio. Multiple backscattering of atoms neighboring the X-ray absorbing atom (here, Fe) dominates the XANES region of a XAS spectrum. The two peaks in the low energy region used to calculate LFIR (Figure 2-5A) are primarily due to partially resolved higher shell (second and third shells) ligating atoms.[47] Changes in the LFIR arise from

changes in the backscattering of these higher shell ligands. It has been established that LFIR can be used to probe the Fe motion in various heme-complexes and hemoproteins.[47,50,51]

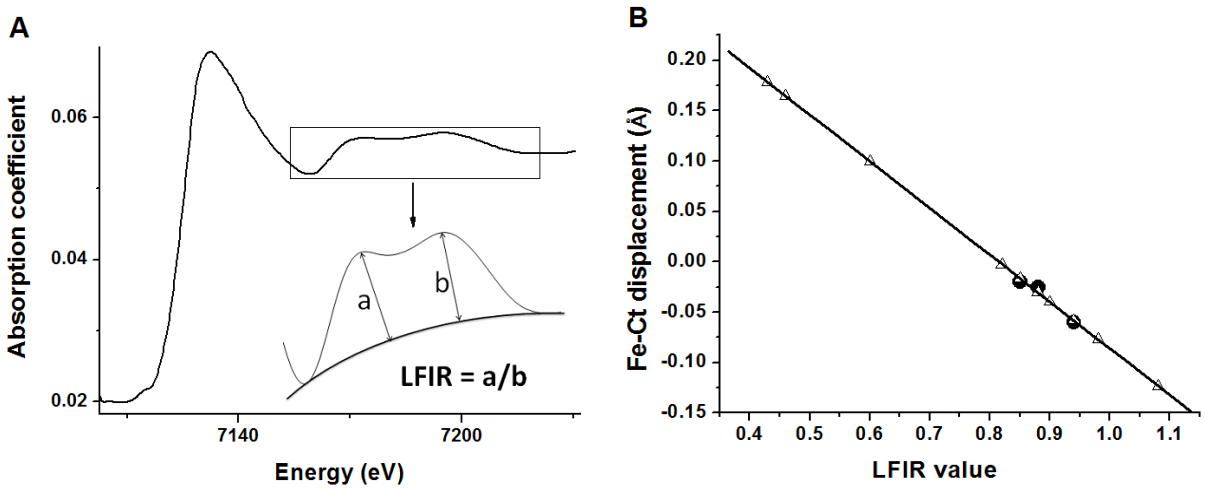

Figure 2-5. (A) Schematic illustration of the extraction of LFIR from a XANES spectrum. (B) Prediction of Fe-Ct displacements from LFIR values for various *Tt* H-NOX species. The data points in the black circles [WT Fe(II)-O_2, WT Fe(III)-H_2O and P115A Fe(II)-O_2] are based on known crystallographic displacements and were used to determine the correlation line for *Tt* H-NOX. The LFIR values obtained from XANES spectra are indicated in the white triangles. The estimated error in LFIR ratio values is ±0.05. The equation for the least squares line is: Fe-Ct displacement = -0.46 × LFIR + 0.38 (R^2 = 0.95).

To obtain the LFIR, a polynomial baseline is drawn starting from the minimum point preceding the first LFIR peak and ending at the tail of the second LFIR peak. Heights of the two LFIR peaks are measured to the baseline, and the LFIR ratio is the height of the first peak divided by the height of the second peak (Figure 2-5A). The ligand field indicator ratio yields a good empirical prediction of the spin state of the iron and the iron-heme displacement. For example, Chance, *et al.* has found that LFIR values linearly correlate to the movement of iron relative to the mean plane of the four porphyrin nitrogens (Fe-Ct displacement) for hemoproteins.[50,51]

We determined the LFIR and Fe-Ct displacement for each complex of WT and P115A *Tt* H-NOX. Crystal structures of three WT and P115A *Tt* H-NOX complexes have been solved [WT Fe(II)-O_2 (PDB 1U55 and 1U4H), WT Fe(III)-H_2O (PDB 1U56) and P115A Fe(II)-O_2 (PDB 3EEE)],[12,37] from which we extracted the crystallographically determined Fe-Ct distances in order to relate them to the measured LFIRs. Figure 2-5B illustrates the linear relationship between Fe-Ct displacement and LFIR for *Tt* H-NOX WT and P115A. Based on the least squares fit line determined by the three crystallographically characterized complexes, we predict the iron displacement from heme for all other ligand binding complexes, as shown in Table 2-2 and Figure 2-5B. The slope and intercept of the least squares fit line for *Tt* H-NOX is different than the slope reported for myoglobin, hemoglobin, and other model compounds.[50] The reasons for this are not clear, but apparently *Tt* H-NOX has different ligand field sensitivity to Fe-Ct displacement. Due to the limiting number of available WT and P115A *Tt* H-NOX crystal structures, the Fe-Ct displacements used for prediction do not cover the entire range of expected iron motion. However, because we focus on the relative magnitude of the Fe-Ct, and we are comparing various complexes of the same H-NOX domain, we can predict Fe-Ct displacements using measured LFIRs.

Most of the *Tt* H-NOX WT and P115A complexes have LFIR values between 0.85 and 1.08, which results in negative values for Fe-Ct displacement, indicating the iron is predicted to sit on the proximal side of the heme. The CO and CN^- complexes, however, have much smaller LFIRs (0.43-0.82) and display positive Fe-Ct displacement values [or no displacement for *Tt* WT Fe(III)-CN^-], indicating that the iron atom moves toward or into the distal heme pocket. The LFIR value and iron displacement towards proximal side for WT and P115A *Tt* H-NOX follow

the same trend: Fe(II)-CO < Fe(III)-CN^- < Fe(II)-O_2 < Fe(II)-NO ~ Fe(III)-H_2O < Fe(II)-unligated.

Cyanide binding kinetics. Fe-Ct displacement has been correlated with ligand binding affinity in hemoproteins.[50,57] Since Fe-Ct displacement is obtained from LFIR, ligand binding properties can therefore be predicted from LFIR data. Comparing the LFIR values of WT with P115A complexes (Table 2-2), we found that they are generally similar except for the Fe(III)-CN^- compounds (0.82 for WT versus 0.60 for P115A). Hence, we hypothesized that there would be large differences in CN^- binding properties to the ferric complexes of WT and P115A *Tt* H-NOX.

To test this prediction, we performed kinetic and equilibrium studies on Fe(III)-CN^- binding properties for both WT and P115A *Tt* H-NOX. The observed association rate constant (k_{obs}) values were obtained at various cyanide concentrations for both WT and P115A *Tt* H-NOX and were used to determine the association rate constant (k_{on}) (Figure 2-6). We found that cyanide binds to WT Fe(III) (k_{on} = 26.9 s^{-1} M^{-1}) almost 2000 times faster than to P115A Fe(III) (k_{on} = 0.0153 s^{-1} M^{-1}) (Table 2-3).

Table 2-3. Rate constants and equilibrium constants of cyanide binding to WT and P115A *Tt* H-NOX.

Species	k_{on} (s^{-1} M^{-1})	k_{off} (s^{-1})	K_d (μM)
Tt WT	26.9 ± 1.1	$2.19 \pm 0.02\times10^{-6}$	0.0813 ± 0.0203
Tt P115A	0.0153± 0.0011	$4.44 \pm 0.12\times10^{-9}$	0.290 ± 0.111

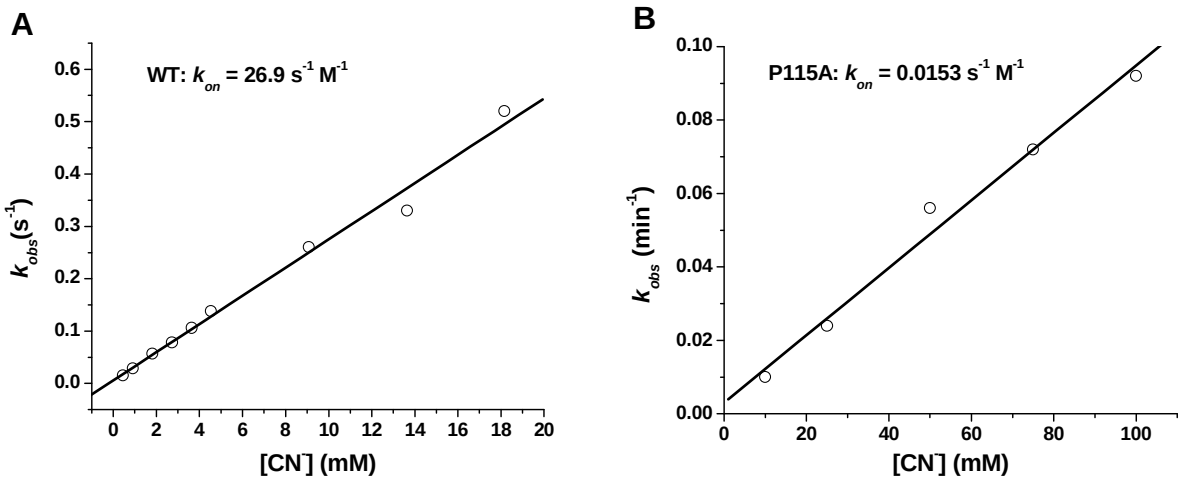

Figure 2-6. Determination of association rate constants for cyanide binding to ferric WT (A) and P115A (B) *Tt* H-NOX. We found that cyanide binds to ferric *Tt* H-NOX WT much faster than to P115A.

We have measured the equilibrium binding constant of CN^- for both ferric proteins; values of K_D for WT and P115A Fe(III)-CN^- were determined to be 81.3 nM and 290 nM, respectively.[35] Based on the measured K_D and k_{on} values, we calculated the dissociation rate constants k_{off} as 2.19×10^{-6} s^{-1} and 4.44×10^{-9} s^{-1} for WT and P115A *Tt* H-NOX, respectively. All the rate and equilibrium constants for cyanide binding to ferric *Tt* H-NOX are summarized in Table 2-3.

2.4. Discussion

The H-NOX family of proteins use a histidine-ligated protoporphyrin IX to bind low concentrations of NO and other diatomic gas molecules. Once the ligand is bound to H-NOX, signal transduction commences. In eukaryotes, this signal transduction results in activation of the

enzymatic domain of sGC,[1,41] while in prokaryotes, ligand binding is thought to regulate the activity of histidine kinases and di-guanylate cyclases.[18,23,58] In each case, however, the binding of a diatomic molecule to the heme center must be communicated to a different polypeptide domain for signal transduction to occur. The mechanism for this information transfer has not been determined. In this report, we have examined the local structural changes that take place at the heme iron during the first stages of signal transduction in order to shed light on the signaling mechanism of H-NOX proteins.

Insight into the H-NOX heme pocket and signaling properties based on K-edge absorption energies. Looking at the K-edge data broadly, we observe that the Fe(II) species generally have lower K-edge values than the Fe(III) species of *Tt* H-NOX. The only exception to this is the Fe(II)-O_2 complex, whose edge is about the same as the Fe(III)-H_2O complex. However, because of the strong electronegativity of oxygen, it is likely that the Fe(II)-O_2 complex has significant contribution from a Fe(III)-O_2^- resonance form. Therefore, the central iron in the *Tt* H-NOX oxy-complex may actually be electronically very similar with ferric complexes and thus this result is not unexpected. Furthermore, we found that the edge positions for WT and P115A complexes are generally similar, and that they follow the same trend. This confirms previous resonance Raman studies that indicate the P115A mutation results in a relatively minor perturbation to heme pocket, considering the dynamic nature of the heme structure in H-NOX.[38]

Looking at the data more closely, however, we can understand details of the electronic structure of H-NOX upon ligand binding. In hemoproteins, the iron edge position reports on the iron-ligand electron density distribution. As discussed, we found the 5-coordinate Fe(II)-unligated complexes have the lowest absorption edges of all the H-NOX complexes.

Qualitatively, upon binding of the sixth ligand in the distal pocket of *Tt* H-NOX, there is σ electron donation from the ligand to central iron that should act to reduce the effective charge of iron. However, as the sixth ligand pulls valence electrons away from the iron cation due to stronger electronegativity, the electrons around the central metal (in lower energy orbitals) are pulled closer to the nucleus to increase shielding of the existing nuclear charge, and hence increase the core shell electron excitation energy.[54] Apparently, the latter effect overwhelms the former as evidenced by the increasing K-edge values of CO-bound, NO-bound and especially the O_2-bound complexes. The K-edge value for the NO-bound complex is slightly larger than that for CO-complex, however it is not as much larger as would be expected based on the electronegativity difference between nitrogen and carbon. This is because of π-back bonding, in which iron donates its 3d electrons back to the π* anti-bonding orbitals of CO. Also as a result of the π-back bond donating electrons from iron to CN^- in the ferric states, the cyanide-bound complexes have slightly larger K-edges than water-bound complexes for both *Tt* H-NOX WT and P115A.

Because the edge position is a good indication of iron-ligand electron density distribution, it is related to electronic properties of the heme, such as iron reduction potential.[59-62] The heme iron in P115A has a lower reduction potential (-3.8 mV versus SHE) than that of WT *Tt* H-NOX (167.0 mV versus SHE).[37] Indeed, we see this difference reflected in the K-edges of the Fe(II)-unligated complexes of WT (7124.1 eV) and P115A (7124.4 eV). This difference (0.3 eV) is close to the limit of energy resolution in our data collection. However, we have repeated these scans several times with different samples and we always see a 0.3 eV difference, thus we believe this is reflective of a real difference in edge energy. The Fe(III)-H_2O K-edges are comparable, both at 7126.5 eV. Furthermore, iron porphyrins with more severe saddling are

known to have more positive reduction potentials, which serves to link heme conformation with redox properties.[63] Therefore we attribute the difference in ferrous K-edge energies to electronic structure changes that arise from a combination of changes in heme structure as well as overall changes in electrostatic interactions in the heme pocket, introduced upon mutation, that alter the dielectric constant and consequently lead to a different iron reduction potential.[64,65]

The significance of these results lies in the fact that we are able to address the re-distribution of electron density upon the binding of various ligands to H-NOX proteins, which is important in small molecule sensing processes. Our data predict that the heme structure and environment are more similar in the ferric state than the ferrous state. As only the ferrous oxidation state of H-NOX is expected to be physiologically relevant, this may indicate that heme structure is especially important for priming the H-NOX unligated protein for ligand (NO, CO or O_2) binding.

Insight into the H-NOX heme pocket based on ligand field indicator ratios. Crystallographically determined displacements of hemoglobin as well as many artificial porphyrin macrocycles, have established that the LFIR correlates with spin state and iron-heme displacement.[47] Miller *et al.* also found that there is a linear relationship between Fe-Ct displacement and LFIR in myoglobin;[51] a reduction in Fe-Ct displacement towards the distal side is always accompanied by an increase in LFIR. Here we have predicted the Fe-Ct for each complex of the *Tt* H-NOX domain using our LFIR data. Notably, the trend in Fe-Ct displacements implied by the LFIR data agrees with available crystallography data (Table 2-2 and Figure 2-5B).

As indicated before, we see a trend in the movement of iron towards the proximal pocket for both WT and P115A *Tt* H-NOX as a function of ligand binding: Fe(II)-CO < Fe(III)-CN^- <

Fe(II)-O_2 < Fe(II)-NO ~ Fe(III)-H_2O < Fe(II)-unligated. This trend is easily explained with the spectrochemical series and indicates ligand field strength. These data suggest that the strongest ligands studied here, CO and CN^-, which have significant π-back bonding interaction with the heme iron, "pull" the iron back to the distal side (where the sixth ligand locates), resulting in smaller iron movements to the proximal heme pocket in these complexes. For the same reason, in a strong ligand field, Fe uses 3d orbitals instead of 4d orbitals for hybridization, which also helps to reduce the Fe-ligand bond length and pull the iron away from the proximal side. Indeed, Fe-Ct displacements determined from recent crystal structures of *Ns* H-NOX support this interpretation. The *Ns* H-NOX Fe-Ct displacement changes from -0.31 Å (proximal side) for Fe(II)-unligated to +0.02 Å (distal side) for Fe(II)-CO complex,[22] indicating a substantial movement of iron towards the distal pocket after binding of a strong ligand. Conversely, since there is no or only a weak ligand for Fe(II)-unligated (5-coordinate) and Fe(III)-H_2O, these complexes of WT and P115A *Tt* H-NOX have the largest LFIR values and the largest displacement towards the proximal heme pocket (towards the proximal histidine ligand).

LFIR ratios also correlate with the magnetic moment of the heme. Chance *et al.* have obtained a good linear fit with a positive slope when plotting the LFIR values of various hemoproteins to their magnetic moments; lower LFIR values yield smaller magnetic moments.[47] The magnetic moments of *Tt* H-NOX complexes have not been independently measured. However, based on ligand strength and our LFIR values, we can predict their relative magnitude. For the high spin Fe(II)-unligated and Fe(III)-H_2O complexes, the 3d electrons are trying to occupy different d orbitals, since in this case the electron pairing energy is larger than the crystal field splitting energy, which results in more unpaired electrons and larger magnetic moments. However, the strong ligands CO and CN^- impose strong ligand fields to the central iron and lead

to low-spin iron with fewer unpaired electrons and a smaller magnetic moment. Therefore, we expect the magnetic moment for ferrous complexes in the *Tt* H-NOX system follow the trend: Fe(II)-CO < Fe(II)-O_2 < Fe(II)-NO < Fe(II)-unligated, and ferric states to follow this trend: Fe(III)-CN^- < Fe(III)-H_2O.

The spin state of iron is key to the local geometry of its complexes. Low spin iron porphyrin complexes tends to have less iron displacement towards the proximal histidine.[22,57,66] This is consistent with our observations that CO and CN^- complexes have the least iron displacement toward the proximal heme pocket. Therefore, the two seemingly separate parameters - the magnetic moment and Fe-Ct displacement - can both be predicted by our LFIR data and explained by the strength of the binding ligand.

Insight into H-NOX ligand binding properties based on ligand field indicator ratios. Fe-Ct displacement is also related to ligand binding affinity in hemoproteins.[50] We found large differences in the LFIR-predicted Fe-Ct values for the Fe(III)-CN^- complexes of WT and P115A H-NOX. Hence we predicted this was indicative of differences in the CN^- binding properties of the two proteins. Indeed, we observed large differences in CN^- binding properties of WT versus P115A *Tt* H-NOX. We found that cyanide binds to WT Fe(III) (k_{on} = 26.9 s^{-1} M^{-1}) almost 2000 times faster than to P115A Fe(III) (k_{on} = 0.0153 s^{-1} M^{-1}), and values of K_d for WT and P115A Fe(III)-CN^- are determined to be 81.3 nM and 290 nM,[35] respectively (Figure 2-6 and Table 2-3).

The rates of association and dissociation of CN^- in *Tt* H-NOX reflect the overall barrier of CN^- binding and leaving, respectively. The barriers mainly involve the diffusion of the ligand through the protein matrix and the interaction of the ligand with heme at the heme pocket. The ligand diffusion rates are expected to be similar for WT and P115A *Tt* H-NOX as they have the same protein fold. Thus, the differences in equilibrium and rate constants for CN^- binding to WT

and P115A ferric heme are attributed to the interaction of CN^- with the heme pocket and can be understood using the LFIR prediction of Fe-Ct displacement. As shown in Table 2-2, during the replacement of water during CN^- binding to the ferric heme, the central iron in P115A *Tt* H-NOX experiences a much larger shift (0.16 Å) than that for WT (0.06 Å), which may subsequently lead to a larger shift of proximal histidine as well as the whole protein conformation based on our discussion. All these movements contribute to a larger activation energy for the P115A mutant.

Steric hindrance also plays an important role in ligand binding. In this case, the iron in the WT *Tt* H-NOX Fe(III)-CN^- complex is located almost exactly at the center of the porphyrin nitrogens, while the iron in the P115A *Tt* H-NOX Fe(III)-CN^- complex moves dramatically into the distal pocket where cyanide locates; we suggest that this results in a more crowded distal heme pocket, and hence larger steric hindrance, consequently leading to a larger energy barrier for both CN^- association with and dissociation from P115A Fe(III). Thus k_{on} and k_{off} values for P115A are both much smaller than those measured for WT. Also due to the larger steric strain, the Fe(III)-CN^- complex for P115A is not as stable as that for WT *Tt* H-NOX, as indicated by the equilibrium dissociation constants.

Following this logic, we would also expect ferrous WT *Tt* H-NOX to have slightly greater affinity than its P115A analog for oxygen, due to its slightly smaller Fe-Ct displacement. However, it has been determined that the association and dissociation rate constants of O_2 binding to ferrous WT are 13.6 $s^{-1}\mu M^{-1}$ and 1.22 s^{-1} respectively, and to ferrous P115A are 10.4 $s^{-1}\mu M^{-1}$ and 0.22 s^{-1}, respectively.[37] These data indicate that oxygen binds to ferrous P115A more tightly than to ferrous WT *Tt* H-NOX. This disagreement is resolved upon consideration of the importance of H-bonds in stabilizing the H-NOX oxygen complex, however. It has been

demonstrated that a strong H-bond between tyrosine 140 and bound oxygen is essential for oxygen binding in the H-NOX family.[28] Inspection of the Fe(II)-O_2 crystal structures indicates that, in P115A the Tyr-OH is ~0.3 Å closer to the bound oxygen molecule than in WT, which is reflective of the change in Fe-Ct displacement. This suggests a stronger H-bond and thus a larger oxygen stabilization effect for the *Tt* H-NOX P115A oxy-complex. This stronger H-bond is supported by lengthening of the O-O bond in the oxygen molecule from 1.30 Å in the WT complex to 1.40 Å in the P115A complex, and the shortening of the Fe-O (O_2) bond from 1.80 Å in the WT complex to 1.74 Å in the P115A complex.[12,37]

Furthermore, in comparison to the Fe(II)-O_2 binding properties, the differences between WT and P115A Fe(III)-CN^- binding properties are much more extreme, reflecting the much larger differences observed in the LFIRs and Fe-Cts for this complex. As discussed, the predicted Fe-Ct values for ferrous oxy-complexes of WT and P115A are similar, while the difference between WT and P115A for the Fe(III)-CN^- complex is 0.10 Å. That the LFIR data do not pick up on the difference in affinity for O_2 is an indication of the sensitivity of this technique for predicting ligand binding affinity. This level of sensitivity is suggested in the Hb example discussed above; the iron atom and the heme are less coplanar by ~0.08 Å in the low affinity (T) form of hemoglobin than the high affinity (R) form. Therefore, a more dramatic difference between WT and P115A for Fe(III)-CN^- binding is predicted from XAS measurements, as we have observed.

Based on this argument, we expect differences in the CO and NO affinities to be similar in scale to the differences observed in the O_2 affinities, as the differences in Fe-Ct displacements for these ligands are small. Indeed, we find that the NO dissociation rate constants for *Tt* H-NOX WT and P115A are more similar, 0.042 min^{-1} and 0.026 min^{-1}, respectively (Chapter 6, Table 6-

1). Therefore, in addition to the crystallographically measured displacements discussed above, the correlation we observe between ligand binding affinity and LFIR-predicted Fe-Cts supports our assignment of Fe-Cts in this system.

Insight into the H-NOX involved signaling pathway based on LFIR predicted iron-heme displacement. The current view on signal transduction in H-NOX proteins is that upon ligand binding, the proximal histidine protein residue dissociates, leading to protein conformational changes.[41,67,68] New data has also suggested a role for heme distortion in triggering protein conformational changes.[22,30] Structural data indicate that upon ligation, the heme flattens and the αF and N-terminal αA-αC helices shift.[22]

The data presented here provide a description of the changes in the electronic structure and position of the heme iron that occur upon ligand binding. We suggest movement of the heme iron is the initial step in signaling that gives rise to subsequent conformational changes in the histidine ligand, heme conformation, and protein conformation. Our XAS data indicate that diatomic gas binding to the H-NOX heme alters the position of the central iron, moving it towards or into the distal heme pocket. Because the heme is in contact with a large number of atoms in the protein matrix of H-NOX, porphyrin iron displacement alone could trigger changes in the tertiary structure needed for signal transduction. Iron movement into the H-NOX distal pocket can cause protein tertiary structural changes by one or both of two mechanisms: through lengthening or breaking the Fe-histidine (proximal) bond and/or through distal pocket rearrangements brought about by changes in heme structure. Iron moving toward the distal side of the heme pocket would lengthen and/or break the bond with the proximal histidine ligand. This would then lead to a shift in the position of histidine residue and relax the αF helix where the histidine resides, causing the αF helix to move further from the heme pocket (Figure 2-1). In

addition, ligand binding in the distal pocket, accompanied by iron movement into the distal pocket, would result in a crowded distal pocket with substantial steric strain, as evidenced by our cyanide binding data. Hence, a rearrangement of this pocket, involving the N-terminal αA-αC helices, would be required to release the strain.

These alterations in tertiary structure would provide for direct communication between ligand binding and downstream signaling events (Figure 2-7). Our hypothesis is supported by recent subpicosecond time-resolved resonance Raman and femtosecond transient absorption spectroscopy results which emphasize the importance of heme iron motion for heme and protein conformational changes in hemoproteins.[69]

Our data indicate that CO binding, as well as NO binding, causes the iron to move substantially into the distal pocket, thus this mechanism does not discriminate against CO as an activating molecule for H-NOX proteins. Indeed, in combination with an allosteric activator such as YC-1, CO fully activates sGC.[70] Recent resonance Raman experiments have shown that during activation of CO-bound sGC by YC-1, the iron moves so far into the distal pocket that there is evidence that the Fe-His bond breaks, creating a population of 5-coordinated sGC-CO complex.[40] It is proposed that this population of 5-coordinate sGC, in which Fe has substantially moved towards the distal pocket, is the active state in both NO and CO/YC-1 bound sGC. These data further emphasize the importance of iron-heme displacement in the H-NOX signaling cascade.

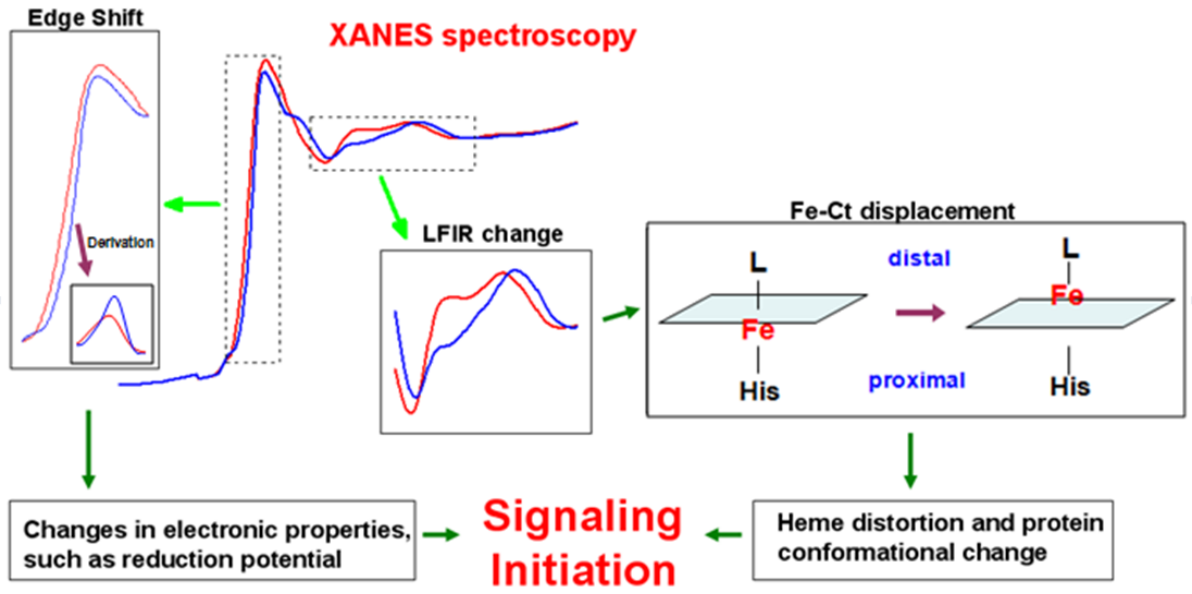

Figure 2-7. Insight into the molecular basis of signal initiation of H-NOX domains based on XANES spectroscopy. The synergism between local structural rearrangement and electronic environment change leads to the signaling initiation step of the NO/sGC signaling pathway.

Our K-edge and LFIR data indicate that the greatest differences in the electronic and geometric properties of the heme pocket between WT and P115A occur in the Fe(II)-unligated and Fe(III)-CN^- complexes. As H-NOX is expected to remain in the ferrous oxidation states throughout its physiological function, this may indicate that H-NOX heme structure has been optimized to produce the largest changes in the H-NOX heme environment upon ligation by O_2, CO, or NO, the likely functional ligands in this family.

2.5. Conclusion

Understanding the molecular details of how sGC and other H-NOX proteins sense small signaling molecules is still under investigation. We employed X-ray absorption spectroscopy to

study the local electronic and geometric properties of the iron center in the heme pocket of WT and P115A *Tt* H-NOX, a prokaryotic analog of sGC. Our results shed light on electronic and conformational changes that occur in the heme pocket of H-NOX proteins after ligation and during initiation of signaling, which confirms that XAS is a promising approach in studying the NO/sGC signaling pathway.

The K-edge absorption energies measured here yield the effective charges on the iron center as well as the distribution of electron density for various complexes. Based on our XAS data, we evaluated the spin states of iron and predicted the Fe-Ct displacement for *Tt* H-NOX WT and P115A mutant complexes. Our XANES predictions of Fe-Ct were confirmed by known crystallographic data and ligand binding properties. We propose that this iron displacement upon ligand binding is the driving force leading to protein conformation changes in the αF helix and the N-terminal αA-αC helices, which subsequently contribute to signal initiation in the H-NOX family.

Chapter 3. EXAFS Analysis Reveals Structural Insights into the Molecular Basis of NO/H-NOX Signaling Mechanism

Abstract: Heme-Nitric oxide and/or OXygen binding (H-NOX) proteins are a family of recently identified diatomic gas (NO, O_2) sensing hemoproteins that have attracted great interest. Soluble guanylate cyclase (sGC), the best studied H-NOX family member, binds NO as a 5-coordinate (5c) complex, leading to the full activation of this enzyme. Some other H-NOXs bind NO in a 6-coordinate manner, or as a 5c/6c mixture. To examine the molecular details of the NO/H-NOX binding and signaling, here we investigated the Fe(II)-unligated and Fe(II)-NO complexes of H-NOX proteins from *Thermoanaerobacter tengcongensis* (*Tt* H-NOX), *Shewanella woodyi* (*Sw* H-NOX), and *Pseudoalteromonas atlantica* (*Pa* H-NOX). We focused on using the Extended X-ray Absorption Fine Structure (EXAFS) analysis to obtain structural details of the heme pocket for these H-NOX complexes. Our results suggest that NO binds to *Tt* H-NOX in a 6-coordinate manner, while to *Sw* H-NOX and *Pa* H-NOX in a 5-coordinate manner with proximal histidine dissociating away, which is exactly the same as sGC. In the *Tt* H-NOX Fe(II)-NO compound, the Fe-histidine bond is substantially lengthened although it is not broken. This coordination chemistry has also been confirmed by their UV/visible spectra and iron K-edge values. On the basis of EXAFS fitting for all three H-NOX Fe(II)-unligated complexes, we noticed a ~0.07 Å shortening in the Fe-N_p bond lengths upon NO binding; such a contraction in Fe–N_p bond lengths could be important for the signal initiation step of NO sensing.

3.1. Introduction

The ability of an organism to respond to internal and external signals is critical for its survival. Diatomic gas molecules like nitric oxide (NO) have been increasingly recognized as important signaling molecules that induce signal transduction through selective binding with cognate sensor proteins.[1,14,24,26,58] A family of heme-based sensor proteins, named Heme-Nitric oxide and/or OXygen binding (H-NOX) proteins, has been found to play essential roles in gas molecule sensing in a variety of biological systems.[17,24-27] The best studied H-NOX family member is soluble guanylate cyclase (sGC), the only confirmed NO sensor in mammals. Upon binding of NO to the H-NOX domain of sGC, the enzymatic activity of sGC is enhanced by over 200-fold, leading to a significant increase in the production cyclic guanosine monophosphate (cGMP) (Figure 1-1). Through its interactions with downstream signaling systems, cGMP regulates important biological processes including neurotransmission, smooth muscle relaxation, and inhibition of platelet aggregation. [1,8,14,33]

In addition, H-NOX proteins also widely exist in prokaryotes and are involved in important signaling pathways that regulate the behavior of these organisms.[24-26] For example, in *Shewanella woodyi*, an H-NOX gene is located upstream of a gene encoding a di-guanylate cyclase (DGC) within the same putative operon (Figure 1-2). Recent biochemical and genomic studies in our group have shown that NO modulates a protein-protein interaction of H-NOX with the DGC, which subsequently affects *S. woodyi* biofilm formation. Moreover, NO-bound H-NOX proteins have been implicated in signaling pathways in many other bacteria like *Legionella pneumophila*,[25] *Shewanella oneidensis*,[26] and *Vibrio* species[24] (Figure 1-2). Therefore, understanding the detailed molecular mechanism of how NO is sensed by H-NOX protein is of crucial importance.

In 2004, crystal structure of the predicted O_2-sensing H-NOX domain from *Thermoanaerobacter tengcongensis* (*Tt* H-NOX) was solved to a resolution of 1.77 Å (Figure 1-3),[12] which has greatly helped to understand the structure-function correlation of the H-NOX family. Although this *Tt* H-NOX is predicted to be an O_2 sensor, its structure has been widely used to model the sGC heme domain and other H-NOX proteins due to the high homology in their protein sequences. And a great amount of valuable insights into the H-NOX signaling mechanism have been obtained.[18,28-31,36-38,44] Currently the prevalent hypothesis for NO/H-NOX signaling is that NO binding to H-NOX generates conformational changes to the heme group and the H-NOX domain; such changes induce downstream signaling cascade through either domain-domain interactions in large enzyme complexes (like sGC) or protein-protein interactions of H-NOX with effector enzymes (like DGC and histidine kinase). However, the molecular details of these heme and H-NOX conformational changes induced by NO ligation remain to be fully elucidated.

One critical problem that severely impedes the study on H-NOX signaling is the lack of structural information at the heme pocket for the Fe(II)-unligated and Fe(II)-NO complexes, which respectively represent the physiological rest state and active state of these NO sensors. There has been no success in crystallizing Fe(II)-unligated H-NOX and only one crystal structure of Fe(II)-NO complex, the NO-bound *Nostoc sp* H-NOX (*Ns* H-NOX), has been reported.[22] But it turns out that this NO-bound *Ns* H-NOX complex is a mixture of 6-coordinate (6c) and 5c-NO heme with 6c-NO as the predominant species. This largely limits the amount and accuracy of the structural information that can be extracted. Therefore, a thorough structural characterization of the heme pocket for the H-NOX Fe(II)-unligated and Fe(II)-NO complexes are highly desirable.

In this work, we concentrate on using iron K-edge X-ray absorption spectroscopy (XAS) to characterize the H-NOX Fe(II)-unligated and Fe(II)-NO states. XAS is a powerful technique for examining Fe-heme local structure and electrostatics in hemoproteins, providing information on Fe oxidation state, spin state, the number and type of ligands bound to Fe, and Fe-ligand bond lengths. In previous work, we have used iron K-edge to examine the flow of electron density between the iron center and surrounding ligands, and the X-ray Absorption Near-Edge Structure (XANES) to predict the iron-heme displacement upon ligand binding to *Tt* H-NOX.[36] Here we present our work of using the Extended X-ray Absorption Fine Structure (EXAFS) analysis to obtain structural details of the heme pocket for several different H-NOXs.

Specifically, we investigated the Fe(II)-unligated and Fe(II)-NO complexes for three different H-NOX proteins, H-NOX from *Thermoanaerobacter tengcongensis* (*Tt* H-NOX), H-NOX from *Shewanella woodyi* (*Sw* H-NOX), and H-NOX from *Pseudoalteromonas atlantica* (*Pa* H-NOX). The results for NO complexes indicate that NO binds to *Tt* H-NOX in a 6-coordinate manner, and to *Sw* H-NOX and *Pa* H-NOX in a 5-coordinate manner. Based on the EXAFS fits of *Tt* H-NOX data, we found that even though the Fe-histidine bond is not broken in NO-bound *Tt* H-NOX, it is substantially weakened likely due to the strong trans effect of NO. On the basis of EXAFS fits for the Fe(II)-unligated complexes, we noticed a ~0.07 Å shortening in the Fe-N_p bond lengths upon NO binding for all three H-NOXs; such a contraction in Fe–N_p bond lengths could be important for the signal initiation step of NO sensing.

3.2. Materials and Methods

Plasmid preparation and protein expression. Cloning of the *Tt* H-NOX domain into a pET-20b (Novagen) vector has been described previously.[21] For ease of purification, a C-terminal 6×His tag was incorporated to the plasmid ahead of the stop codon. Plasmids for *Sw* H-NOX and *Pa* H-NOX were cloned into pET-23b and pET-20b, respectively. Cell culture preparation and expression procedures of H-NOX proteins were carried out as previously described.[36]

Protein purification. To purify *Tt* H-NOX, cell lysis and thermal denaturation treatments were carried out as described.[21] The supernatant after thermal denaturation was filtered through a 0.45 µm membrane and the filtrate was applied to a 1 mL HisTrap HP column (GE Life Sciences) pre-equilibrated with buffer A [50 mM sodium phosphate, 300 mM NaCl, pH 7.5]. The column loaded with *Tt* H-NOX was washed using 30 mL buffer A and then three more washes were performed using 20 mL buffer A with 10 mM imidazole, 20 mL buffer A with 20 mM imidazole, and 10 mL buffer A with 50 mM imidazole. The protein was ultimately eluted using buffer A with 250 mM imidazole. The flow rate was controlled at 1 mL/min. The protein was then exchanged into buffer B [50 mM HEPES, 50 mM NaCl, 5% glycerol and 5 mM DTT, pH 7.5] using a PD-10 column (GE Healthcare), aliquoted, and stored at -80 °C. To purify *Sw* H-NOX and *Pa* H-NOX, the procedures are the same as that for *Tt* H-NOX except that thermal denaturation was not performed, because these two H-NOX proteins are not as thermal stable. The procedure resulted in protein that was >95% pure as estimated by SDS-PAGE.

Electronic spectroscopy. All UV/visible spectra were recorded on a Cary 100 Bio spectrophotometer equipped with a constant temperature bath set to 20 °C. Preparation of ferrous complexes was carried out as previously published.[21]

XAS sample preparation. Ferrous (-unligated and -NO) complexes of H-NOXs were prepared in the glove bag as previously described.[21] H-NOX protein samples were exchanged into XAS sample buffer [50 mM HEPES, 50 mM NaCl, 20% glycerol, pH 7.5] and concentrated to 1-2 mM using spin columns from Millipore [Microcon Ultracel YM-3, 3000 molecular weight cut off (MWCO) and 0.5 mL maximum volume]. The concentrated protein samples were transferred to copper sample holders with Mylar windows (10 mm wide × 5 mm high × 0.5 mm thick), frozen in liquid nitrogen and stored at -80 °C before XAS experiments.

X-ray absorption spectroscopy. XAS data collection was carried out at the National Synchrotron Light Source (NSLS) at Brookhaven National Laboratory (BNL), on beamline X3B with a sagittally focused Si (111) crystal monochromator. Samples were cooled to at least 40 K before scanning in a closed-cycle liquid helium diplex and kept frozen during data collection. K_α fluorescence was detected with a Canberra 13-element germanium detector. An iron foil was used as a reference to determine the X-ray absorption edge for each spectrum and to account for any shifts in the monochromator. The step size at the edge region was set to 0.2 eV. 6-9 scans for each complex were taken and averaged for data analysis. In order to minimize radiation damage to the samples, we made multiple samples for the same complex and collected at most 2 scans per X-ray exposed spot. XAS data were aligned, background-removed, normalized and merged using Athena. The K-edge positions were determined from the first derivative of the average XAS spectra after smoothing. The derivative spectra were smoothed using Origin 7.0. EXAFS fitting of all data were carried out using EXAFSPAK.

3.3. Results and Discussion

UV/visible spectroscopy. UV/visible spectra of hemoproteins are indicative of the Fe oxidation state as well as the bound ligand. As shown in Figure 3-1 and Table 3-1, Fe(II)-unligated state for all three H-NOX proteins shows a Soret band maximum at ~430 nm with a merged α/β band at ~560 nm, demonstrating a 5-coordinate, high-spin complex. Addition of NO to the *Tt* H-NOX Fe(II)-unligated solution generates a 6-coordinate Fe(II)-NO compound, showing a Soret band at 419 nm. However, the Fe(II)-NO complexes for *Sw* H-NOX and *Pa* H-NOX have Soret bands at ~399 nm and split α/β bands at ~570 nm and 543 nm respectively, which are the same as that for sGC. On the basis of these results, we predict that both *Sw* H-NOX and *Pa* H-NOX form 5-coordinate Fe(II)-NO complexes with the Fe-His bond broken. Thus, characterization of these two H-NOX proteins can not only identify the molecular factors involved in their own signaling systems, but also provide helpful insights for the NO-sGC activation mechanism.

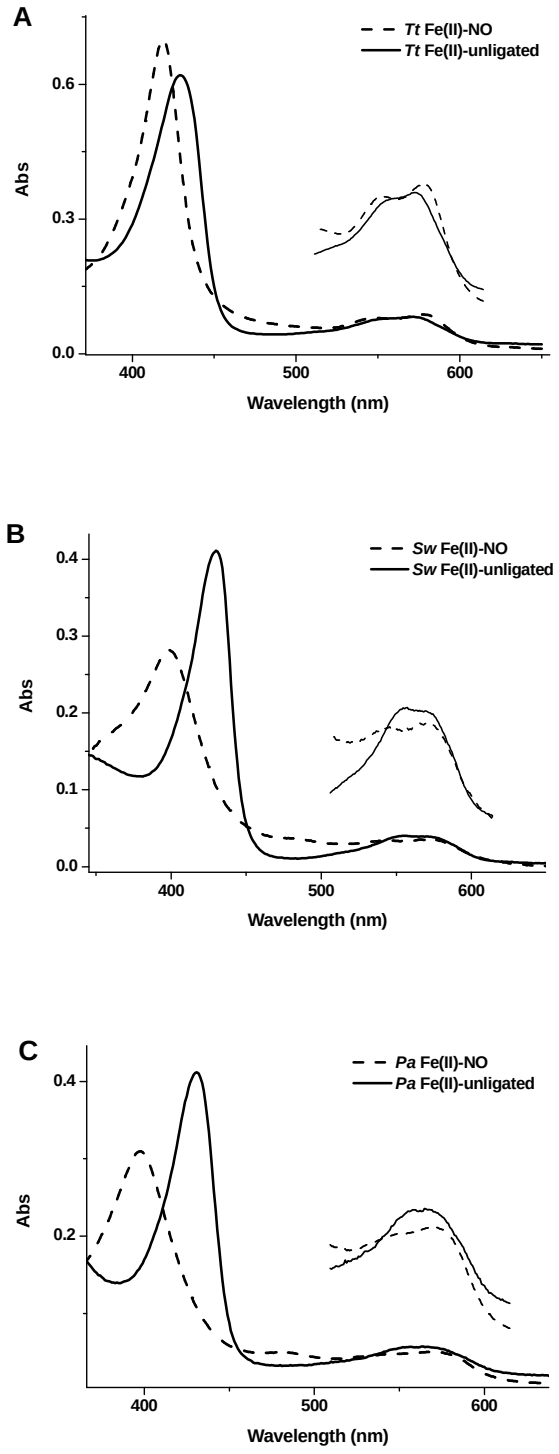

Figure 3-1. UV/visible spectra of *Tt*, *Sw* and *Pa* H-NOX in Fe(II)-unligated (solid) and Fe(II)-NO (dash) states.

Table 3-1. UV/visible spectra peak positions and iron K-edges for *Tt*, *Sw* and *Pa* H-NOX in Fe(II)-unligated and Fe(II)-NO states. (unit: nm for UV/visible spectra peaks and eV for edge)

	Soret	β	α	edge
Fe(II)-unligated				
T. tengcongensis	429	560		7124.1
S. woodyi	430	564		7123.4
P. atlantica	431	561		7123.2
sGC	431	555		-
Fe(II)-NO				
T. tengcongensis	419	547	577	7125.5
S. woodyi	399	543	572	7123.7
P. atlantica	398	543	569	7123.0
sGC	398	537	572	-

Iron K-edge of H-NOX complexes. Iron K-edge indicates the energy required to excite the core shell (1s) electron of the Fe atom. Higher edge position corresponds to larger energy requirement for electron excitation and more positive effective charge on the iron. Thus, analysis of the Fe edge positions for H-NOX protein complexes implies the electron density on the heme iron and show how the electron density flows upon ligand binding. We have determined the Fe K-edge positions for *Tt* H-NOX before, and the values for Fe(II)-unligated and Fe(II)-NO complexes are 7124.1 eV and 7125.5 eV, respectively (listed in Table 3-1).[36] The 1.4 eV increase in edge energy upon NO binding suggest an extensive electron flow from Fe to its surrounding ligands (including NO), generating a more positive heme iron center.

However, results here show that for *Sw* and *Pa* H-NOX, the edge values for their Fe(II)-NO complexes are similar with the ones for their Fe(II)-unligated complexes (Table 3-1). This can be attributed to the 5-coordinate environment of these two NO complexes. We have shown that addition of a bound ligand causes an increase in the H-NOX Fe K-edge due to the strong electronegativity of ligation atoms. In the case of *Tt* H-NOX, NO binding leads to an increase in

the coordination number from 5 to 6; the exogenous NO ligand pulls the valence electrons away from the Fe nucleus, resulting in a larger K-edge value. While for *Sw* and *Pa* H-NOX, at the same time that NO binds to the heme iron, the proximal histidine ligand dissociates, keeping a 5-coordinate environment. Therefore, the effect of NO association on iron electron density is roughly cancelled out by histidine dissociation, resulting in similar K-edge values. These data agree with our UV/visible results that both *Sw* H-NOX and *Pa* H-NOX form 5-coordinate Fe(II)-NO complexes.

The insignificant difference in iron K-edge caused by NO association does not exclude the importance of Fe electronic environment in a NO signaling event. The edge energy has implication on the net electron density on heme iron; however, it does not reveal the detailed iron electric field. Upon the binding of NO to the distal pocket, there will be a correlated electron density change to the distal side of heme plane, and an opposite electron density shift on the proximal side accompanying the dissociation of proximal histidine. Therefore, the seemingly identical edge values for Fe(II)-unligated and Fe(II)-NO complex may actually represent two distinct electronic environment at the heme pocket. Such changes should contribute to the NO-induced H-NOX signaling. Only considering the electronic implication from edge values together with the coordination structure of heme iron can we reach an accurate understanding of the heme pocket electrostatics.

Furthermore, we find that the K-edge value for *Tt* H-NOX Fe(II)-unligated state is ~1.0 eV greater than those for *Sw* and *Pa* H-NOX (Table 3-1). Such a dramatic shift in edge energy suggests a large electrostatic difference at the heme pocket, indicating a more positive heme iron in *Tt* H-NOX. We reason that this large difference is correlated with their distinct functions; *Tt* H-NOX is predicted to be an O_2 sensor while *Sw* and *Pa* H-NOX are expected to be NO sensors.

In addition, as it has been suggested that the severe heme distortion in wildtype *Tt* H-NOX creates a low electron density at heme iron,[39] larger edge value should correlate with larger heme distortion. Therefore, on the basis of their K-edges, we predict that *Sw* and *Pa* H-NOX have a flatter heme plane than *Tt* H-NOX, which may also be an indication of their functionality difference.

EXAFS analysis of H-NOXs. EXAFS is a powerful technique that has been extensively used to examine the coordination chemistry of metal centers in metalloproteins, including heme-based sensor proteins. Here we use it to identify the exact molecular details of heme conformational changes induced by NO binding to the three different H-NOXs.

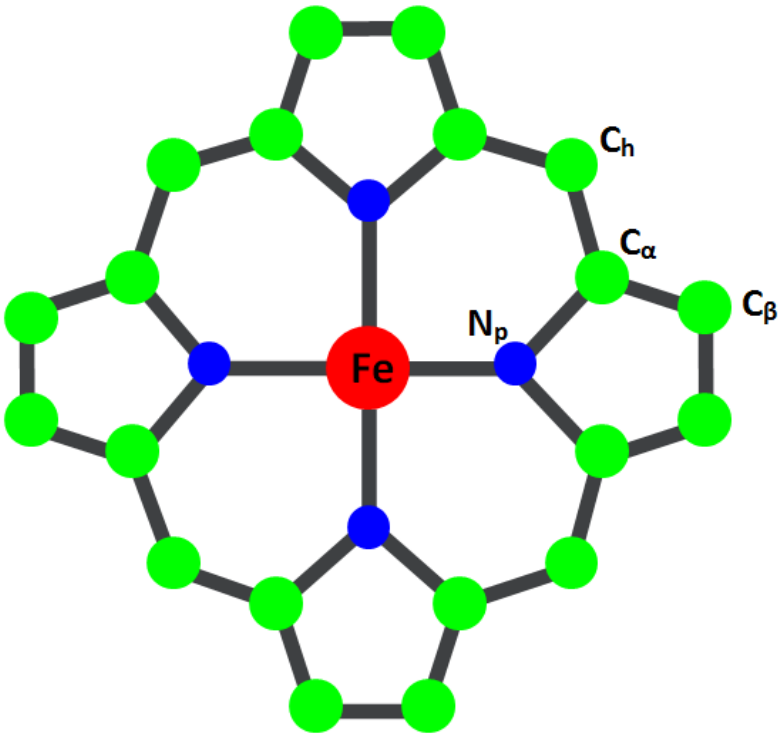

Figure 3-2. Sketch of the heme macrocycle. Fe, N and C are colored in red, blue and green, respectively. N_p, Cα, Cβ, and C_h atoms are labeled.

A detailed EXAFS analysis was carried out for the Fe(II)-NO complex of *Tt* H-NOX, and is summarized in Tables 3-2. A large portion of the EXAFS of NO-ligated *Tt* H-NOX can be simulated with a set of 4 Fe–N_p scatterers at 1.99 Å associated with the equatorial N donors of the heme, along with a set of single and multiple scattering paths associated with the Cα, Cβ, and C_h atoms assignable to the pyrrole moieties of the heme (Figure 3-2 and Table 3-2, fit 1). Addition of a single Fe–N/O scatterer at 1.75 Å attributed to bound NO results in a significant improvement in fit quality (Table 3-2, fit 2). We note that the Debye-Waller factor (σ^2) for this shell is comparably large, which may reflect either sub-stoichiometric binding of NO or more than one NO binding mode. It was not possible to identify unique multiple-scattering paths involving the Fe–NO unit that would enable determination of the Fe–NO bond angle. Additional attempts were made to fit the inner shell to a six-coordinate Fe(II) site by inclusion of an axially bound Fe–N_{His} bond. A fit with a single shell of 5 (Fe–N_p + N_{His}) shells (Table 3-2, fit 3) resulted in a significant decrease in fit quality and a much larger σ^2 value for the principal Fe–N shell, suggesting that the Fe–N_{His} bond, if present, has a bond length very different from those of the equatorial heme nitrogens. Indeed, a weak and disordered Fe–N_{His} bond of 2.32 Å can be resolved (Table 3-2, fit 4), providing a modest improvement in fit quality, as can be seen in Figure 3-3. This long Fe–N_{His} bond length is consistent with the notion of a six-coordinate ferrous NO complex in WT *Tt* H-NOX, in which the Fe-N_{His} binding is severely weakened by the NO trans effect.

Table 3-2. Selected EXAFS fits to *Tt* H-NOX Fe(II)-NO data.[a]

***Tt* H-NOX Fe(II)-NO complex**

fit 1			**fit 2**			**fit 3**			**fit 4**		
shell	r (Å)	σ^2	shell	r (Å)	σ^2	shell	r (Å)	σ^2	shell	r (Å)	σ^2
			1 Fe-NO	1.75	5.1	1 Fe-NO	1.73	3.0	1 Fe-NO	1.74	5.4
4 Fe-N_p	1.99	3.9	4 Fe-N_p	1.97	3.3	4 Fe-N_p + 1 Fe-N_{His}	1.97	5.1	4 Fe-N_p	1.97	3.4
									1 Fe-N_{His}	2.32	6.5
8 Fe--Cα	3.01	3.3	8 Fe--Cα	2.99	3.6	8 Fe--Cα	2.99	3.6	8 Fe--Cα	2.99	3.5
16 Fe--Cα/N_p	3.18	6.8	16 Fe--Cα/N_p	3.16	7.2	16 Fe--Cα/N_p	3.16	7.2	16 Fe--Cα/N_p	3.16	7.1
Fe--C_h	3.10	37.5	Fe--C_h	3.34	4.9	Fe--C_h	3.34	4.9	Fe--C_h	3.35	4.5
Fe--Cβ	4.36	6.3	Fe--Cβ	4.31	5.5	Fe--Cβ	4.31	5.4	Fe--Cβ	4.31	5.5
Fe--Cβ/N_p	4.39	12.6	Fe--Cβ/N_p	4.34	11.0	Fe--Cβ/N_p	4.33	10.8	Fe--Cβ/N_p	4.33	11.0
F		0.369	F		0.286	F		0.315	F		0.270
ΔE_0		8.40	ΔE_0		3.76	ΔE_0		3.43	ΔE_0		3.48

[a] *r* is in units of Å; σ^2 is in units of 10^{-3} Å^2. All fits are to unfiltered data. F represents a goodness-of-fit parameter. Fourier transform range k = 2.0 – 13.85 Å^{-1} (resolution = 0.134 Å). Values of r for the Fe--Cα single scattering and Fe--Cα/N_p multiple scattering paths were constrained to a constant difference from one another, while σ^2 for the multiple scattering path was constrained to be twice that of the single scattering path. A similar constraint was placed on the Cβ and Cβ/N_p combination.

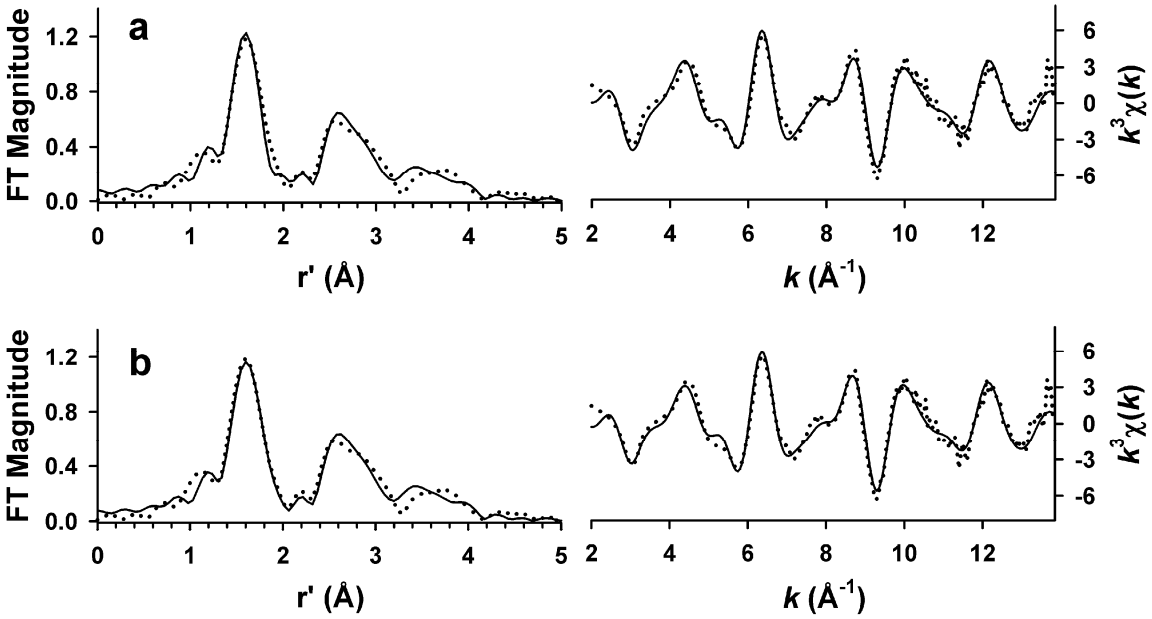

Figure 3-3. Representative best fits to the Fourier transforms of the Fe K-edge EXAFS data ($k^3\chi(k)$, left) and unfiltered EXAFS spectra ($k^3\chi(k)$, right) for WT *Tt* H-NOX Fe(II)-NO complex. Experimental data is shown with dotted lines (•••), fits are shown with solid lines. Fourier transformation range: k = 2 – 13.85 Å^{-1}. Fit parameters correspond to (a) fit 2 and (b) fit 4 in Table 3-2.

Similar EXAFS analyses were obtained for the NO-complexes of *Sw* and *Pa* H-NOX (Table 3-3). EXAFS data for both species was adequately simulated by a short Fe–N scatterer from bound NO and a set of single and multiple scattering pathways associated with the heme macrocycle. Although we expected a five-coordinate site to provide the best fit, it was possible to include a long Fe–N scatterer at *ca.* 2.3 – 2.35 Å and slightly improve fit quality over the five-coordinate fits. However, we note that for both *Sw* and *Pa* H-NOX (Table 3-3, fits 6 and 8), the σ^2 values for this Fe-N_{His} shell were larger than that obtained for *Tt* H-NOX. We can therefore conclude from this analysis that, even if the axial His in NO-ligated *Sw* and *Pa* H-NOX is bound to heme Fe, the binding is weaker than that in *Tt* H-NOX. In a combined view of UV/visible spectra, Fe K-edge results and the EXAFS fitting, we conclude that the Fe-His bond is actually

Table 3-3. Selected EXAFS fits to *Sw* and *Pa* H-NOX Fe(II)-NO data.[a]

***Sw* H-NOX Fe(II)-NO**						***Pa* H-NOX Fe(II)-NO**					
fit 5			**fit 6**			**fit 7**			**fit 8**		
shell	r (Å)	σ^2	shell	r (Å)	σ^2	shell	r (Å)	σ^2	shell	r (Å)	σ^2
1 Fe-NO	1.75	1.8	1 Fe-NO	1.75	2.1	1 Fe-NO	1.72	5.3	1 Fe-NO	1.72	5.4
4 Fe-N_p	1.99	2.0	4 Fe-N_p	1.99	2.1	4 Fe-N_p	1.98	4.0	4 Fe-N_p	1.98	4.0
			1 Fe-N_{His}	2.32	8.4				1 Fe-N_{His}	2.35	10.5
8 Fe--Cα	3.02	3.0	8 Fe--Cα	3.02	3.0	8 Fe--Cα	3.03	2.8	8 Fe--Cα	3.03	2.7
16 Fe--Cα/N_p	3.19	6.1	16 Fe--Cα/N_p	3.19	6.1	16 Fe--Cα/N_p	3.20	5.6	16 Fe--Cα/N_p	3.20	5.5
Fe--C_h	3.38	3.5	Fe--C_h	3.38	3.2						
Fe--Cβ	4.36	4.8	Fe--Cβ	4.36	4.7	Fe--Cβ	4.37	7.1	Fe--Cβ	4.36	6.7
Fe--Cβ/N_p	4.39	9.6	Fe--Cβ/N_p	4.39	9.4	Fe--Cβ/N_p	4.39	14.2	Fe--Cβ/N_p	4.39	13.4
F		0.342	F		0.321	F		0.406	F		0.393
ΔE_0		7.65	ΔE_0		7.70	ΔE_0		6.21	ΔE_0		5.82

[a] *r* is in units of Å; σ^2 is in units of 10^{-3} $Å^2$. All fits are to unfiltered data. F represents a goodness-of-fit parameter. Fourier transform ranges: $k = 2.0 – 13.85$ $Å^{-1}$ (resolution = 0.134 Å) for *Sw* H-NOX Fe(II)-NO; $k = 2.0 – 12.5$ $Å^{-1}$ (resolution = 0.150 Å) for *Pa* H-NOX Fe(II)-NO. Values of r for the Fe--Cα single scattering and Fe--Cα/N_p multiple scattering paths were constrained to a constant difference from one another, while σ^2 for the multiple scattering path was constrained to be twice that of the single scattering path. A similar constraint was placed on the Cβ and Cβ/N_p combination.

broken in the Fe(II)-NO complexes of *Sw* and *Pa* H-NOX.

We also carried out a detailed full multiple-scattering analysis of EXAFS data obtained for the Fe(II)-unligated forms of *Tt, Sw* and *Pa* H-NOX, the results of which are summarized in Tables 3-4, 3-5 and 3-6. Similar to our observations with the NO-ligated Fe(II) form, the $k^3\chi(k)$ EXAFS data obtained for Fe(II)-unligated *Tt* H-NOX is well simulated by a set of single- and multiple-scattering pathways associated with the 4 pyrrole moieties of the heme group, with an Fe–N_p distance of some 2.02 Å. In contrast to our analysis of the NO-bound form, it is not necessary to include multiple-scattering from a three-body path involving the iron, Cα, and $N_{pyrrole}$ (Fe–Cα/N_p), and indeed fit quality improves markedly when this path is removed (data not shown). The observed 0.05 Å increase in the average Fe–$N_{pyrrole}$ bond length relative to the NO-ligated form is consistent with a high-spin Fe(II) center in unligated *Tt* H-NOX. Attempts to introduce an Fe–N_{His} scatterer having a different bond length than the principal Fe–N_p shell were unsuccessful, affording an unrealistically long Fe–N distance of 2.69 Å (fit 3, Table 3-4). Indeed, computational studies predicted an Fe–N_{His} bond length of 2.05 Å for unligated Fe(II) *Tt* H-NOX. There is evidence for a long, weak Fe–O/N interaction at ca. 2.38 Å (fit 4, Table 3-4) that might be assigned to a bound solvent ligand, but inclusion of this sixth ligand affords only modest improvement in the quality of fit relative to a 5C fit model (compare fits 2 and 4 in Table 3-4 and Figure 3-4).

The complete EXAFS analyses for unligated ferrous forms of *Sw* and *Pa* H-NOX were broadly similar to that of *Tt* H-NOX, in that the EXAFS could be well simulated with a set of 4 – 5 Fe–N/O scatterers at 2.05 – 2.07 Å, as well as single- and multiple-scattering paths associated with the heme pyrroles (Table 3-5 and 3-6). One notable difference in all three cases was that it was not possible to obtain chemically reasonable bond lengths for a putative solvent ligand that

would complete the 6C Fe(II) site expected. In all cases, the Fe–O distance was refined to a value of 2.6 – 2.7 Å, clearly too long to be associated with any significant bonding interaction.

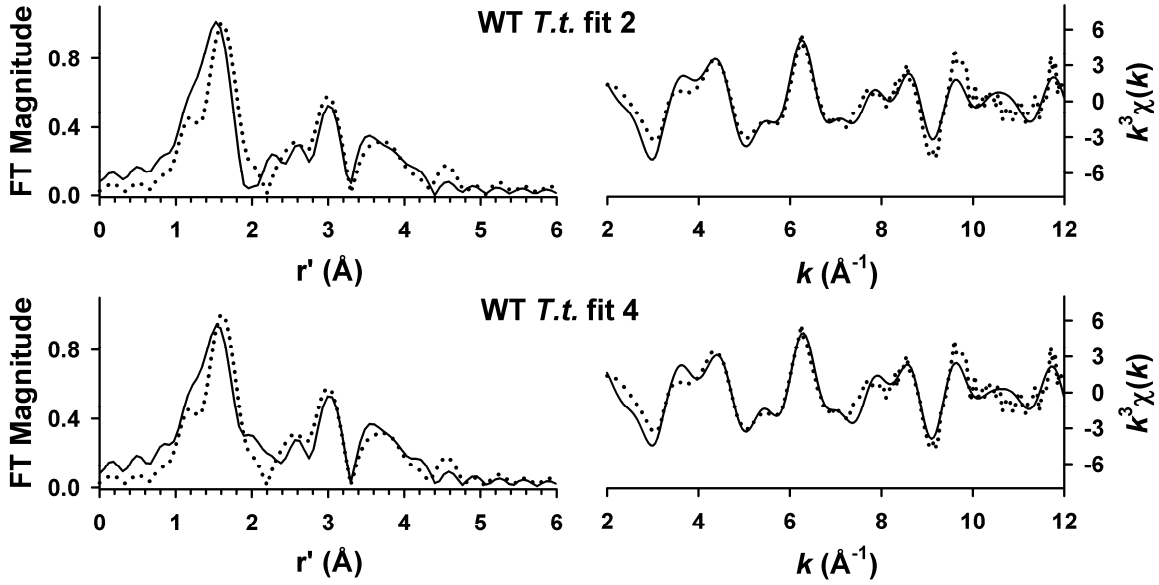

Figure 3-4. Representative best fits to the Fourier transforms of the Fe K-edge EXAFS data ($k^3\chi(k)$, left) and unfiltered EXAFS spectra (k^3 χ (k), right) for *Tt* H-NOX Fe(II)-unligated. Experimental data is shown with dotted lines (•••), fits are shown with solid lines. Fourier transformation range: k = 2 – 12 Å^{-1}. Fit parameters correspond to fit 2 and fit 4 in Table 3-4.

Table 3-4. Selected EXAFS fits for *Tt* H-NOX Fe(II)-unligated.[a]

***Tt* H-NOX Fe(II)-unligated**

fit 1			**fit 2**			**fit 3**			**fit 4**		
shell	r (Å)	σ^2	shell	r (Å)	σ^2	shell	r (Å)	σ^2	shell	r (Å)	σ^2
4 Fe-N_p	2.02	7.2	4 Fe-N_p + 1 Fe-N_{His}	2.02	10.0	4 Fe-N_p	2.02	7.2	4 Fe-N_p + 1 Fe-N_{His}	2.03	10.3
						1 Fe-N_{His}/O	2.69	2.6	1 Fe-O	2.38	3.2
8 Fe--Cα	3.11	13.4	8 Fe--Cα	3.12	15.9	8 Fe--Cα	3.09	15.0	8 Fe--Cα	3.12	14.2
4 Fe--C_h	3.40	-0.3	4 Fe--C_h	3.40	-0.4	4 Fe--C_h	3.40	-0.5	4 Fe--C_h	3.40	-0.8
8 Fe--Cβ	4.39	3.7	8 Fe--Cβ	4.39	4.0	8 Fe--Cβ	4.39	3.8	8 Fe--Cβ	4.39	3.3
16 Fe--Cβ/N_p	4.42	7.5	16 Fe--Cβ/N_p	4.42	8.0	16 Fe--Cβ/N_p	4.42	7.7	16 Fe--Cβ/N_p	4.42	6.7
F		0.381	F		0.436	F		0.362	F		0.411
ΔE_0		4.95	ΔE_0		4.94	ΔE_0		4.98	ΔE_0		4.98

[a] *r* is in units of Å; σ^2 is in units of 10^{-3} $Å^2$. All fits are to unfiltered data. F represents a goodness-of-fit parameter. Fourier transform ranges: k = 2.0 – 12.0 $Å^{-1}$ (resolution = 0.157 Å). Values of r for the Fe--Cβ single scattering and Fe--Cβ/N_p multiple scattering paths were constrained to a constant difference from one another, while σ^2 for the multiple scattering path was constrained to be twice that of the single scattering path.

Table 3-5. Selected EXAFS fits for *Sw* H-NOX Fe(II)-unligated.[a]

***Sw* H-NOX Fe(II)-unligated**

fit 1			**fit 2**			**fit 3**			**fit 4**		
shell	r (Å)	σ^2	shell	r (Å)	σ^2	shell	r (Å)	σ^2	shell	r (Å)	σ^2
4 Fe-N_p	2.07	4.0	4 Fe-N_p + 1 Fe-N_{His}	2.06	5.7	4 Fe-N_p	2.07	4.0	4 Fe-N_p + 1 Fe-N_{His}	2.07	5.8
						1 Fe-N_{His}/O	2.67	14.3	1 Fe-O	2.61	17.6
8 Fe--Cα	3.11	6.1	8 Fe--Cα	3.11	6.6	8 Fe--Cα	3.10	6.3	8 Fe--Cα	3.10	6.9
4 Fe--C_h	3.41	1.0	4 Fe--C_h	3.41	0.55	4 Fe--C_h	3.42	0.9	4 Fe--C_h	3.41	0.5
8 Fe--Cβ	4.43	4.0	8 Fe--Cβ	4.42	3.8	8 Fe--Cβ	4.43	4.0	8 Fe--Cβ	4.42	3.8
16 Fe--Cβ/N_p	4.46	7.9	16 Fe--Cβ/N_p	4.45	7.6	16 Fe--Cβ/N_p	4.46	8.0	16 Fe--Cβ/N_p	4.45	7.65
F		0.276	F		0.301	F		0.261	F		0.287
ΔE_0		4.40	ΔE_0		3.88	ΔE_0		4.62	ΔE_0		4.12

[a] *r* is in units of Å; σ^2 is in units of 10^{-3} Å^2. All fits are to unfiltered data. F represents a goodness-of-fit parameter. Fourier transform ranges: k = 2.0 – 12.0 Å^{-1} (resolution = 0.157 Å). Values of r for the Fe--Cβ single scattering and Fe--Cβ/N_p multiple scattering paths were constrained to a constant difference from one another, while σ^2 for the multiple scattering path was constrained to be twice that of the single scattering path.

Table 3-6. Selected EXAFS fits for *Pa* H-NOX Fe(II)-unligated.[a]

***Pa* H-NOX Fe(II)-unligated**

fit 1			fit 2			fit 3			fit 4		
shell	r (Å)	σ^2	shell	r (Å)	σ^2	shell	r (Å)	σ^2	shell	r (Å)	σ^2
4 Fe-N_p	2.06	3.6	4 Fe-N_p + 1 Fe-N_{His}	2.06	5.2	4 Fe-N_p	2.06	3.7	4 Fe-N_p + 1 Fe-N_{His}	2.06	5.2
						1 Fe-N_{His}/O	2.67	20.4	1 Fe-O	2.57	25.5
8 Fe--Cα	3.10	3.2	8 Fe--Cα	3.10	3.1	8 Fe--Cα	3.10	3.1	8 Fe--Cα	3.10	3.1
4 Fe--C_h	3.41	2.1	4 Fe--C_h	3.40	2.37	4 Fe--C_h	3.41	2.2	4 Fe--C_h	3.41	2.3
8 Fe--Cβ	4.43	3.7	8 Fe--Cβ	4.42	3.9	8 Fe--Cβ	4.43	3.7	8 Fe--Cβ	4.43	3.8
16 Fe--Cβ/N_p	4.45	7.4	16 Fe--Cβ/N_p	4.50	7.7	16 Fe--Cβ/N_p	4.46	7.5	16 Fe--Cβ/N_p	4.45	7.65
F		0.283	F		0.306	F		0.272	F		0.295
ΔE_0		3.63	ΔE_0		3.31	ΔE_0		3.86	ΔE_0		3.66

[a] *r* is in units of Å; σ^2 is in units of 10^{-3} Å^2. All fits are to unfiltered data. F represents a goodness-of-fit parameter. Fourier transform ranges: k = 2.0 – 13.0 Å^{-1} (resolution = 0.142 Å). Values of r for the Fe--Cβ single scattering and Fe--Cβ/N_p multiple scattering paths were constrained to a constant difference from one another, while σ^2 for the multiple scattering path was constrained to be twice that of the single scattering path.

3.4. Conclusion

To explore the detailed molecular basis of NO/H-NOX signaling pathways, we used EXAFS spectra to investigate the Fe(II)-unligated and Fe(II)-NO complexes of three different H-NOX proteins, *Tt* H-NOX, *Sw* H-NOX, and *Pa* H-NOX. We found that NO binds to *Tt* H-NOX in a 6-coordinate manner, while to *Sw* H-NOX and *Pa* H-NOX in a 5-coordinate manner with proximal histidine dissociating away, the same as sGC. Probably due to the severe heme distortion and low electron density on heme iron, the Fe-histidine bond is not broken in *Tt* H-NOX NO-complex although it is substantially lengthened to 2.32 Å. This coordination chemistry is supported by their UV/visible spectra and iron K-edge values. Through comparing the EXAFS fitting results for H-NOX –unligated and –NO complexes, we observed a ~0.07 Å shortening in the Fe-N_p bond lengths upon NO binding for all three different H-NOX proteins; such a contraction in Fe–N_p bond lengths could be important for the signal initiation step of NO sensing.

Chapter 4. An Interesting Structure-Function Correlation of *Tt* H-NOX Determined by EXAFS Studies

Abstract: Hemoproteins ubiquitously exist in living organisms and play critical roles. The activity of the heme cofactor dictates the function of hemoprotein. A family of recently discovered hemoproteins, named Heme-Nitric oxide and/or OXygen binding (H-NOX) proteins, has been found to act as important diatomic molecule sensors in multiple biological systems. A crystal structure of the O_2-bound H-NOX domain from *Thermoanaerobacter tengcongensis* (*Tt* H-NOX) has been solved, showing that this hemoprotein has a severely distorted heme group strained by the packing of several hydrophobic residues including proline 115. Following that, a great amount of studies have been performed on *Tt* H-NOX wildtype (WT) and the P115A mutant. While the crystal structure of P115A *Tt* H-NOX indicates a dramatic change to the heme conformation, subsequent spectroscopic characterizations suggest a minimal perturbation from the mutation. To resolve this contradiction, here we performed a series of structural and ligand binding studies on *Tt* H-NOX WT and the P115A mutant. Results show that the P115A mutation leads to a significant change in the iron-ligand bond length in the Fe(III)-H_2O complex, resulting increased electron density on heme iron and causing the *Tt* H-NOX water-complex to exist as Fe(III)-H_2O in P115A and Fe(III)-OH^- in WT. This finding provides a molecular basis for the greater changes in electronic spectroscopy and ligand binding properties for ferric *Tt* H-NOX. In contrast, the heme structures are very similar between WT and P115A in the ferrous complexes. In summary, our data illustrates how the protein matrix and heme ligation state modulate the

structure and properties of heme cofactor, and how these modulations affect hemoprotein functionalities.

4.1. Introduction

Hemoproteins widely exist in biological systems, playing important roles including diatomic molecule sensing, O_2 transport, electron transfer, *etc.*.[3,10,33,39,46,61,71] The structure and properties of the heme cofactor in hemoproteins are critical for the correct functioning of this family of proteins as the heme serves to either bind signaling molecules in heme-based sensors or to transfer electrons in redox-active heme enzymes. For example, changes in heme planarity caused by O_2 binding have been implicated in the signaling mechanism of the oxygen sensor FixL.[4] Cytochrome c complexes isolated from various species have almost identical non-planar heme structures, suggesting a unique role for that specific heme conformation.[34] In addition, the redox potential of heme group also affects the hemoprotein functions like electron transfer and redox reaction catalysis.[61] Thus, a thorough analysis of the structural and electronic features of heme cofactor is necessary for determining the structure-function relationship of various hemoproteins.

Factors contributing to modulate heme characteristics can be generally classified into two groups, the protein matrix and the heme ligation state. As the heme group is in contact with a large number of residues of the protein matrix, the protein environment can easily exert its influence on the heme cofactor. The porphyrin group is planar when it is free in solution, but adopts an energetically unfavorable distorted conformation when incorporated in hemoproteins. Heme electronic features like reduction potential are also affected by heme pocket residues, changes in which can lead to a change of more than 400 mV in reduction potential.[61,62,64,72-76] Furthermore, the ligation state of hemoprotein complexes, mainly dictated by the iron oxidation state and ligand species, is an important determinant of heme properties as well. Variation of Fe oxidation state and axial ligand has contributed to generate distinctive heme features even within

the same protein fold. For example, during the activation of soluble guanylate cyclase (sGC), while Fe(II)-unligated state shows basal level activity and CO-bound state displays a 2-3 fold activity increase, NO-bound sGC has a several hundred fold increase in enzyme activity; such changes are attributed to varying heme conformations induced by different axial ligands.[15,33] In addition, it has been shown that there is a connection between the extent of heme distortion and the electron density on heme iron.[39] Therefore, a complete understanding of how the properties of heme cofactor are affected could help to solve the molecular details of hemoprotein functioning as well as to rationally design hemoproteins with desirable activities.

We are particularly interested in the Heme-Nitric oxide/OXygen binding (H-NOX) proteins, which are a family of heme-based sensor proteins that have been recently identified to widely exist in both eukaryotes and prokaryotes, playing critical roles in sensing diatomic molecules like NO and O_2.[12,20,24-27] A crystal structure of the O_2-bound H-NOX domain from *Thermoanaerobacter tengcongensis* (*Tt* H-NOX) was solved a few years ago, and it shows that this hemoprotein bears a severely distorted heme cofactor strained by the tightly packing of several highly conserved residues including proline 115 (Figure 1-3 and Figure 1-5).[12] Subsequent crystallographic study on the O_2-bound P115A mutant of *Tt* H-NOX has demonstrated that this mutation results in a much flatter heme plane; the root-mean-square deviation from planarity for P115A is approximately 3-fold less than that for wildtype (WT).[37] Afterwards, WT and P115A *Tt* H-NOX have been extensively used to study heme-protein interactions and how such interactions modulate heme and protein functionalities.

While the P115A mutation leads to significant heme flattening as shown in its crystal structure, a variety of studies indicate that there has actually not been a dramatic change in the ferrous complexes in solution. For example, WT and P115A *Tt* H-NOX have similar UV/visible

and resonance Raman spectra in the ferrous states.[38] Our X-ray Absorption Near-Edge Structure (XANES) analysis has also shown that both the iron K-edge values and ligation-induced iron movement are very similar between WT and P115A *Tt* H-NOX.[36] On the basis of these findings, we observed only minimal perturbations to the ferrous heme and protein properties from the P115A mutation.

However, some studies do show significant alteration in *Tt* H-NOX properties between WT and P115A. The reduction potential for WT *Tt* H-NOX is 167 mV, while that for P115A is only -3.8 mV,[37] implying an electronic environment variance for the Fe(II)/Fe(III) pair in *Tt* H-NOX. This implication was supported by the large shift of Fe(III)-H_2O Soret band in the UV/visible spectra (415 nm for WT *v.s.* 405 nm for P115A).[35,39] Moreover, cyanide binding rate to ferric *Tt* H-NOX is severely changed. We have found that cyanide binds to WT Fe(III) almost 2000 times faster than to P115A Fe(III).[36] Interestingly, these dramatic changes induced by P115A mutation are all related to the ferric states of *Tt* H-NOX, which lead to our hypothesis that, for this interesting hemoprotein, environmental changes to the heme cofactor (like the one caused by P115A mutation) induce a much more dramatic change to the ferric state; in other words, *Tt* H-NOX Fe(III)-H_2O state more sensitively monitors heme local changes.

To test this hypothesis and also to gain insight into the structure-function relationship of this important family of proteins, we performed a series of H-NOX structural and ligand binding characterizations. Our Extended X-ray Absorption Fine Structure (EXAFS) results show that the P115A mutation leads to a significant lengthening to the iron-ligand bond lengths in the Fe(III)-H_2O complex causing increased electron density on heme iron, which makes the *Tt* H-NOX water-complex exist as Fe(III)-H_2O in P115A and Fe(III)-OH^- in WT. For ferrous complexes, the heme structures are very similar between WT and P115A. The importance of this finding is that

it provides a molecular basis for the changes in the properties of ferric WT and P115A *Tt* H-NOX that we have observed. In addition, we found that ligand binding kinetics are more greatly affected in the ferric state, which further supports our hypothesis. Our data illustrates how the protein matrix and heme ligation state modulates heme structure and properties in the H-NOX family, and how these modulations influence function.

4.2. Materials and Methods

Plasmid preparation and protein expression. Cloning of the *Tt* H-NOX domain into a pET-20b (Novagen) vector has been described previously.[21] For ease of purification, a C-terminal 6×His tag was incorporated to the plasmid ahead of the stop codon. P115A mutagenesis of the 6×His tagged protein construct was carried out using the QuikChange® protocol from Stratagene. Cell culture preparation and expression procedures of H-NOX proteins were carried out as previously described.[36]

Protein purification. Cell lysis and thermal denaturation treatments were carried out as described.[21] The supernatant after thermal denaturation was filtered through a 0.45 µm membrane and the filtrate was applied to a 1 mL HisTrap HP column (GE Life Sciences) pre-equilibrated with buffer A [50 mM sodium phosphate, 300 mM NaCl, pH 7.5]. The column loaded with *Tt* H-NOX was washed using 30 mL buffer A and then three more washes were performed using 20 mL buffer A with 10 mM imidazole, 20 mL buffer A with 20 mM imidazole, and 10 mL buffer A with 50 mM imidazole. The protein was ultimately eluted using buffer A with 250 mM imidazole. The flow rate was controlled at 1 mL/min. The protein was then exchanged into buffer B [50 mM HEPES, 50 mM NaCl, 5% glycerol and 5 mM DTT, pH 7.5]

using a PD-10 column (GE Healthcare), aliquoted, and stored at -80 °C. This procedure (thermal denaturation plus affinity chromatography) resulted in protein that was >95% pure as estimated by SDS-PAGE.

XAS sample preparation. Ferrous (-unligated and -NO) complexes of H-NOX were prepared in the glove bag as previously described.[21] The Fe(III)-H_2O complex was prepared by oxidizing the protein sample with 10-20 mM potassium ferricyanide followed by desalting with a PD-10 column. Protein samples were exchanged into buffer C [50 mM HEPES, 50 mM NaCl, 10% glycerol, pH 7.5] and concentrated to 1-2 mM using spin columns from Millipore [Microcon Ultracel YM-3, 3000 molecular weight cut off (MWCO) and 0.5 mL maximum volume]. The concentrated protein samples were transferred to copper sample holders with Mylar windows (10 mm wide × 5 mm high × 0.5 mm thick), frozen in liquid nitrogen and stored at -80 °C before XAS experiments.

X-ray absorption spectroscopy. XAS data collection was carried out at the National Synchrotron Light Source (NSLS) at Brookhaven National Laboratory (BNL), on beamline X3B with a sagittally focused Si (111) crystal monochromator. Samples were cooled to at least 40 K before scanning in a closed-cycle liquid helium diplex and kept frozen during data collection. K_α fluorescence was detected with a Canberra 13-element germanium detector. An iron foil was used as a reference to determine the X-ray absorption edge for each spectrum and to account for any shifts in the monochromator. The step size at the edge region was set to 0.2 eV. 6-9 scans for each complex were taken and averaged for data analysis. In order to minimize radiation damage to the samples, we made multiple samples for the same complex and collected at most 2 scans per X-ray exposed spot. XAS data were aligned, background-removed, normalized and merged using Athena. The K-edge positions were determined from the first derivative of the average

XAS spectra after smoothing. The derivative spectra were smoothed using Origin 7.0. EXAFS fitting of all data were carried out using EXAFSPAK.

4.3. Results and Discussion

Significant structure and property changes in ferric Tt H-NOX induced by P115A. To study how the ferric *Tt* H-NOX is affected by heme environment change, we first analyzed the EXAFS spectra of *Tt* H-NOX WT and P115A ferric complexes. Significant differences in the EXAFS for WT and P115A are observed for the Fe(III)-H_2O form (Table 4-1 and 4-2). The WT complex can be best fit with 4-5 Fe–N/O scatterers at 1.96 Å and 1 Fe–O/N scatterers at approximately 2.3 Å, reflecting the contributions of the pyrrole and axial His nitrogens and the bound solvent ligand. Conversely, the principal Fe–N/O distance of 2.02 Å in P115A Fe(III)-H_2O is 0.06 Å longer than that of WT. Moreover, the Debye-Waller factor for this shell is larger in P115A, reflecting substantial static disorder in the bond lengths. Such an increase in bond lengths and bond length disorder in P115A correlates very well with previous structural characterizations. As shown from the P115A Fe(II)-O_2 crystal structure and resonance Raman spectra, substitution of the bulky proline with an alanine highly relaxes the heme cofactor and introduces large heterogeneity to the H-NOX domain.[37,38]

Table 4-1. Selected EXAFS fits for WT *Tt* H-NOX Fe(III)-H_2O.[a]

WT *Tt* H-NOX Fe(III)-H_2O

fit 1			**fit 2**			**fit 3**			**fit 4**		
shell	r (Å)	σ^2	shell	r (Å)	σ^2	shell	r (Å)	σ^2	shell	r (Å)	σ^2
4 Fe-N_p	1.96	1.5	4 Fe-N_p + 1 Fe-N_{His}	1.96	2.9	4 Fe-N_p	1.96	1.7	4 Fe-N_p + 1 Fe-N_{His}	1.96	3.2
						1 Fe-O	2.31	1.5	1 Fe-O	2.29	2.0
8 Fe--Cα	2.98	5.7	8 Fe--Cα	2.98	6.0	8 Fe--Cα	2.99	5.9	8 Fe--Cα	2.99	6.0
16 Fe--Cα/N_p	3.15	11.4	16 Fe--Cα/N_p	3.15	12.1	16 Fe--Cα/N_p	3.16	11.9	16 Fe--Cα/N_p	3.16	11.9
4 Fe--C_h	3.38	0.6	4 Fe--C_h	3.38	1.0	4 Fe--C_h	3.37	1.2	4 Fe--C_h	3.37	2.2
8 Fe--Cβ	4.34	4.7	8 Fe--Cβ	4.33	4.4	8 Fe--Cβ	4.32	4.2	8 Fe--Cβ	4.33	4.8
16 Fe--Cβ/N_p	4.37	9.4	16 Fe--Cβ/N_p	4.36	8.9	16 Fe--Cβ/N_p	4.35	8.4	16 Fe--Cβ/N_p	4.36	9.7
F		0.307	F		0.314	F		0.309	F		0.295
ΔE_0		4.18	ΔE_0		3.61	ΔE_0		3.10	ΔE_0		3.69

[a] *r* is in units of Å; σ^2 is in units of 10^{-3} $Å^2$. All fits are to unfiltered data. F represents a goodness-of-fit parameter. Fourier transform range k = 2.0 – 12.5 $Å^{-1}$ (resolution = 0.150 Å). Values of r for the Fe--Cα single scattering and Fe--Cα/N_p multiple scattering paths were constrained to a constant difference from one another, while σ^2 for the multiple scattering path was constrained to be twice that of the single scattering path. A similar constraint was placed on the Cβ and Cβ/N_p combination.

Table 4-2. Selected EXAFS fits for P115A *Tt* H-NOX Fe(III)-H_2O.[a]

P115A *Tt* H-NOX Fe(III)-H_2O

fit 1			**fit 2**			**fit 3**			**fit 4**		
shell	r (Å)	σ^2	shell	r (Å)	σ^2	shell	r (Å)	σ^2	shell	r (Å)	σ^2
4 Fe-N_p	2.03	6.4	4 Fe-N_p + 1 Fe-N_{His}	2.02	8.9	4 Fe-N_p	2.02	6.8	4 Fe-N_p + 1 Fe-N_{His}	2.02	9.1
						1 Fe-O	2.43	6.9	1 Fe-O	2.41	5.7
8 Fe--Cα	3.10	6.6	8 Fe--Cα	3.09	7.5	8 Fe--Cα	3.09	7.7	8 Fe--Cα	3.09	7.7
16 Fe--Cα/N_p	3.27	13.3	16 Fe--Cα/N_p	3.27	15.1	16 Fe--Cα/N_p	3.27	15.4	16 Fe--Cα/N_p	3.27	15.5
4 Fe--C_h	3.41	4.9	4 Fe--C_h	3.41	3.7	4 Fe--C_h	3.41	2.9	4 Fe--C_h	3.40	2.5
8 Fe--Cβ	4.44	7.0	8 Fe--Cβ	4.42	6.1	8 Fe--Cβ	4.41	6.3	8 Fe--Cβ	4.40	6.1
16 Fe--Cβ/N_p	4.47	13.9	16 Fe--Cβ/N_p	4.44	12.3	16 Fe--Cβ/N_p	4.44	12.7	16 Fe--Cβ/N_p	4.43	12.3
F		0.453	F		0.479	F		0.448	F		0.458
ΔE_0		3.15	ΔE_0		1.71	ΔE_0		1.20	ΔE_0		0.75

[a] *r* is in units of Å; σ^2 is in units of 10^{-3} $Å^2$. All fits are to unfiltered data. F represents a goodness-of-fit parameter. Fourier transform range k = 2.0 – 12.0 $Å^{-1}$ (resolution = 0.157 Å). Values of r for the Fe--Cα single scattering and Fe--Cα/N_p multiple scattering paths were constrained to a constant difference from one another, while σ^2 for the multiple scattering path was constrained to be twice that of the single scattering path. A similar constraint was placed on the Cβ and Cβ/N_p combination.

The heme structural changes and accompanied protein structural rearrangement is likely the cause for increased electron density on heme iron in P115A *Tt* H-NOX. This difference in heme iron electric field makes P115A bind water as Fe(III)-H_2O while WT bind as Fe(III)-OH^- to compensate for the lower electron density. Such a ligation state change subsequently alters the light absorption of *Tt* H-NOX, causing a blue shift in the Soret band from 415 nm (WT) to 405 nm (P115A) and a color change from bright red (WT) to dark brown (P115A). A higher electron density at Fe(III) state also leads to a lower Fe(III)/Fe(II) reduction potential, which is consistent with previously reported values for WT and P115A.[37] Although it has been shown that heme porphyrins with more severe saddling tend to have more positive reduction potentials and protein-induced porphyrin distortion may alter heme electronic properties, our studies further elaborated the molecular details of such porphyrin distortion and its correlation with heme electrostatic environment.

The structural and electronic differences are also the molecular basis of the changes in ligand binding kinetics for *Tt* H-NOX ferric complexes. We have determined that cyanide binds to WT Fe(III) almost 2000 times faster than to P115A Fe(III).[36] As the Fe-N_p bond lengths are much shorter in WT, there is a larger steric strain for the axial ligand, making the OH^- group in WT Fe(III) complex more readily dissociate and facilitating the cyanide association. Besides, the hydrophobic atmosphere at the *Tt* H-NOX distal pocket would also make OH^- a better leaving group. Therefore, our work here establishes the molecular basis for the dramatic property changes in ferric *Tt* H-NOX.

Minimal structure and property changes in ferrous Tt H-NOX induced by P115A. The EXAFS studies on WT *Tt* H-NOX Fe(II)-unligated and Fe(II)-NO states have been shown in Chapter 3. Here we have also analyzed the EXAFS spectra of the complexes for the P115A

mutant. In contrast to the ferric states, the Fe-N_p bond lengths are very similar for the ferrous complexes of WT and P115A. The first shell EXAFS for both Fe(II)-unligated WT and P115A *Tt* H-NOX principally consists of 4-5 Fe–N atoms located at 2.02 – 2.06 Å (Table 3-4 and Table 4-3), attributable to the equatorial pyrrole nitrogens and perhaps the axially bound His residue. In addition, based on the comparison of the full fitting results for WT and P115A Fe(II)-NO complexes (Table 3-2 and Table 4-4), the Fe-NO, Fe-N_p and Fe-N_{His} bond lengths are almost identical, suggesting that P115A induces minimal changes to the NO complexes.

NO dissociation rates were also measured for WT and P115A Fe(II)-NO complexes to examine how the kinetics is influenced by the mutation. As the results shown in Chapter 6 (Table 6-1), the rate constants are 0.042 min^{-1} and 0.026 min^{-1} for WT and P115A respectively, a less than 2-fold alteration. As compared to the substantial kinetics change in cyanide binding to ferric *Tt* H-NOX, this rate change for P115A is truly minimal.

Table 4-3. Selected EXAFS fits for P115A *Tt* H-NOX Fe(II)-unligated.[a]

***Tt* H-NOX P115A Fe(II)-unligated**

fit 1			**fit 2**			**fit 3**			**fit 4**		
shell	r (Å)	σ^2	shell	r (Å)	σ^2	shell	r (Å)	σ^2	shell	r (Å)	σ^2
4 Fe-N_p	2.05	4.1	4 Fe-N_p + 1 Fe-N_{His}	2.05	6.0	4 Fe-N_p	2.05	4.2	4 Fe-N_p + 1 Fe-N_{His}	2.05	6.1
						1 Fe-N_{His}/O	2.70	2.5	1 Fe-O	2.69	2.6
8 Fe--Cα	3.10	9.0	8 Fe--Cα	3.10	9.5	8 Fe--Cα	3.08	9.7	8 Fe--Cα	3.08	10.6
4 Fe--C_h	3.40	0.9	4 Fe--C_h	4.41	4.09	4 Fe--C_h	3.41	0.6	4 Fe--C_h	3.40	0.2
8 Fe--Cβ	4.42	4.2	8 Fe--Cβ	4.44	8.2	8 Fe--Cβ	4.42	4.2	8 Fe--Cβ	4.42	3.9
16 Fe--Cβ/N_p	4.45	8.5	16 Fe--Cβ/N_p	3.40	0.5	16 Fe--Cβ/N_p	4.45	8.5	16 Fe--Cβ/N_p	4.44	7.88
F		0.331	F		0.379	F		0.305	F		0.359
ΔE_0		5.23	ΔE_0		4.61	ΔE_0		5.32	ΔE_0		4.74

[a] *r* is in units of Å; σ^2 is in units of 10^{-3} $Å^2$. All fits are to unfiltered data. F represents a goodness-of-fit parameter. Fourier transform ranges: k = 2.0 – 12.0 $Å^{-1}$ (resolution = 0.157 Å). Values of r for the Fe--Cβ single scattering and Fe--Cβ/N_p multiple scattering paths were constrained to a constant difference from one another, while σ^2 for the multiple scattering path was constrained to be twice that of the single scattering path.

Table 4-4. Selected EXAFS fits to P115A *Tt* H-NOX Fe(II)-NO.[a]

***Tt* H-NOX P115A Fe(II)-NO**

fit 1			**fit 2**			**fit 3**			**fit 4**		
shell	r (Å)	σ^2	shell	r (Å)	σ^2	shell	r (Å)	σ^2	shell	r (Å)	σ^2
			1 Fe-NO	1.72	2.9	1 Fe-NO	1.72	1.5	1 Fe-NO	1.72	3.0
4 Fe-N_p	1.99	3.3	4 Fe-N_p	1.98	3.4	4 Fe-N_p + 1 Fe-N_{His}	1.97	5.3	4 Fe-N_p	1.98	3.4
									1 Fe-N_{His}	2.31	8.8
8 Fe--Cα	3.02	3.1	8 Fe--Cα	3.01	3.0	8 Fe--Cα	3.01	2.9	8 Fe--Cα	3.01	3.0
16 Fe--Cα/N_p	3.19	6.2	16 Fe--Cα/N_p	3.18	6.0	16 Fe--Cα/N_p	3.18	5.7	16 Fe--Cα/N_p	3.18	5.9
Fe--C_h	3.36	5.6	Fe--C_h	3.35	5.0	Fe--C_h	3.35	5.7	Fe--C_h	3.35	4.6
Fe--Cβ	4.36	5.0	Fe--Cβ	4.33	5.0	Fe--Cβ	4.33	4.8	Fe--Cβ	4.33	5.0
Fe--Cβ/N_p	4.39	10.0	Fe--Cβ/N_p	4.36	9.9	Fe--Cβ/N_p	4.36	9.7	Fe--Cβ/N_p	4.36	9.9
F		0.449	F		0.330	F		0.349	F		0.325
ΔE_0		6.14	ΔE_0		4.01	ΔE_0		3.95	ΔE_0		3.81

[a] *r* is in units of Å; σ^2 is in units of 10^{-3} $Å^2$. All fits are to unfiltered data. F represents a goodness-of-fit parameter. Fourier transform range k = 2.0 – 13.55 $Å^{-1}$ (resolution = 0.138 Å). Values of r for the Fe--Cα single scattering and Fe--Cα/N_p multiple scattering paths were constrained to a constant difference from one another, while σ^2 for the multiple scattering path was constrained to be twice that of the single scattering path. A similar constraint was placed on the Cβ and Cβ/N_p combination.

4.4. Conclusion

In this study, we focused on analyzing how the P115A mutation differently affects the structure and functions of the ferric and ferrous states of *Tt* H-NOX. Our EXAFS results show that this mutation causes a significant change to the iron-ligand bond lengths in Fe(III)-H_2O complex and hence increases the electron density on heme iron. Therefore, the *Tt* H-NOX water-complex exit as Fe(III)-H_2O in P115A, while in WT a proton dissociates away generating the Fe(III)-OH^- complex to compensate for the low Fe electron density. While for ferrous complexes, the heme structures are very similar between WT and P115A. Further, ligand binding kinetics is more greatly affected at the ferric state, which confirms our hypothesis. Moreover, our data illustrates how protein matrix and heme ligation state modulate heme structure and properties, and how these modulations affect H-NOX functioning.

Chapter 5. Engineering of *Tt* H-NOX for Direct Cyanide Detection and Quantification

Abstract: A new cyanide sensing system, the Heme-Nitric oxide and/or OXygen binding domain (H-NOX domain) from *Thermoanaerobacter tengcongensis* (*Tt* H-NOX), has been investigated. With straightforward absorbance-based detection, we have achieved a cyanide detection limit of 0.5 μM (~10 ppb) with an upper detection range that is adjustable with protein concentration. We find a linear correlation of multiple spectroscopic features with cyanide concentration. These spectroscopic features include the Soret band maximum and absorbance changes in both the Soret and α/β band regions of the spectrum. Multiple probes for cyanide detection makes sensing with *Tt* H-NOX unique compared to other cyanide sensing methods. Furthermore, using site-directed mutagenesis, we have rationally engineered the heme pocket of *Tt* H-NOX to improve its cyanide sensing properties. We were able to introduce colorimetric detection and enhance anion selectivity in P115A *Tt* H-NOX. Through substituting phenylalanine 78 with a smaller (valine, F78V) or a larger residue (tyrosine, F78Y), we demonstrate a correlation with distal pocket steric crowding and affinity for cyanide. In particular, F78V *Tt* H-NOX shows a significant increase in CN^- binding affinity and selectivity. Thus, we demonstrate the ability to fine-tune the affinity and specificity of *Tt* H-NOX for cyanide, suggesting that *Tt* H-NOX can be readily tailored into a practical cyanide sensor.

5.1. Introduction

Cyanide is well known for its extreme toxicity to mammals, due to its ability to bind to the active site of cytochrome oxidase and inhibit cellular respiration.[77] Cyanide poisoning can lead to vomiting, convulsions, unconsciousness and most severely, death. However, cyanide is still widely used in industrial fields, including electroplating, metal mining, and plastic manufacture. Accidental leaks and spills of cyanide can lead to disastrous consequences.[78] Therefore, it is highly desirable to develop safe, simple, and direct sensing techniques for cyanide detection and quantification.

As suggested by the World Health Organization, the maximum acceptable level of cyanide in drinking water is 1.9 μM.[79] Thus, numerous analytical techniques have been developed to detect and quantify cyanide at sub-micromolar concentrations. Probes including silver electrode,[80] boronic acids,[81] cationic boranes,[82,83] cobalt corrinoids,[84,85] benzil,[86] coumarin with a salicylaldehyde moiety,[87] acridinium salt,[88] and oxazines,[89,90] *etc*, have been used in amperometric, chromatographic, fluorometric, and colorimetric assays for cyanide detection.[80-98] These systems, however, either require sophisticated equipment and/or laborious sample pretreatment, or are subject to interference by other anions.[80,98] Additionally, some of the cyanide detectors are organic materials that require laborious synthesis and usually have poor water solubility.[88,95] Although efforts have been made to design cyanide sensors that function in aqueous solution, a certain percentage of organic solvent is often required in the detection media for those organic probes.[82,86,88,91,95] Thus, new water soluble cyanide detection techniques with high sensitivity and selectivity, that are easily accessed without relying on complicated analytical processes, are desired. Here, we introduce a new cyanide sensing system: the Heme-Nitric oxide

and/or OXygen binding domain (H-NOX domain) from *Thermoanaerobacter tengcongensis* (*Tt* H-NOX).[12]

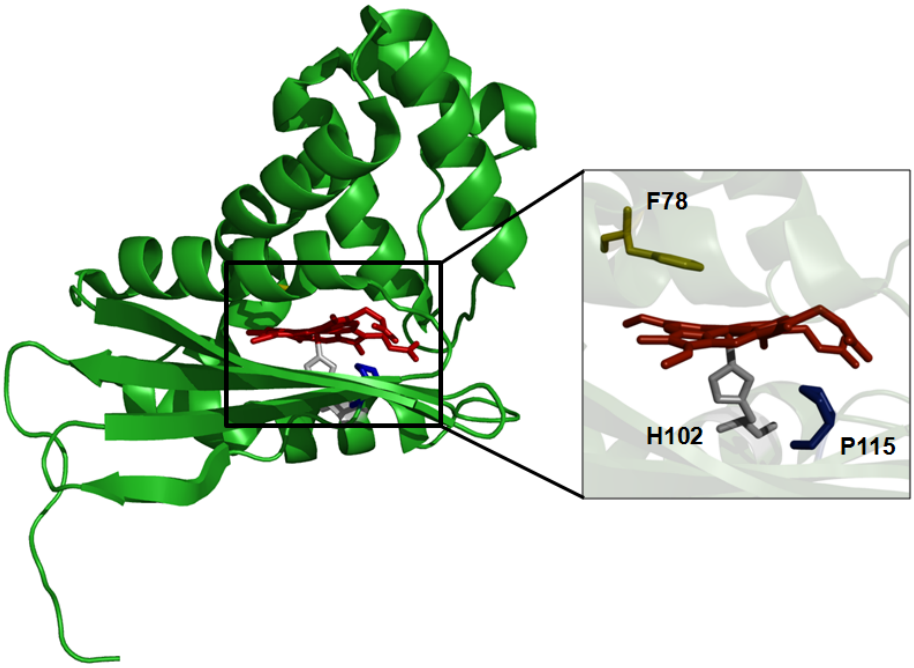

Figure 5-1. Crystal structure of *Tt* H-NOX (PDB 1U55). P115, F78 and H102 residues are colored in blue, yellow and gray, respectively.

It is well established that cyanide binds to hemoproteins and induces absorbance changes to the UV/visible spectra of the protein. Nonetheless, *Tt* H-NOX has many intriguing features that make it a unique new candidate for a cyanide sensor. H-NOX proteins are a family of recently discovered diatomic gas binding and sensing hemoproteins that are highly homologous to soluble guanylate cyclase (sGC), the well-studied nitric oxide (NO) sensor in eukaryotes.[41] The *Tt* H-NOX domain has been well characterized: (1) the crystal structure of wildtype (WT) *Tt* H-NOX has been solved to a resolution of 1.77 Å (Figure 5-1);[12] (2) it can be easily over-expressed and purified;[21] (3) it is very soluble in water; (4) as it was isolated from a thermophilic

bacterium living at 75 °C, it is extremely stable at room temperature and can tolerate high temperatures; (5) its fold is tolerant of mutagenesis;[28,37] (6) its ferric state binds cyanide very tightly, while its ferrous state shows no affinity for cyanide;[99] and (7) the heme of *Tt* H-NOX can be easily converted between ferrous and ferric states, which should facilitate its use as a reusable cyanide indicator. Furthermore, mutants of *Tt* H-NOX have already been proven to be robust protein sensors of small molecules; Y140F *Tt* H-NOX has been used as a nitric oxide sensor.[100]

In this work, we have explored the application of *Tt* H-NOX as a sensitive and specific cyanide sensor in an assay based on UV/visible absorbance changes. *Tt* H-NOX senses CN^- with a detection limit of 0.5 μM (at the level of 10 ppb), which is much more sensitive than recently reported optical sensor based on hemoglobin (~0.2 ppm).[96] We demonstrate that the well characterized *Tt* H-NOX P115A mutant has improved CN^- sensing properties, in particular, affording increased anion selectivity and colorimetric detection. Based on a comparison of WT and P115A *Tt* H-NOX, we develop a model relating heme distal pocket steric hindrance to CN^- binding properties in *Tt* H-NOX. Using this model, the CN^- binding properties of three additional mutants (P115F, F78V and F78Y) are predicted and tested. All three of these mutants have spectral changes that linearly correspond to cyanide concentration and all of them show better anion selectivity than the WT analog. As predicted, F78V binds cyanide with the highest affinity.

5.2. Materials and Methods

Protein expression and purification. Plasmids for WT and P115A *Tt* H-NOX were generated in previous studies.[99] Site-directed mutagenesis for other *Tt* H-NOX mutants was carried out as described.[99] Mutagenesis for P115F was carried out using primers 5'-

ggagccactcctttcaggcttattgcaaagcctgttgc-3' and its reverse complement. Mutagenesis for F78V was carried out using primers 5'-ggaaggcagaacataaaaactgtcagcgaatggtttccctcc-3' and its reverse complement. Mutagenesis for F78Y was carried out using primers 5'-ggaaggcagaacataaaaacttacagcgaatggtttccctcc-3' and its reverse complement. Over-expression, purification and storage of all H-NOX proteins were carried out as previously described.[99]

Cyanide detection. All cyanide quantification and ligand binding affinity experiments were carried out in 50 mM HEPES buffer, pH 7.5 at 20 °C unless otherwise noticed. The KCN solutions were prepared freshly before use. All UV/visible spectra were obtained using a Cary 100 Bio Spectrophotometer (Varian, now Agilent Technologies).

All WT and mutant *Tt* H-NOX discussed here are in their ferric states. In a typical cyanide detection experiment, *Tt* H-NOX ferric protein was produced by oxidizing the protein with 15-100 mM potassium ferricyanide; excess potassium ferricyanide and product ferrocyanide were removed by desalting through a PD-10 column (GE Healthcare). After desalting, protein concentration was measured based on its UV/visible absorbance (Beer-Lambert law). Next, titration of the protein with cyanide was performed through adding increasing amount of cyanide-from 0 μM to more than twice as the sensor amount-to separate protein samples. After the binding reached equilibrium (when there was no further spectral change), the UV/visible spectra for all samples were taken. Excel was first used to normalize the spectral data and extract absorbance changes at the Soret band region and the β/α region. Origin 7.0 was then utilized to fit the absorbance changes with cyanide concentration. For colorimetric cyanide detection based on P115A *Tt* H-NOX, cyanide was added to the sensor solution and photos were taken after 10 minutes.

Anion selectivity assay. To study the anion selectivity of *Tt* H-NOX as cyanide sensor, extra amount (100 equivalents anions for WT and 200 equivalents anions for P115A) of potential interfering anions, including SO_4^{2-} (Na_2SO_4), AcO^- (NaOAc), HCO_3^- ($NaHCO_3$), F^- (NaF), Cl^- (NaCl), Br^- (NaBr), I^- (NaI), NO_3^- ($NaNO_3$), $C_2O_4^{2-}$ ($Na_2C_2O_4$), ClO_4^- ($KClO_4$), SCN^- (NaSCN), phosphate (NaH_2PO_4) and EDTA (sodium salt), were added to the *Tt* H-NOX sensor solution, separately. UV/visible spectra of all samples were taken to check if the anions perturb the spectrum. To test the selectivity of P115A *Tt* H-NOX as a colorimetric probe, photos were also taken after 10 minutes following the addition of various anions.

Cyanide and fluoride binding affinity. Spectrophotometric equilibrium titrations of *Tt* H-NOX ferric proteins with cyanide and fluoride were performed at 20 °C using UV/visible spectroscopy. Ligand binding was followed using the Soret band shift. Difference spectra were calculated by subtracting the first scan (the sample with 0 mM anion) from subsequent scans (samples with increasing anion amount). The equilibrium dissociation constants (K_D) of all proteins for CN^- and F^- were determined by plotting maximal absorbance difference for each scan versus cyanide concentration and curve fitting with the following equation: [101]

$$\Delta A = \Delta A_{max} ([P] + [L] + K_D - (([P] + [L] + K_D)^2 - 4[P] [L])^{1/2}) / 2[P] \qquad \textbf{(Equation 5-1)}$$

where ΔA is the absorbance difference; ΔA_{max} is the maximum absorbance difference when all the ferric heme molecules are occupied with anion; [P] and [L] are the total protein and total anion concentration respectively; and K_D is the equilibrium dissociation constant.

5.3. Results and Discussion

Simple and inexpensive techniques for cyanide detection and quantification at the sub-micromolar level are required. *Tt* H-NOX detects CN^- at the 10 ppb level and affords multiple handles for cyanide sensing, including visual detection, which makes it unique compared to other small-molecule probes. Further, cyanide sensing can be fine-tuned by rational engineering of the H-NOX heme pocket.

Tt H-NOX is a sensitive and selective CN^- sensor. We first investigated the quantification of cyanide with WT *Tt* H-NOX. Cyanide was added to 6 μM ferric WT *Tt* H-NOX solutions to final concentrations of 0-20 μM. The binding reached equilibrium within 75 minutes at 20 °C, and when the temperature was increased to 37 °C, the reaction time decreased to 45 min. Because *Tt* H-NOX is a thermo-stable protein, we can further increase the cyanide association rate and shorten the reaction time using temperature.

UV/visible spectroscopy of *Tt* H-NOX in reaction with varying concentrations of CN^- revealed that with increasing cyanide concentration (until ~6 μM, the concentration of H-NOX in the reaction), the Soret band shifts from 415.4 nm to 420.6 nm (Figure 5-2A), which is attributed to the replacement of a water molecule or hydroxide anion with cyanide at the distal binding site of the heme pocket. We plotted the change in absorbance of ferric WT *Tt* H-NOX upon cyanide addition verses cyanide concentration and obtained a good linear relationship until the concentration of cyanide exceeded the concentration of the sensor (6 μM), implying strong, one-to-one binding (Figure 5-2B). We also found that the β/α absorbance band ratio linearly correlates with cyanide concentration (Figure 5-2C). Interestingly, we observed a linear response in the Soret band maximum as a function of cyanide concentration (from 0 to 6 μM), which

indicates that we can quantify cyanide in an unknown sample simply based on reading the Soret band maximum from the UV/visible spectrum (Figure 5-2D).

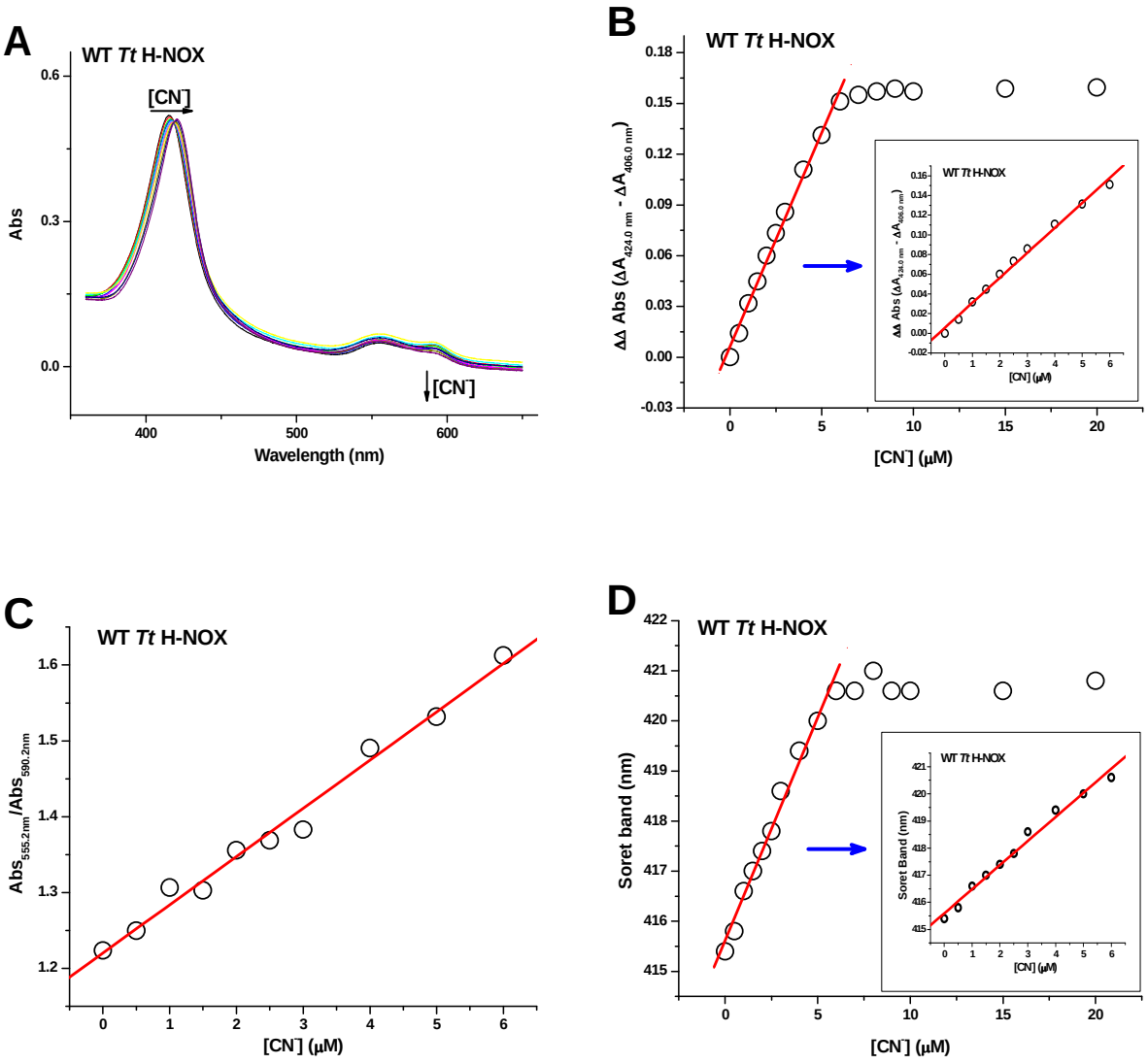

Figure 5-2. Quantification of cyanide using 6 μM WT *Tt* H-NOX. A. UV/visible spectral shifts upon cyanide addition; B, C, D. Cyanide detection based on the absorbance changes at the Soret band region (B) and the β/α band region (C), and based on Soret band maximum shift (D). R^2 = 0.99.

The detection limit is as low as 0.5 µM with a detection range of 0-6 µM in this assay. We can broaden the detection range by increasing the sensor concentration since CN^- binding is one-to-one with respect to protein. We repeated this experiment using 30 µM ferric WT *Tt* H-NOX, and as expected, found that the Soret band and β/α band ratio are both linearly correlated with the cyanide concentration to as much as 30 µM (Figure 5-3), which is described as the necessary cyanide monitoring range for human physiological safeguard.[81] These multiple sensing features, especially the direct cyanide quantification based on the Soret band maximum, render *Tt* H-NOX an excellent candidate for cyanide detection and quantification.

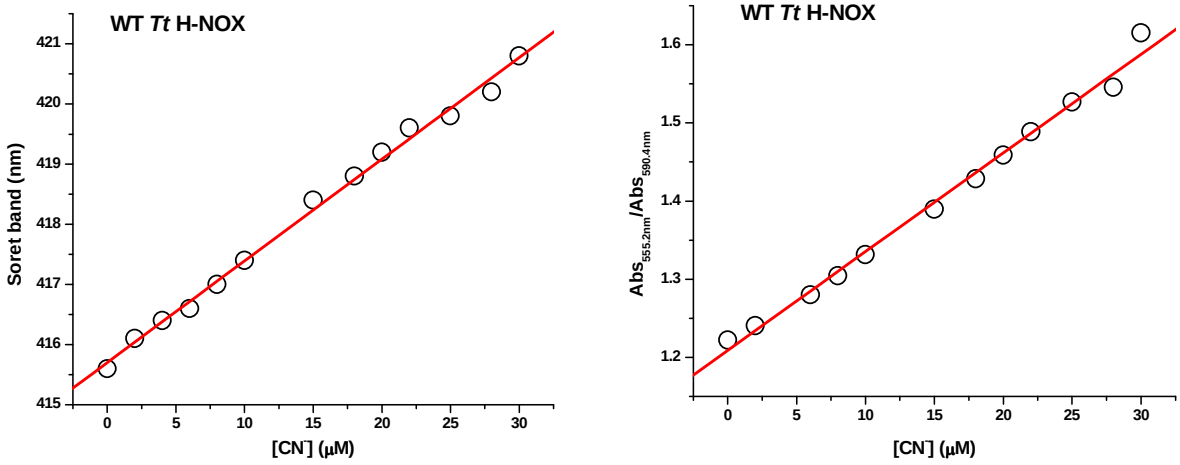

Figure 5-3. The Soret band maximum and β/α band ratio correlate with cyanide concentration (addition of 0-30 µM cyanide to 30 µM WT *Tt* H-NOX). $R^2 = 0.99$.

To examine the selectivity of WT *Tt* H-NOX, 100 equivalents (600 µM) of various anions, including SO_4^{2-}, AcO^-, HCO_3^-, F^-, Cl^-, Br^-, I^-, NO_3^-, $C_2O_4^{2-}$, ClO_4^-, SCN^-, phosphate and EDTA, were added separately to the sensor solution (6 µM). None of the anions tested caused a change to the spectrum of WT *Tt* H-NOX, except for F^- (Figure 5-4A). Weak binding of F^- to the ferric heme brought about a small but consistent blue shift (~0.4 nm) to the Soret band

maximum. Cyanide was then added (6 µM) to each anion test sample, which caused the Soret band in each sample (including the F^- sample) to shift to 420.6 nm, indicative of formation of the Fe^{3+}-CN^- complex (Figure 5-4B).

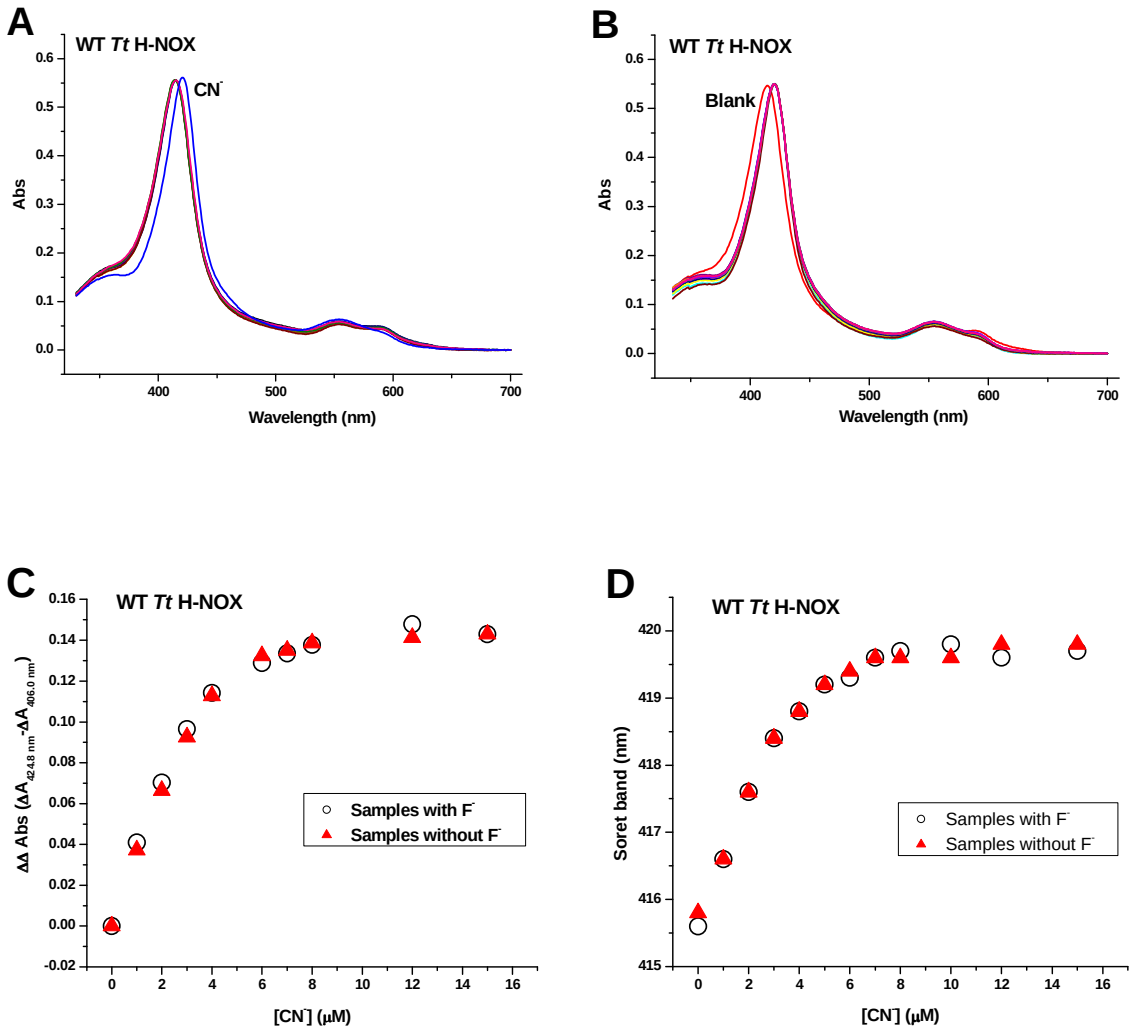

Figure 5-4. Anion selectivity of WT *Tt* H-NOX. A. Spectra of WT *Tt* H-NOX (6 µM) after the addition of buffer only (blank) and 600 µM SO_4^{2-}, AcO^-, HCO_3^-, F^-, Cl^-, Br^-, I^-, NO_3^-, $C_2O_4^{2-}$, ClO_4^-, SCN^-, phosphate, EDTA or CN^-. Only the cyanide sample (blue curve) yields a typical red-shift and the fluoride sample gives a ~0.4 nm blue-shift; B. Spectra of WT *Tt* H-NOX (6 µM) after adding cyanide (6 µM) to samples in the presence of various existing anions (from above). All samples give typical cyano-complex spectra and only the blank sample (red curve), to which no CN^- was added, yields no spectral change. C, D. Soret band absorbance change and Soret band maximum shift of WT *Tt* H-NOX (6 µM) upon the addition of cyanide (0-15 µM) with and without the presences of 100 equivalents of fluoride (600 µM).

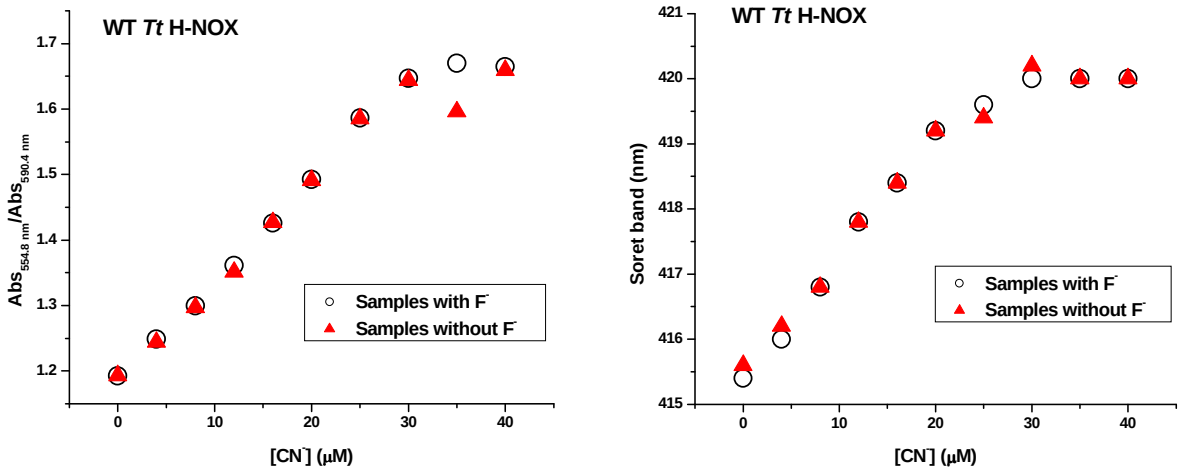

Figure 5-5. β/α band ratio shift and Soret band maximum of WT *Tt* H-NOX (30 μM) upon the addition of cyanide (0-40 μM) with and without the presences of 100 equivalents of fluoride (3 mM).

Next, we examined WT *Tt* H-NOX cyanide quantification in the presence of 100 equivalents of F^- and found that excess F^- does not affect CN^- quantification based on absorbance change measurements (Figure 5-4C and Figure 5-5). We did not observe any interference from fluoride during quantification by the Soret band maximum shift until the amount of F^- was ~1000 times greater than CN^- (Figure 5-5).

Finally, we measured the equilibrium dissociation constants (K_D) for CN^- and F^- binding to WT *Tt* H-NOX (Figure 5-6 and Figure 5-7). As listed in Table 5-1, WT *Tt* H-NOX has a K_D for F^- of 3.45 mM, which is much larger than its K_D for CN^- of 81 nM. This difference explains the high tolerance toward fluoride during cyanide detection.

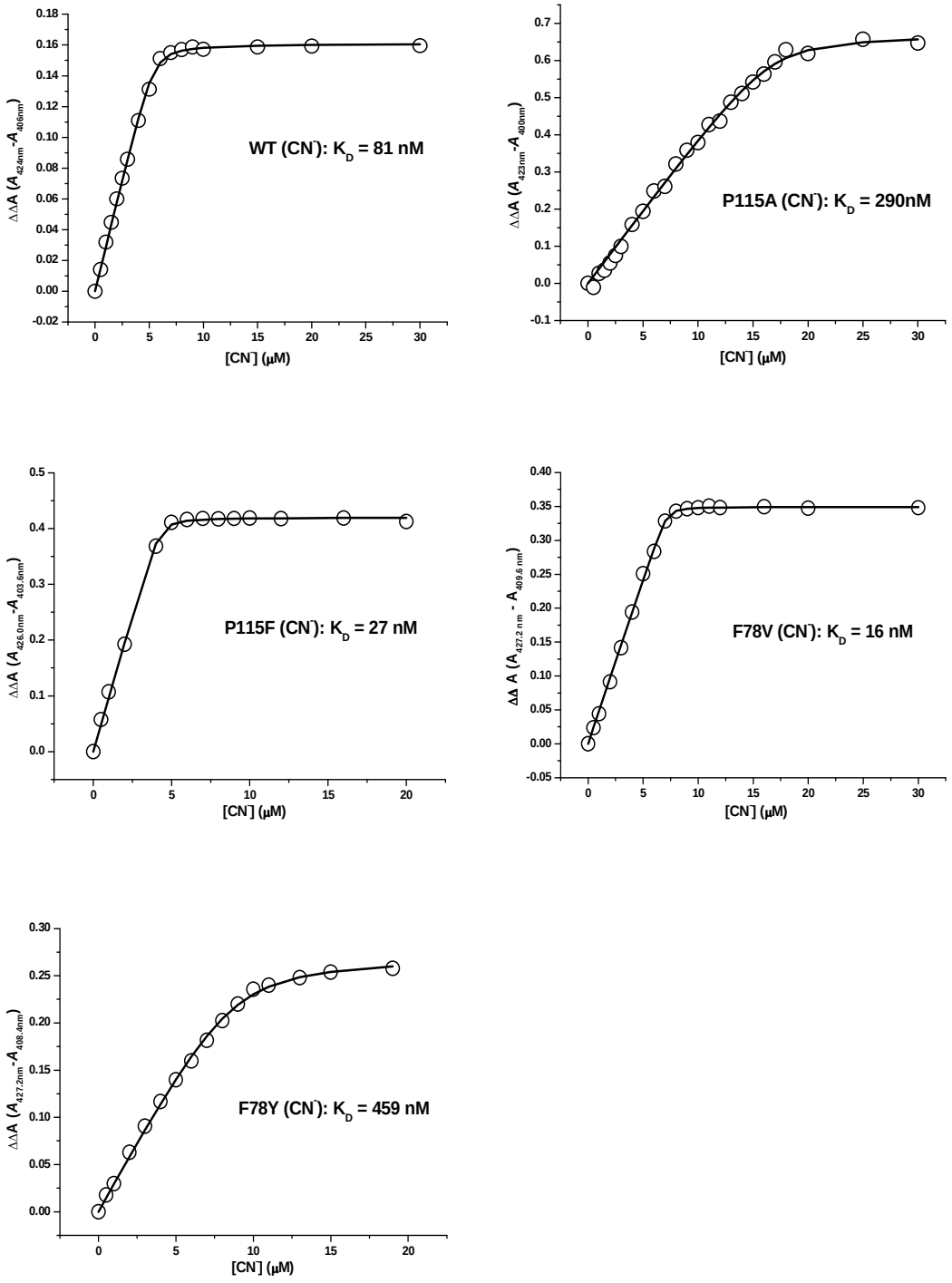

Figure 5-6. Equilibrium dissociation constants for CN^- binding to WT, P115A, P115F, F78V and F78Y *Tt* H-NOX proteins.

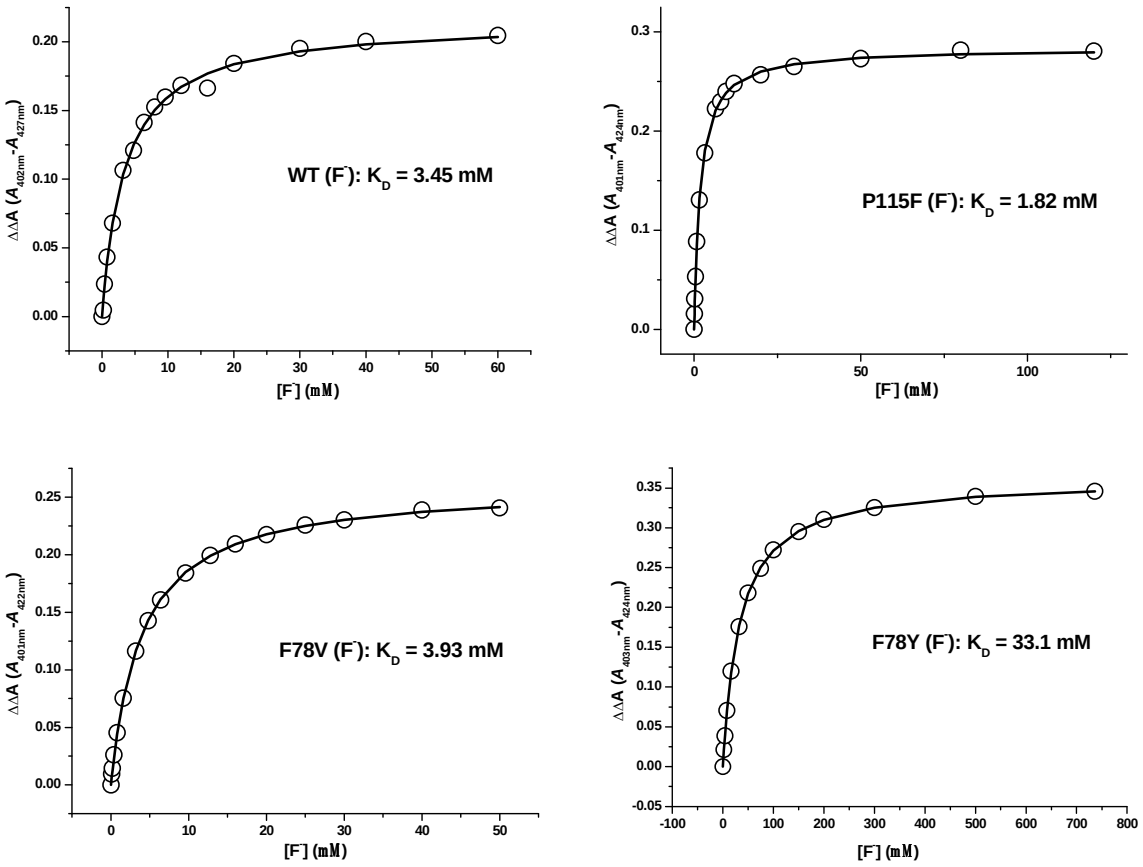

Figure 5-7. Equilibrium dissociation constants for F^- binding to WT, P115F, F78V and F78Y *Tt* H-NOX proteins.

Table 5-1. Ligand binding properties of *Tt* H-NOX proteins.

Sensor	Soret band (nm)		$K_{D\ (CN^-)}$ (M)	$K_{D\ (F^-)}$ (M)	$K_{D\ (CN^-)}$ / $K_{D\ (F^-)}$ × 10^{-6}
	Fe^{3+}-H_2O	Fe^{3+}-CN^-			
WT	415.4	420.6	$(8.1 \pm 2.0) \times 10^{-8}$	$(3.45 \pm 0.17) \times 10^{-3}$	24
P115A	405.0	420.0	$(29.0 \pm 11.1) \times 10^{-8}$	N/A[a]	N/A
P115F	410.1	420.6	$(2.7 \pm 1.3) \times 10^{-8}$	$(1.82 \pm 0.04) \times 10^{-3}$	15
F78V	414.5	420.0	$(1.6 \pm 0.9) \times 10^{-8}$	$(3.93 \pm 0.05) \times 10^{-3}$	4
F78Y	414.6	420.0	$(45.9 \pm 10.5) \times 10^{-8}$	$(33.11 \pm 0.26) \times 10^{-3}$	14

[a] As F^- induces no spectral changes to P115A, its K_D value is not measurable.

The Tt H-NOX P115A mutant is a colorimetric CN^- sensor. A colorimetric sensor would be desirable for cyanide detection. Due to lack of a requirement for sophisticated equipment, such a sensor would be ideal for employment in the field. We did not see a color change in the wildtype sensor upon the addition of cyanide. However, it has been found that changes in the solvent properties can improve the visual detection of cyanide by small molecule sensors;[85] therefore we hypothesized that an alteration at the cyanide sensing site may introduce a color change and render *Tt* H-NOX as a sensor for visual cyanide detection.

Examination of the crystal structure of the Fe^{3+}-OH_2 complex of *Tt* H-NOX[12] reveals that the CN^- binding site in the distal heme pocket is sterically crowded with amino acid side chains. Thus we rationalized that alteration to these residues should affect the "solvent properties" at the cyanide binding site and potentially lead to a better CN^- sensor. Hence, the cyanide sensing properties were investigated for a previously characterized *Tt* H-NOX mutant, P115A.

Proline 115 sits very close to the heme in the proximal heme pocket (Figure 5-1), pushing the porphyrin propionate side chain away and making the heme severely distorted. Based on crystallographic and spectroscopic characterization,[37] the P115A *Tt* H-NOX mutation alters the conformation of the heme, making it less distorted than wildtype and causing a shift in one of the helices in the distal heme pocket. Thus, the heme itself and the distal pocket have different conformations between WT and P115A *Tt* H-NOX. We hypothesized these changes in the environment of the CN^- binding site might alter the CN^- sensing attributes of *Tt* H-NOX.

To test the CN^- sensing properties of P115A *Tt* H-NOX, 20 μM P115A was incubated with 0-60 μM CN^- and the binding reaction was monitored by UV/visible spectroscopy (Figure 5-8). Like WT, the absorbance changes in Soret band region and β/α band region all linearly respond to cyanide concentration, which affords multiple parameters to quantify CN^- in a

variable range dictated by the H-NOX concentration. We noticed that upon CN^- binding, P115A yields a much larger Soret band maximum shift (from 405.0 nm to 420.0 nm) and more dramatic changes in the α/β band region (Figure 5-8), implying that it could be an even better cyanide sensor than the WT *Tt* H-NOX.

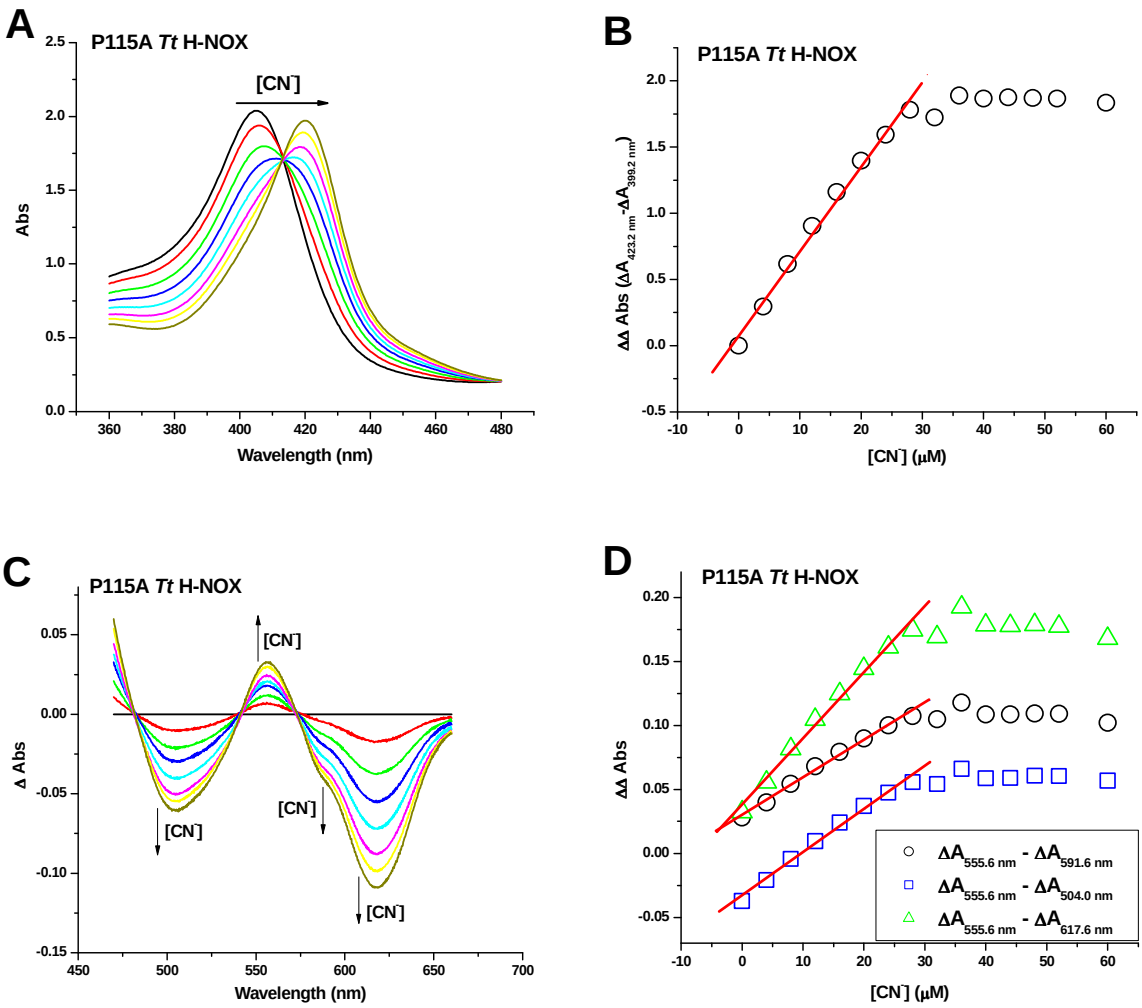

Figure 5-8. Quantification of cyanide using 20 μM P115A *Tt* H-NOX protein. A, C. UV/visible spectral changes at the Soret band region (A) and the β/α band region (C) upon the addition of cyanide. B, D. Cyanide detection based on absorbance changes at the Soret band region (B) and the β/α band region (D). $R^2 = 0.99$.

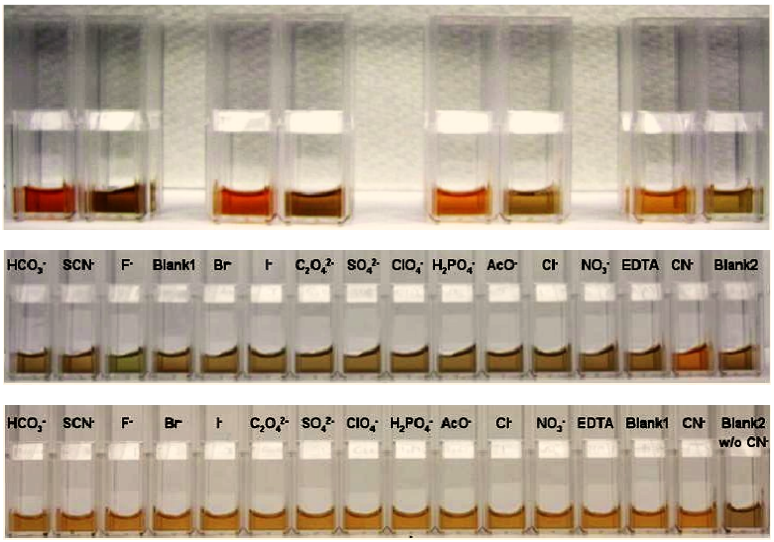

Figure 5-9. Selective visual detection of cyanide using P115A *Tt* H-NOX. Top: color change upon CN^- binding. From left to right: 120 µM, 100 µM, 80 µM and 60 µM P115A*Tt* H-NOX with and without two equivalents of CN^-. Middle: 14 different anions (at 15 mM) were added to 75 µM P115A *Tt* H-NOX. Blank 1 and 2 contain only protein. Bottom: CN^- (150 µM) was added to each sample from above except blank 2. Only cyanide changes the color to orange.

More importantly, we observed a color change from dark brown to bright orange after adding cyanide for 10 minutes (Figure 5-9, Top), which enables us to visually detect cyanide and also confirms our hypothesis that we can improve this cyanide sensing system by modifying the *Tt* H-NOX heme pocket. This color change is possible because P115A H-NOX is dark brown in the Fe^{3+}-OH_2 state, while WT Fe^{3+}-OH_2 and all of the *Tt* H-NOX Fe^{3+}-CN^- complexes are orange in color. This difference in the electronic structure of P115A is likely caused by the flattened heme in the P115A mutant.[37] The structure and some biochemical properties of ferrous complexes of *Tt* H-NOX P115A have been previously reported (although in the ferrous oxidation state, there are no significant differences in the UV/visible spectrum of P115A compared to WT).[12,37] P115A has also been demonstrated to cause a shift in the redox potential of *Tt* H-NOX, compared to WT. This redox potential change may also contribute to the introduction of colorimetric cyanide detection with the P115A mutation.

Furthermore, we found that P115A *Tt* H-NOX has similar CN^- sensitivity and better anion selectivity than WT *Tt* H-NOX. Anion selectivity tests (15 mM) with P115A *Tt* H-NOX (75 µM) revealed that only CN^- changes the UV/visible spectrum (Figure 5-10A) and only CN^- changes the color of P115A *Tt* H-NOX from brown to orange (Figure 5-9, Middle). Even with a large excess of F^- (15 mM), we found no measurable detection of F^- binding based on UV/visible absorption changes. We need to point out that F^- brings about a very slight visually detectable color change, toward green in the absence of CN^-, but this does not affect cyanide detection. After adding cyanide (150 µM) to samples containing various competing anions, we observed spectra typical of the CN^--bound complex (Figure 5-10B) as well as the expected brown-to-orange color change for all samples (Figure 5-9, Bottom). Furthermore, from our studies, a color change is detectable at ~25 µM CN^- (Figure 5-11) with 75 µM P115A *Tt* H-NOX.

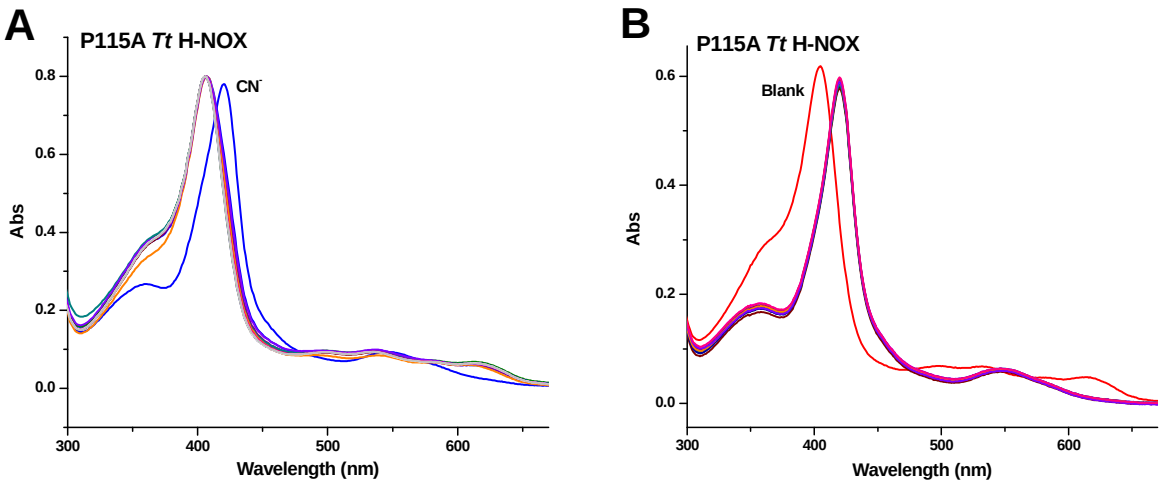

Figure 5-10. A. Spectra of P115A *Tt* H-NOX (75 µM) after the addition of buffer only (blank) and 15 mM SO_4^{2-}, AcO^-, HCO_3^-, F^-, Cl^-, Br^-, I^-, NO_3^-, $C_2O_4^{2-}$, ClO_4^-, SCN^-, phosphate, EDTA or CN^-. Only the cyanide sample (blue curve) yields a spectral shift; Right: spectra of P115A *Tt* H-NOX (75 µM) after adding cyanide (150 µM) to samples in the presence of various existing anions (from above). All samples give typical cyano-complex spectra and only the blank sample (red curve), to which no CN^- was added, yields no spectral change.

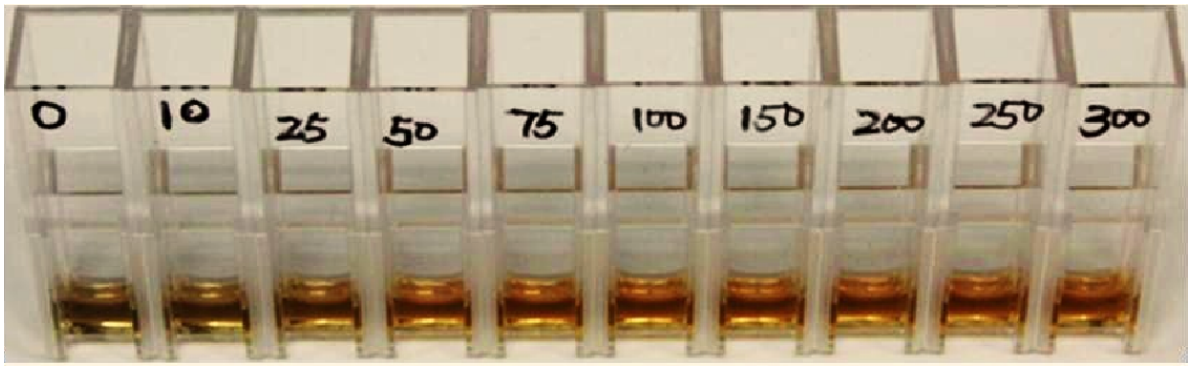

Figure 5-11. Color change of P115A *Tt* H-NOX after adding 0-300 µM cyanide to 75 µM P115A *Tt* H-NOX.

The K_D value of cyanide binding to P115A was determined to be 290 nM (Table 5-1 and Figure 5-6). Although P115A binds CN^- less tightly than WT, the addition of a color change, and lack of F^- binding, make it an attractive construct for cyanide sensing.

Based on our recent X-ray absorption spectroscopy results,[99] during the replacement of water with CN^- at the heme pocket, the central iron in P115A *Tt* H-NOX experiences a much larger shift toward the distal pocket (0.16 Å) than that for WT (0.06 Å). As a result, while the iron in the WT *Tt* H-NOX Fe^{3+}-CN^- complex is located almost exactly at the center of the porphyrin nitrogens, the iron in the P115A *Tt* H-NOX Fe^{3+}-CN^- complex moves dramatically into the distal pocket. This leads to a more crowded ligand binding cavity and hence, larger steric strain in the P115A complex than the WT complex. This change in distortion and protein conformation destabilizes the CN^- and F^- complexes, which explains the larger K_D for Fe^{3+}-CN^- and lack of F^- binding in P115A. These changes lead to enhanced anion selectivity in P115A *Tt* H-NOX.

Cyanide detection properties of Tt H-NOX can be rationally engineered through mutation. Our results with P115A led us to the hypothesis that distal pocket crowding is a key feature for CN^- affinity and specificity using *Tt* H-NOX. In support of our hypothesis, it has

previously been demonstrated that steric hindrance from the distal residues of heme pocket can perturb ligand binding to hemoproteins.[71,102] This hypothesis was tested by the generation of three additional mutants: P115F, F78V, and F78Y.

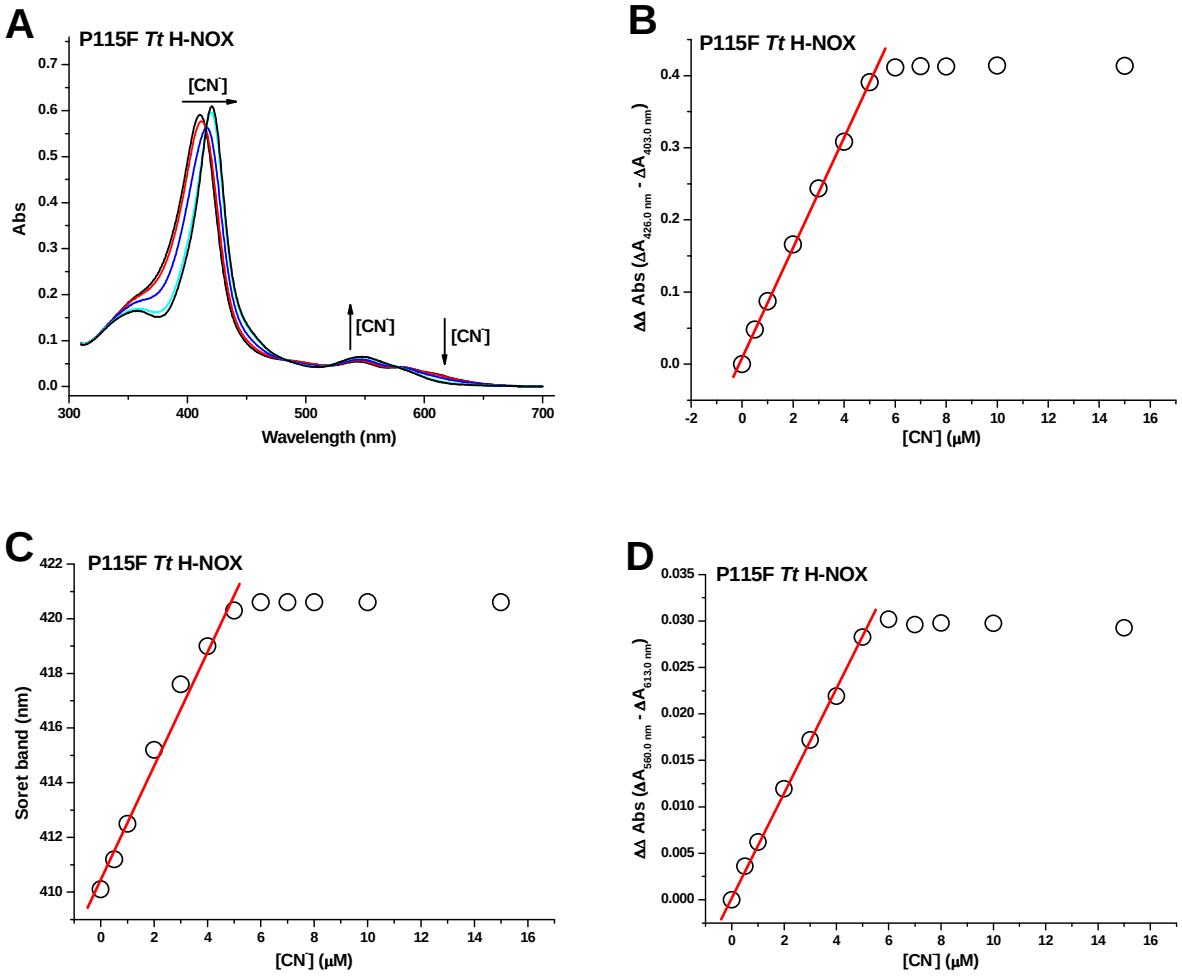

Figure 5-12. Quantification of cyanide using 5 μM P115F *Tt* H-NOX. A. UV/visible spectral shifts upon the addition of cyanide. B, C, D. Cyanide detection based on absorbance changes at the Soret band region (B) and the β/α band region (D), and based on Soret band maximum shift (C). $R^2 = 0.99$.

P115F was chosen to increase the bulk at the P115 position with the aim of altering the heme, and therefore heme pocket structure. Upon addition of cyanide (0-15 μM), the Soret band of P115F (5 μM) moves from 410.1 nm to 420.6 nm (Figure 5-12A). Like WT and P115A, the Soret band maximum and the absorbance changes in both the Soret band and β/α band region linearly titrate with the amount of cyanide added (Figure 5-12). As predicted, P115F has the opposite effect of P115A on CN^- binding. The K_D of P115F for CN^- is 27 nM, making it 3-fold more sensitive to CN^- than WT (Table 5-1 and Figure 5-6). This increase in ligand binding affinity is likely due to a larger binding cavity created by an altered heme conformation as a result of the introduction of bulky phenylalanine. Fluoride also binds more tightly to P115F (K_D = 1.82 mM), however, in comparison to WT, the anion selectivity has been increased through this mutation [$K_D(CN^-)/K_D(F^-)$ is 15×10^{-6} for P115F as compared to 24×10^{-6} for WT; Table 5-1 and Figure 5-6, 5-7].

In order to directly test our hypothesis relating distal pocket crowding to CN^- binding properties, we selected phenylalanine 78 for mutation. F78 is in the distal pocket, packed against the heme, with its benzyl group directed towards the exogenous ligand binding site (Figure 5-1). Therefore we hypothesized that adjusting the size of cyanide binding pocket by changing this residue should affect the cyanide sensing features. Using site-directed mutagenesis, we obtained two mutants, F78V with a less crowded distal pocket, and F78Y with a more crowded distal pocket.

Like all other *Tt* H-NOX constructs, the absorption spectral changes in both the Soret band and β/α band regions titrate with cyanide concentration for both F78V and F78Y (here 0-30 μM CN^- was incubated with 7 μM F78V and 0-20 μM CN^- was incubated with 8 μM F78Y). We can quantify the amount of cyanide present in a sample using the Soret band position, as it shifts

from 414.5 nm to 420.0 nm linearly with increasing CN^-. Thus $[CN^-]$ can be quantified using the Soret band position or change in absorbance (Figure 5-13 and Figure 5-14).

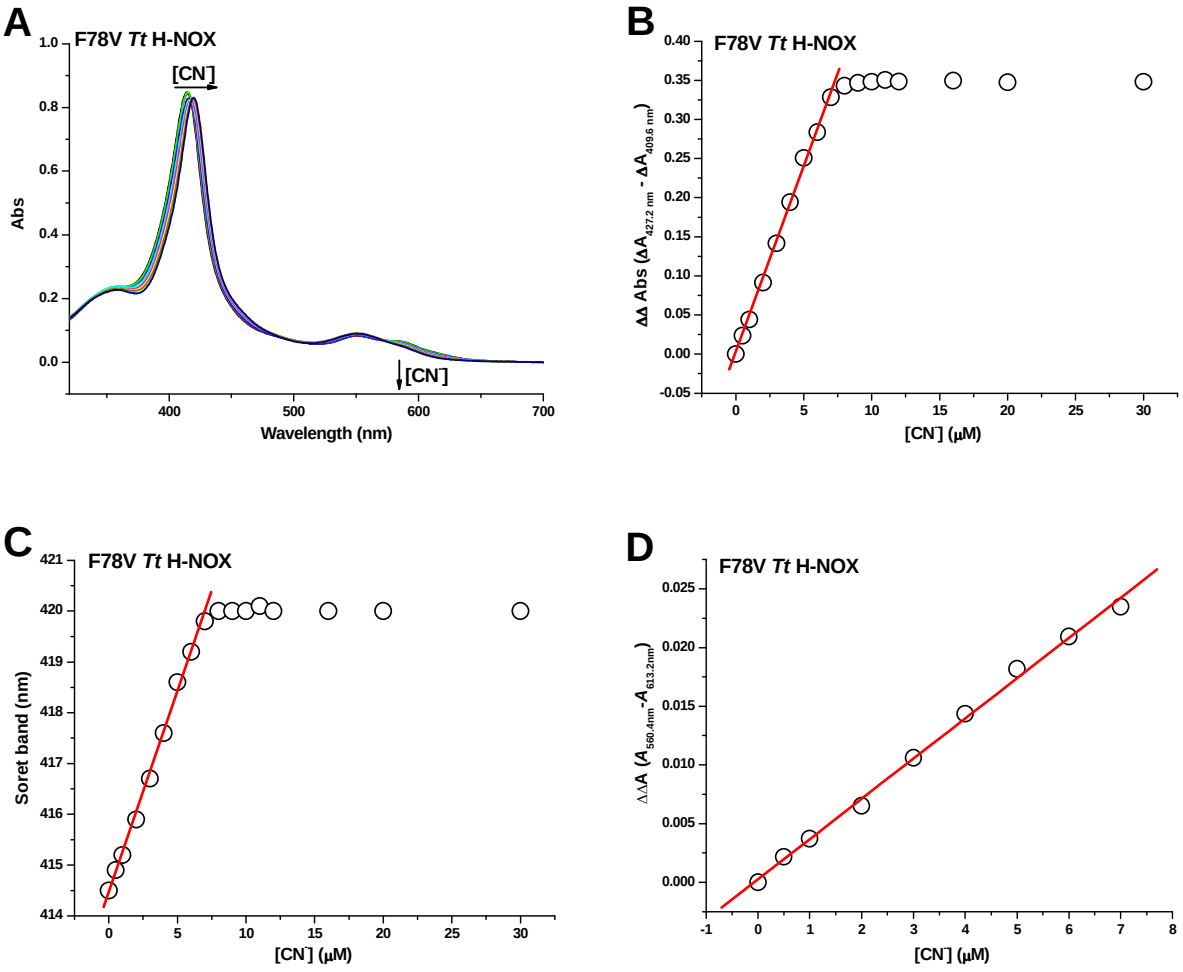

Figure 5-13. Quantification of cyanide using 7 μM F78V *Tt* H-NOX. A. UV/visible spectral changes upon the addition of cyanide. B, C, D. Cyanide detection based on absorbance changes at the Soret band region (B) and the β/α band region (D), and based on Soret band maximum shift (C). $R^2 = 0.99$.

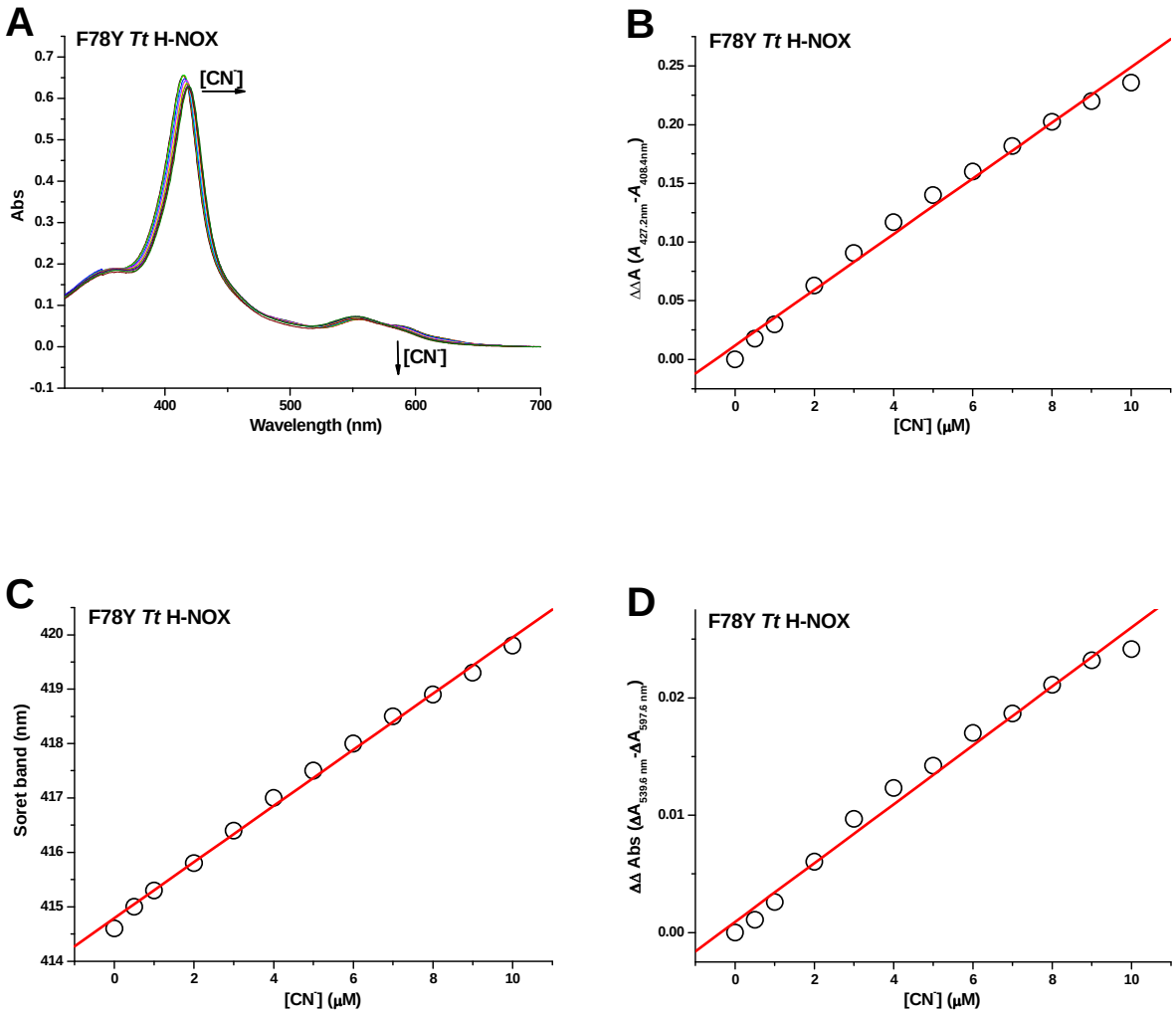

Figure 5-14. Quantification of cyanide using 8 μM F78Y *Tt* H-NOX. A. UV/visible spectral changes upon the addition of cyanide. B, C, D. Cyanide detection based on absorbance changes at the Soret band region (B) and the β/α band region (D), and based on Soret band maximum shift (C). $R^2 = 0.99$.

More importantly, as shown in Table 5-1 and Figure 5-6, the cyanide binding affinity for F78V is increased by ~5 fold compared with WT, which makes this mutant the tightest CN^- receptor among all proteins tested here. Moreover, the F^- affinity is decreased slightly (Figure 5-7), and thus the synergistic effect leads to a large increase in the selectivity of cyanide over fluoride [$K_D(CN^-)/K_D(F^-) = 4 \times 10^{-6}$; Table 5-1] compared to WT. Removal of the F78 benzyl

side chain from the distal pocket likely creates an emptier cyanide binding pocket. The less croweded pocket leads to stabilization of the cyano-complex by providing extra space to help release the steric strain caused by the binding of cyanide and movement of iron towards the distal side.

F78Y, in contrast, interferes with the binding of anions. The affinities for cyanide and fluoride are decreased by ~6 fold and ~10 fold, respectively (Table 5-1 and Figure 5-6, 5-7) in comparison to WT, and the net effect is an increase in anion selectivity in F78Y mutant. F78Y, in addition to increasing steric bulk, also introduces an additional possible hydrogen bond for CN^-. However, apparently the destabilization from steric interference overwhelms the effect of a potentially stabilizing H-bonding, as F78Y has a significantly larger equilibrium dissociation constant for CN^- binding. The CN^- binding affinity changes in F78V and F78Y mutant proteins support our hypothesis linking steric bulk with CN^- affinity. More importantly, the data presented here suggest that *Tt* H-NOX can be further tuned for cyanide sensing.

5.4. Conclusion

Tt H-NOX is a novel cyanide sensing system with high selectivity and excellent sensitivity. With this simple and straightforward cyanide sensing technique, we have achieved a cyanide detection limit as low as 0.5 μM. The linear response to cyanide of multiple probing features, especially the Soret band maximum shift, renders this detection technique unique compared to other cyanide sensing schemes. Furthermore, we have shown that we can improve this system through modifying the heme pocket. We were able to introduce colorimetric detection and enhance anion selectivity in ferric P115A *Tt* H-NOX. Through replacing F78 with

a smaller (valine) or a bigger residue (tyrosine), we tuned the binding affinity of cyanide and improved the anion selectivity. In particular, the F78V protein shows a significant increase in CN^- binding affinity and selectivity. The sensitivity of *Tt* H-NOX to CN^-, in addition to the extreme stability of *Tt* H-NOX, its tolerance of excess anions, and its independent of organic solvents, make it a practical sensor for cyanide monitoring.

Chapter 6. Nitrile as an IR Probe for Electric Field Changes in H-NOX Proteins

Abstract: One critical issue of studying the molecular mechanism of H-NOX signaling is to identify the local electrostatic environment changes at the heme pocket. Nitrile (–CN), as an IR probe, has been found to be a powerful functional group that can be used to monitor changes in the electrostatic environment. In this project, we are exploring the potential of using nitrile to probe the changes in H-NOX electric field during a signaling event. So far, we have successfully introduced the nitrile group into *Tt* H-NOX protein and have detected an IR signal of the –CN group. The IR spectra of –CN modified protein complexes show a nitrile stretch at 2152 cm^{-1}. However, we did not observe a signal shift in the –CN IR absorption when we further introduced the P115A mutation. This is likely because either P115A does not cause a significant change to the electrostatic environment of heme pocket, or Met98 is not an appropriate site for incorporating the nitrile stretch. Further studies include rationally selecting sites for nitrile introduction and/or inducing a larger electrostatic change in H-NOX, so that the –CN probe can sensitively pick up electric field changes in the protein. Once the technique of –CN incorporation into H-NOX is optimized, we will use it to study the heme electric field changes caused by the binding of signaling molecules as well as downstream signal transduction.

6.1. Introduction

One critical issue of studying the molecular mechanism of H-NOX signaling is to identify the local electrostatic environment changes at the heme pocket during a signaling event. A detailed mapping of electric field for the heme group could provide insight into essential signaling features, such as ligand discrimination, heme redox properties, as well as the effects of ligand binding, protein subdomain interactions and protein-protein interactions on heme pocket electrostatics. In previous chapters, we have described using heme iron as an internal XAS probe to obtain insight into H-NOX heme cavity and have generated an overview of electron density flow induced by ligand binding. While XAS study mainly provides information on the heme iron and its coordination spheres, we are exploring techniques that can be more generally applied to different sites of the heme pocket or of the whole H-NOX domain.

A wide variety of spectroscopic probes have been developed to study the local environment in proteins. Nitrile (–CN), as an IR probe, has been found to be a powerful functional group that can be site-specifically introduced into various protein complexes to report on changes in the electrostatic environment.[103-105] The advantages of using nitrile as an probe include: (1) it is small thus it brings about minimal perturbation to the protein matrix; (2) its IR absorption frequency is located at a relatively clean region (ν ~ 2100-2240 cm^{-1}) in the spectrum and the extinction coefficient is relatively large (ε ~ 50-1000 M^{-1} cm^{-1}); (3) the nitrile stretch is sensitive to electric field change; (4) the nitrile group can be easily introduced into proteins through chemical cysteine cyanylation[106,107] (Scheme 6-1) or incorporating nitrile-containing unnatural amino acids (like p-cyano-Phe or m-cyano-Phe) in protein expression.[108] The overall goal of this project is to study the potential of using nitrile as an IR probe to monitor the electrostatic changes in H-NOX at multiple occasions, including signaling molecule ligation,

intra-molecular interactions among subdomains of large H-NOX complex and inter-molecular interactions between H-NOX protein and its cognate enzyme.

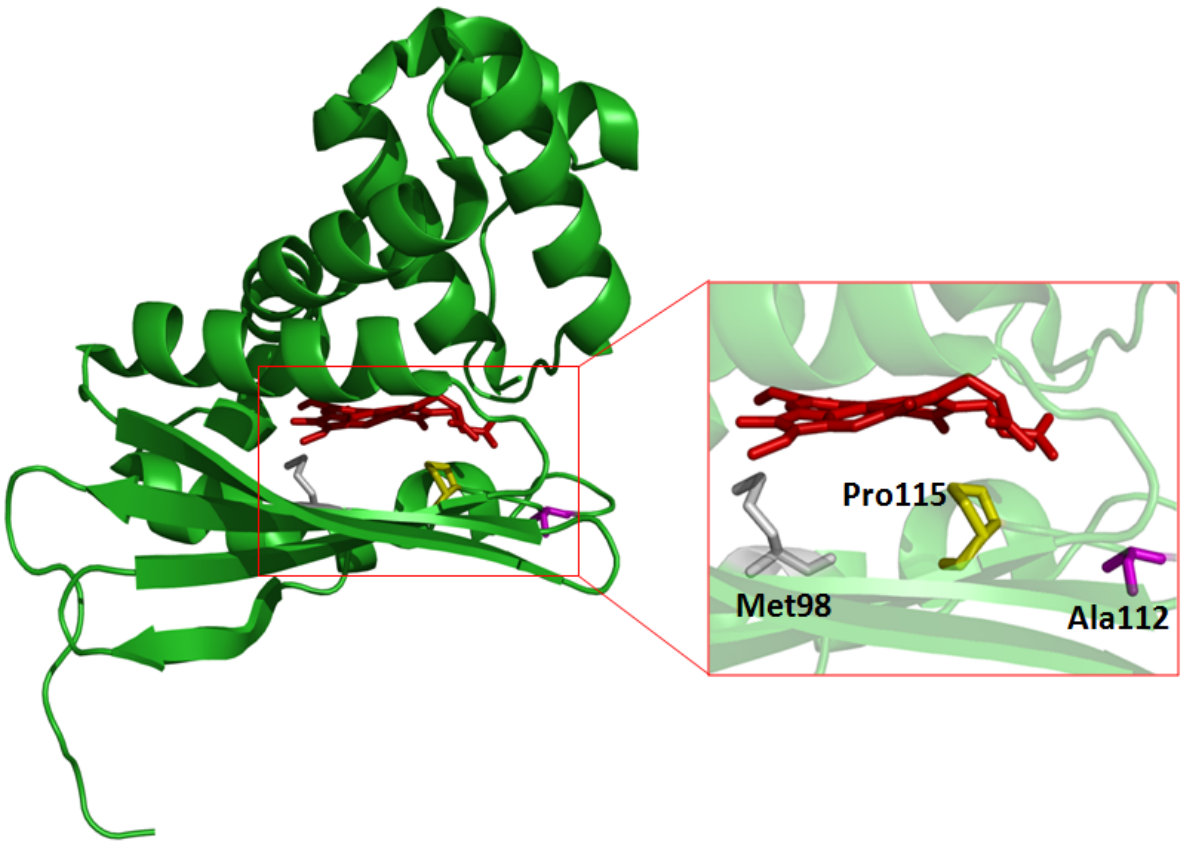

Figure 6-1. Crystal structure of *Tt* H-NOX (adapted from PDB 1U55: Fe(II)-O_2 complex). The heme group is colored in red, while residues Met98, Pro115 and Ala112 are colored in gray, yellow and magenta, respectively.

Proline 115, invariant among H-NOX proteins, has been shown to be primarily responsible for forcing the heme into its strained conformation in *Tt* H-NOX (Figure 6-1).[12,37] The heme significantly flattens upon the P115A mutation. When we first started this project in 2007, we expected that there would be a dramatic change in heme electric field between *Tt* H-NOX WT and P115A. A good understanding of such changes in H-NOX could greatly help to

identify the molecular details of H-NOX signaling. Therefore, we started the project with analyzing the electronic changes caused by P115A mutation in *Tt* H-NOX.

So far, we have successfully introduced the nitrile group into *Tt* H-NOX proteins and have detected an IR signal of the –CN group. As there is no cysteine residue in *Tt* H-NOX, to introduce the nitrile group, we made a site-directed mutation Met98 → Cys (M98C) (Figure 6-1) and then the protein was modified by cysteine cyanylation (Scheme 6-1). The IR spectra of modified protein complexes show a nitrile stretch at 2152 cm^{-1}, demonstrating that this technique can be used for H-NOX complexes. However, we did not observe a signal shift in the –CN IR absorption when we further introduced the P115A mutation. This is likely because P115A does not cause a significant change to the electrostatic environment of heme pocket as evidence by our iron K-edge analysis and recent resonance Raman data.[36,38] It is also possible that Met98 is not an appropriate site for incorporating the nitrile stretch. Further studies include rationally selecting sites for nitrile introduction and/or inducing a larger electrostatic change in H-NOX, so that the –CN probe can sensitively pick up electric field changes in the protein. After we finish the optimization of –CN incorporation into H-NOX, we will use the –CN probe to study the heme electric field changes caused by the binding of signaling molecules as well as downstream signal transduction.

6.2. Materials and Methods

Protein expression and purification. Plasmids for WT and P115A *Tt* H-NOX were generated in previous studies.[36] Site-directed mutagenesis for other *Tt* H-NOX mutants was carried out as described. Mutagenesis for M98C was carried out using primers 5'-

ggctagtgaatttttaatgatgtgcgatgaggtacacctacagcttacc-3’ and its reverse complement. Mutagenesis for A112C was carried out using primers 5’-ccaagatgataaaaggatgcactcctccaaggcttattgcaaagcc-3’ and its reverse complement. Mutagenesis for P115A/M98C double mutant was carried out using M98C primers and *Tt* H-NOX P115A plasmid. Over-expression, purification and storage of all H-NOX proteins were carried out as previously described.

Cysteine cyanylation. After introducing a cysteine residue into *Tt* H-NOX through site-directed mutagenesis, we performed cysteine cyanylation to chemically attach a nitrile group to the thiol side chain of cysteine. The experiment steps are shown in Scheme 6-1. Specifically, *Tt* H-NOX M98C or P115A/M98C was incubated in 25 mM dithiothreitol (DTT) for 1 hour followed by desalting to remove extra DTT. Then 5,5’-dithiobis(2-nitrobenzoic acid) (DTNB or Ellman’s reagent) was added to a final concentration of 16 mM and the reaction solution was kept at room temperature for 2 hours to generate the mixed H-NOX – thionitrobenzoic acid disulfide. Afterwards, KCN was added at 1 M to produce protein-thiocyanate and the reaction solution was again kept at room temperature for 2 hours followed by purification and concentration using concentrator cells (Molecular weight cut off: 10 kD). During the reaction process, 2-nitro-5-thiobenzoate (TNB) anion, as a byproduct, was monitored at 412nm by UV/visible spectroscopy.

Scheme 6-1. Cysteine cyanylation of an H-NOX protein.

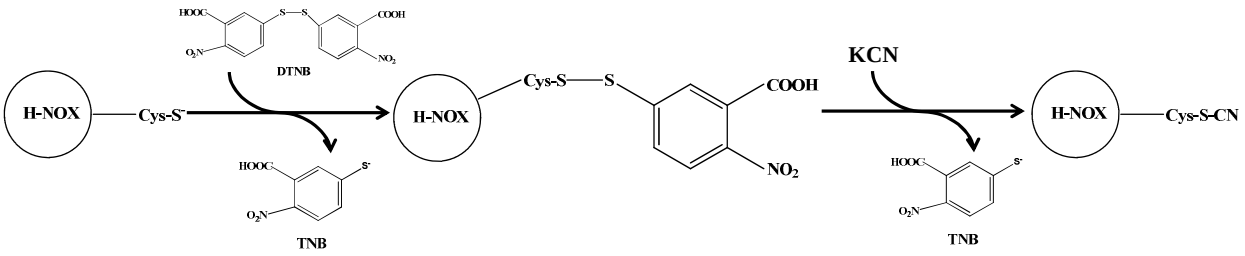

Mass spectroscopy. Unmodified and nitrile-modified *Tt* H-NOX samples were subjected to trypsin/Glu-C double digestion. The experiment was carried out at 37 C° for 20 hours. Afterwards, the ZipTip technique was used to desalt and purify digested peptides before the samples were analyzed by MALDI-MS using a Bruker DALTONICS® autoflex TOF/TOF spectrometer.

UV/visible spectroscopy. All UV/visible spectra were recorded on a Cary 100 Bio spectrophotometer. Preparation of *Tt* H-NOX complexes was carried out as previously published. Measurement of NO dissociation rate were carried out by monitoring the disappearance of Fe(II)-NO Soret band using the Cary 100 Bio spectrophotometer equipped with a constant temperature bath set to 20 °C.

IR spectroscopy. IR samples were prepared in 9 mM sodium phosphate buffer at pH 7.5. The sample concentration of for *Tt* H-NOX M98C-CN was ~0.9 mM, while that for *Tt* H-NOX P115A/M98C-CN was ~2.5 mM. The IR spectrum was taken with a 50 micron spacer and CaF_2 window, with the help of Dr. Lisa Miller from National Synchrotron Light Source (NSLS) at Brookhaven National Laboratory (BNL).

6.3. Results and Discussion

Cysteine cyanylation of Tt H-NOX. One advantage of introducing the nitrile group into *Tt* H-NOX through cysteine cyanylation is the lack of any cysteine residues in this H-NOX protein. This feature creates the opportunity to incorporate the nitrile probe site-specifically. After screening the residues at the heme pocket, we selected Met98 as the mutation site for cysteine

(Figure 6-1). Through site-directed mutagenesis and the reaction processes described in Scheme 6-1, we engineered a single –CN group at *Tt* H-NOX M98C-CN and *Tt* H-NOX P115A/M98C-CN, respectively.

Two different methods were utilized to follow the cysteine modification process: one was to monitor the production of TNB by UV/visible spectroscopy, and the other was to confirm the final cysteine thiocyanate product through Mass spectroscopy. During modification of M98C, the byproduct TNB was detected under UV/visible spectrum, showing a broad band at ~412nm. The absent of an absorption band at 280 nm confirms that the 412 nm absorption originates from TNB, but not the heme protein. Mass spectra of the final products were analyzed to further confirm the nitrile introduction. Unmodified and nitrile-modified *Tt* H-NOX M98C samples were treated with trypsin and Glu-C for digestion, and the samples after digestion were analyzed with MALDI-TOF-MS. We observed an increase in *m/z* of the peptide **RLVNFLMMCDE** from 1371 for unmodified sample (-SH) to 1396 for nitrile-modified sample (-SCN) (Figure 6-2). On the basis of these results, we have successfully modified the Cys98 in *Tt* H-NOX M98C and *Tt* H-NOX P115A/M98C with the nitrile group.

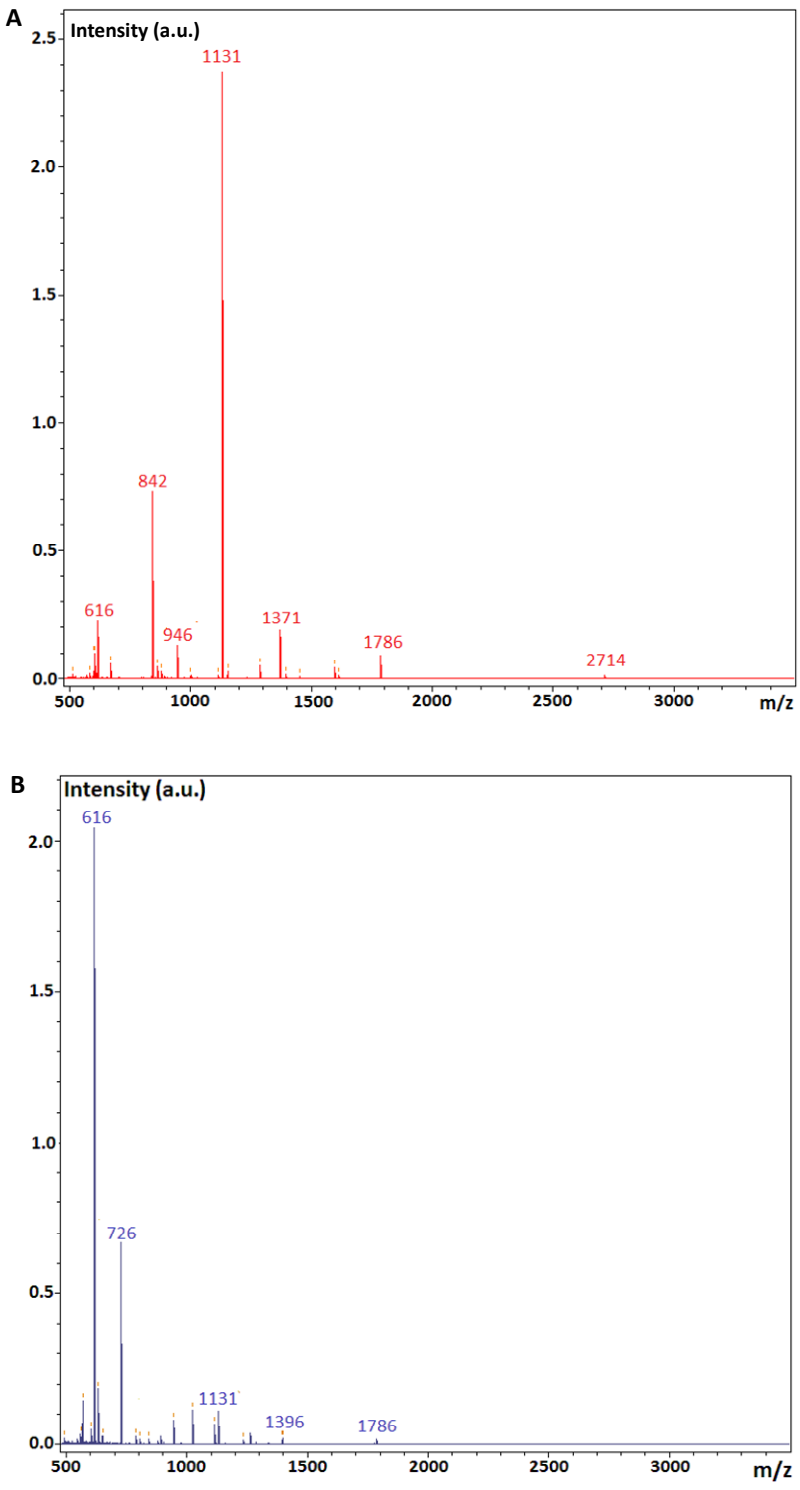

Figure 6-2. MALDI-TOF Mass spectroscopy of unmodified (A) and modified (B) *Tt* H-NOX M98C after trypsin/Glu-C double digestion.

Influence of M98C mutation and cysteine cyanylation on Tt H-NOX. An exogenous probe introduced into a biological system, like the cysteine and nitrile group in our experiment, is expected to cause minimal perturbation to the system by itself. In order to make sure that the modifications do not significantly change heme electric field and conformational state, we performed the UV/visible spectroscopy and ligand binding characterizations of the unmodified and modified *Tt* H-NOX complexes (Table 6-1).

Table 6-1. Characterization of *Tt* H-NOX complexes, including Soret and β/α band absorption maxima and NO dissociation rate constants (unit: nm for Soret and β/α bands, min^{-1} for $k_{off(NO)}$).

Tt H-NOX complex		Soret	β	α	$k_{off(NO)}$
WT	Fe(II)-unligated	431	560		
	Fe(II)-CO	424	545	568	
	Fe(II)-NO	419	547	577	0.042
	Fe(II)-O_2	415	555	591	
P115A	Fe(II)-unligated	431	561		
	Fe(II)-CO	423	544	568	
	Fe(II)-NO	419	547	577	0.026
	Fe(II)-O_2	415	547	583	
A112C	Fe(II)-unligated	432	564		
	Fe(II)-CO	424	544	569	
	Fe(II)-NO	420	543	572	0.030
	Fe(II)-O_2	416	555	590	
M98C	Fe(II)-unligated	434	560		
	Fe(II)-CO	423	541	570	
	Fe(II)-NO	419	544	577	0.025
	Fe(II)-O_2	415	551	587	
M98C-CN	Fe(II)-unligated	434	564		
	Fe(II)-CO	423	543	571	
	Fe(II)-NO	419	545	577	0.024
	Fe(II)-O_2	415	550	587	
P115A/M98C	Fe(II)-unligated	432	562		
	Fe(II)-CO	423	540	569	
	Fe(II)-NO	419	536	569	0.017
	Fe(II)-O_2	414	544	580	

From the UV/visible spectra, the Soret band and β/α band maxima for each ligand state are very similar between wild type and mutants. 5-coordinated Fe(II)-unligated complexes show a typical Soret band at ~431 nm with merged β/α bands at ~ 560 nm. When CO was added, the Soret band undergoes a blue shift to ~424 nm for all proteins. All *Tt* H-NOX proteins form a 6-coordinated Fe(II)-NO complex with a Soret band at ~420 nm, distincting this H-NOX from the H-NOX domains from sGC and facultative aerobes. Upon the binding of oxygen molecules to the *Tt* H-NOX proteins, all of them have a ~415 nm Soret band and the most separated β/α bands. Based on the high similarity in UV/visible spectra among all *Tt* H-NOX proteins, the mutations and cysteine modification do not introduce a significant change to the heme local electric field.

We have also measured the NO dissociation rate constants for all *Tt* H-NOX species to study the effect of modifications on ligand binding kinetics. As shown in Table 6-1, wildtype *Tt* H-NOX has the largest NO dissociate rate at 0.042 min^{-1}, while all single mutations lead to a less than 2-fold decrease in the rate constants. The double mutants P115A/M98C have a NO dissociation rate approximately half of that for WT. Most importantly, the rate constants for unmodified and nitrile-modified *Tt* H-NOX pairs (M98C *v.s.* M98C-CN) are identical, indicating that the incorporation of –CN does not affect the NO binding kinetics. Due to the decrease in rate constant caused by M98C mutation, it is likely that we need to optimize the site selection for cysteine mutation. But on the basis of overall UV/visible spectroscopy and NO dissociation characterizations, there is no dramatic change in heme electrostatics arising from the cysteine mutation and cyanylation.

IR of the nitrile stretch in Tt H-NOX and the influence of proline 115. We successfully detected the nitrile stretch at ~ 2150 cm^{-1} for the modified *Tt* H-NOX complexes (Figure 6-3).

The WT control (which was treated the same way as the M98C experiment) and the M98C control (which has not been treated for cyanylation), show no absorbance between 2100 cm^{-1} and 2240 cm^{-1}; this further confirms that the –CN introduction is specific for cysteine 98 and that unmodified M98C complex does not absorb within that energy range. *Tt* H-NOX M98C-CN complex, with a single –CN group per molecule, shows in its IR spectrum a band at 2152 cm^{-1}, which agrees well with the results of chemically introduced nitrile stretches.

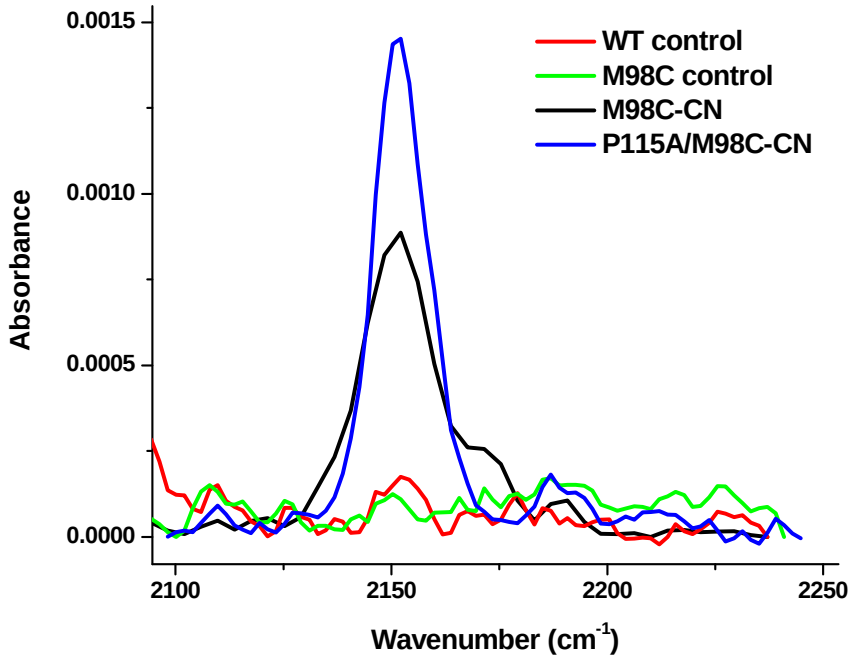

Figure 6-3. IR spectra of unmodified and nitrile-modifiled *Tt* H-NOX proteins.

However, the nitrile stretch in *Tt* H-NOX M98C-CN stays the same upon the P115A mutation and no shift was observed in the IR spectra between *Tt* H-NOX M98C-CN and P115A/M98C-CN complexes (Figure 6-3). This is probably because the overall electric field

change caused by P115A is too weak to be detected by the –CN probe. Based on structural and spectroscopic characterizations, it has been found that the heme group in *Tt* H-NOX is very flexible and can assume several different conformations. Therefore, it is likely that even though P115A mutation largely relaxes the heme, it leads to a relatively minor perturbation to the heme group electronics, especially if we consider the dynamic feature of this domain. The XAS results also support this idea that the K-edge values are very similar for the same ligand binding states of WT and P115A *Tt* H-NOX. Another possible reason for the insensitivity of nitrile stretch to P115A mutation is that the electrostatic changes caused by P115A mutation cannot be sensed by the –CN group at site Cys98. From this point of view, Met 98 may be not a suitable site for introducing the –CN group as an IR probe.

Preliminary studies on Tt H-NOX A112C and future plans. As the nitrile stretch in *Tt* H-NOX M98C-CN failed to pick up the electric field change induced by P115A mutation, we went further to screen for positions that are appropriate for –CN introduction. Alanine 112 was chosen to be mutated to cysteine for cyanylation. As seen in the crystal structure, the side chain of Ala112 locates neither too close to the heme cofactor so that the modifications should have minimal perturbation on the heme group, nor too far away so that –CN will be unable to detect environmental changes at the heme pocket (Figure 6-1).

Preliminary characterizations of *Tt* H-NOX A112C were performed to examine its UV/Visible absorption and ligand binding properties. As shown in Table 6-1, the Soret bands and β/α bands for various A112C complexes are very similar with the ones for WT, indicating a minimal effect of this mutation on the electronic spectra of *Tt* H-NOX. Furthermore, we determined the NO dissociation rate constant for *Tt* H-NOX A112C (0.030 min^{-1}), which is the

closest to that for WT (0.042 min^{-1}) among all mutants. Therefore, the A112C mutation does not introduce significant changes to the heme pocket.

Future work on the A112C mutant will be the same as that has been done to M98C: (1) incorporate the nitrile group to the cysteine side chain; (2) confirm the correct –CN group incorporation and make sure the modification does not cause a large variation in *Tt* H-NOX properties; (3) measure the nitrile stretch with IR spectroscopy and use it to probe electric field changes in *Tt* H-NOX caused by key residue mutation or ligand binding.

To further explore the application of –CN group as an IR probe for electric field changes in *Tt* H-NOX, other sites of the heme pocket will be considered for cysteine mutation and cyanylation. To guide and optimize the site selection for –CN introduction, we will also study the electron density mapping of the H-NOX heme pocket. Once we complete the optimization of –CN incorporation, we will use the –CN probe to study the heme electric field change in an H-NOX signaling event.

6.4. Conclusion

With *Tt* H-NOX as the model system, we have explored the application of nitrile as an IR probe to monitor the local electric field of the H-NOX heme pocket. To introduce the nitrile group, we made the M98C mutation and the mutants were modified through cysteine cyanylation. The IR spectra of modified protein complexes show a nitrile stretch at 2152 cm^{-1}, demonstrating that this technique can be used for H-NOX complexes. Unfortunately, we did not observe a change in the –CN IR absorption when we further introduced the P115A mutation. The reason is possibly that either P115A does not cause a significant change to the electrostatic

environment of heme pocket, or Met98 is not an appropriate site for incorporating the nitrile stretch. Further studies include rationally selecting sites for nitrile as well as inducing a larger heme electrostatic change, so that the –CN probe can sensitively pick up electric field changes in the protein during a signaling events. We have started the work at a new site Ala112 and preliminary characterizations indicate that the A112C mutation does not cause a dramatic change in heme. It is expected that, once we complete the optimization of –CN incorporation to H-NOX, we could use the –CN probe to study the heme electric field changes when H-NOX signaling events take place.

Bibliography

(1) Ignarro, L. J. *Biochem. Pharmacol.* **1991**, *41*, 485.

(2) Gong, W.; Hao, B.; Chan, M. K. *Biochemistry* **2000**, *39*, 3955.

(3) Gong, W.; Hao, B.; Mansy, S. S.; Gonzalez, G.; Gilles-Gonzalez, M. A.; Chan, M. K. *Proc. Natl. Acad. Sci. U.S.A.* **1998**, *95*, 15177.

(4) Hao, B.; Isaza, C.; Arndt, J.; Soltis, M.; Chan, M. K. *Biochemistry* **2002**, *41*, 12952.

(5) Komori, H.; Inagaki, S.; Yoshioka, S.; Aono, S.; Higuchi, Y. *J. Mol. Biol.* **2007**, *367*, 864.

(6) Lanzilotta, W. N.; Schuller, D. J.; Thorsteinsson, M. V.; Kerby, R. L.; Roberts, G. P.; Poulos, T. L. *Nat. Struct. Biol.* **2000**, *7*, 876.

(7) Zhang, W.; Phillips, G. N. *Structure (London)* **2003**, *11*, 1097.

(8) Schmidt, H.; Walter, U. *Cell* **1994**, *78*, 919.

(9) Chan, M. K. *Curr. Opin. Chem. Biol.* **2001**, *5*, 216.

(10) Rodgers, K. R. *Curr. Opin. Chem. Biol.* **1999**, *3*, 158.

(11) Evgenov, O. V.; Pacher, P.; Schmidt, P. M.; Hasko, G.; Schmidt, H. H. H. W.; Stasch, J.-P. *Nat. Rev. Drug Discov.* **2006**, *5*, 755.

(12) Pellicena, P.; Karow, D. S.; Boon, E. M.; Marletta, M. A.; Kuriyan, J. *Proc. Natl. Acad. Sci. U.S.A.* **2004**, *101*, 12854.

(13) Nioche, P.; Berka, V.; Vipond, J.; Minton, N.; Tsai, A.-L.; Raman, C. S. *Science* **2004**, *306*, 1550.

(14) Waldman, S. A.; Murad, F. *Pharmacol. Rev.* **1987**, *39*, 163.

(15) Cary, S. P. L.; Winger, J. A.; Derbyshire, E. R.; Marletta, M. A. *Trends Biochem. Sci.* **2006**, *31*, 231.

(16) Zhao, Y.; Marletta, M. A. *Biochemistry* **1997**, *36*, 15959.

(17) Karow, D. S.; Pan, D.; Davis, J. H.; Behrends, S.; Mathies, R. A.; Marletta, M. A. *Biochemistry* **2005**, *44*, 16266.

(18) Boon, E. M.; Marletta, M. A. *J. Inorg. Biochem.* **2005**, *99*, 892.

(19) Derbyshire, E. R.; Winter, M. B.; Ibrahim, M.; Deng, S.; Spiro, T. G.; Marletta, M. A. *Biochemistry* **2011**, *50*, 4281.

(20) Iyer, L.; Anantharaman, V.; Aravind, L. *BMC Genomics* **2003**, *4*, 5.

(21) Karow, D. S.; Pan, D.; Tran, R.; Pellicena, P.; Presley, A.; Mathies, R. A.; Marletta, M. A. *Biochemistry* **2004**, *43*, 10203.

(22) Ma, X.; Sayed, N.; Beuve, A.; van den Akker, F. *EMBO J.* **2007**, *26*, 578.

(23) Erbil, W. K.; Price, M. S.; Wemmer, D. E.; Marletta, M. A. *Proc. Natl. Acad. Sci. U.S.A.* **2009**, *106*, 19753.

(24) Wang, Y.; Dufour, Y. S.; Carlson, H. K.; Donohue, T. J.; Marletta, M. A.; Ruby, E. G. *Proc. Natl. Acad. Sci. U.S.A.* **2010**, *107*, 8375.

(25) Carlson, H. K.; Vance, R. E.; Marletta, M. A. *Mol. Microbiol.* **2010**, *77*, 930.

(26) Price, M. S.; Chao, L. Y.; Marletta, M. A. *Biochemistry* **2007**, *46*, 13677.

(27) Gray, J. M.; Karow, D. S.; Lu, H.; Chang, A. J.; Chang, J. S.; Ellis, R. E.; Marletta, M. A.; Bargmann, C. I. *Nature* **2004**, *430*, 317.

(28) Boon, E. M.; Huang, S. H.; Marletta, M. A. *Nat. Chem. Biol.* **2005**, *1*, 53.

(29) Boon, E. M.; Marletta, M. A. *Curr. Opin. Chem. Biol.* **2005**, *9*, 441.

(30) Capece, L.; Estrin, D. A.; Marti, M. A. *Biochemistry* **2008**, *47*, 9416.

(31) Weinert, E. E.; Plate, L.; Whited, C. A.; Olea, C.; Marletta, M. A. *Angew. Chem. Int. Ed* **2010**, *49*, 720.

(32) Schmidt, P. M.; Schramm, M.; Schröder, H.; Wunder, F.; Stasch, J.-P. *J. Biol. Chem.* **2004**, *279*, 3025.

(33) Denninger, J. W.; Marletta, M. A. *Biochim. Biophys. Acta* **1999**, *1411*, 334.

(34) Jentzen, W.; Ma, J.-G.; Shelnutt, J. A. *Biophys. J.* **1998**, *74*, 753.

(35) Dai, Z.; Boon, E. M. *J. Am. Chem. Soc.* **2010**, *132*, 11496.

(36) Dai, Z.; Boon, E. M. *J. Inorg. Biochem.* **2011**, *105*, 784.

(37) Olea, C.; Boon, E. M.; Pellicena, P.; Kuriyan, J.; Marletta, M. A. *ACS Chem. Biol.* **2008**, *3*, 703.

(38) Tran, R.; Boon, E. M.; Marletta, M. A.; Mathies, R. A. *Biochemistry* **2009**.

(39) Olea, C.; Kuriyan, J.; Marletta, M. A. *J. Am. Chem. Soc.* **2010**, *132*, 12794.

(40) Ibrahim, M.; Derbyshire, E. R.; Marletta, M. A.; Spiro, T. G. *Biochemistry* **2010**, *49*, 3815.

(41) Zhao, Y.; Brandish, P. E.; Ballou, D. P.; Marletta, M. A. *Proc. Natl. Acad. Sci. U.S.A.* **1999**, *96*, 14753.

(42) Martin, E.; Berka, V.; Bogatenkova, E.; Murad, F.; Tsai, A.-L. *J. Biol. Chem.* **2006**, *281*, 27836.

(43) Namiki, S.; Hirose, K.; Iino, M. *Biochem. Biophys. Res. Commun.* **2001**, *288*, 798.

(44) Boon, E. M.; Davis, J. H.; Tran, R.; Karow, D. S.; Huang, S. H.; Pan, D.; Miazgowicz, M. M.; Mathies, R. A.; Marletta, M. A. *J. Biol. Chem.* **2006**, *281*, 21892.

(45) Barrick, D. *Biochemistry* **2002**, *33*, 6546.

(46) Bianconi, A.; Congiu-Castellano, A.; Dell'Ariccia, M.; Giovannelli, A.; Durham, P. J.; Burattini, E.; Barteri, M. *FEBS Lett.* **1984**, *178*, 165.

(47) Chance, B.; Powers, L.; Ching, Y.; Poulos, T.; Schonbaum, G. R.; Yamazaki, I.; Paul, K. G. *Arch. Biochem. Biophys.* **1984**, *235*, 596.

(48) D'Angelo, P.; Lapi, A.; Migliorati, V.; Arcovito, A.; Benfatto, M.; Roscioni, O. M.; Meyer-Klaucke, W.; Della-Longa, S. *Inorg. Chem.* **2008**, *47*, 9905.

(49) Levina, A.; Armstrong, R. S.; Lay, P. A. *Coord. Chem. Rev.* **2005**, *249*, 141.

(50) Chance, M.; Parkhurst, L.; Powers, L.; Chance, B. *J. Biol. Chem.* **1986**, *261*, 5689.

(51) Miller, L. M.; Chance, M. R. *Biochemistry* **2002**, *34*, 10170.

(52) Roe, A. L.; Schneider, D. J.; Mayer, R. J.; Pyrz, J. W.; Widom, J.; Que, L. *J. Am. Chem. Soc.* **1984**, *106*, 1676.

(53) Westre, T. E.; Kennepohl, P.; DeWitt, J. G.; Hedman, B.; Hodgson, K. O.; Solomon, E. I. *J. Am. Chem. Soc.* **1997**, *119*, 6297.

(54) Wirt, M. D.; Sagi, I.; Chen, E.; Frisbie, S. M.; Lee, R.; Chance, M. R. *J. Am. Chem. Soc.* **1991**, *113*, 5299.

(55) Benfatto, M.; Della Longa, S.; Natoli, C. R. *J. Synchrotron Rad.* **2003**, *10*, 51.

(56) Della Longa, S.; Pin, S.; Cortes, R.; Soldatov, A. V.; Alpert, B. *Biophys. J.* **1998**, *75*, 3154.

(57) Hopfield, J. J. *J. Mol. Biol.* **1973**, *77*, 207.

(58) Barraud, N.; Schleheck, D.; Klebensberger, J.; Webb, J. S.; Hassett, D. J.; Rice, S. A.; Kjelleberg, S. *J. Bacteriol.* **2009**, *191*, 7333.

(59) Kassner, R. J. *Proc. Natl. Acad. Sci. U.S.A.* **1972**, *69*, 2263.

(60) Kennedy, M. L.; Silchenko, S.; Houndonougbo, N. v.; Gibney, B. R.; Dutton, P. L.; Rodgers, K. R.; Benson, D. R. *J. Am. Chem. Soc.* **2001**, *123*, 4635.

(61) Mao, J.; Hauser, K.; Gunner, M. R. *Biochemistry* **2003**, *42*, 9829.

(62) Mauk, A. G.; Moore, G. R. *J. Biol. Inorg. Chem.* **1997**, *2*, 119.

(63) Grinstaff, M.; Hill, M.; Labinger, J.; Gray, H. *Science* **1994**, *264*, 1311.

(64) Cowley, A. B.; Kennedy, M. L.; Silchenko, S.; Lukat-Rodgers, G. S.; Rodgers, K. R.; Benson, D. R. *Inorg. Chem.* **2006**, *45*, 9985.

(65) Tezcan, F. A.; Winkler, J. R.; Gray, H. B. *J. Am. Chem. Soc.* **1998**, *120*, 13383.

(66) Perutz, M. F. *Nature* **1970**, *228*, 726.

(67) Marti, M. A.; Capece, L.; Crespo, A.; Doctorovich, F.; Estrin, D. A. *J. Am. Chem. Soc.* **2005**, *127*, 7721.

(68) Martí, M. A.; Scherlis, D. A.; Doctorovich, F. A.; Ordejón, P.; Estrin, D. A. *J. Biol. Inorg. Chem.* **2003**, *8*, 595.

(69) Kruglik, S. G.; Yoo, B.-K.; Franzen, S.; Vos, M. H.; Martin, J.-L.; Negrerie, M. *Proc. Natl. Acad. Sci. U.S.A.* **2010**, *107*, 13678.

(70) Friebe, A.; Koesling, D. *Mol. Pharmacol.* **1998**, *53*, 123.

(71) Rodriguez-Lopez, J. N.; Smith, A. T.; Thorneley, R. N. F. *J. Biol. Chem.* **1997**, *272*, 389.

(72) Varadarajan, R.; Zewert, T. E.; Gray, H. B.; Boxer, S. G. *Science* **1989**, *243*, 69.

(73) Rivera, M.; Seetharaman, R.; Girdhar, D.; Wirtz, M.; Zhang, X. J.; Wang, X. Q.; White, S. *Biochemistry* **1998**, *37*, 1485.

(74) Gunner, M. R.; Honig, B. *Proc Natl Acad Sci U S A* **1991**, *88*, 9151.

(75) Bertrand, P.; Mbarki, O.; Asso, M.; Blanchard, L.; Guerlesquin, F.; Tegoni, M. *Biochemistry* **1995**, *34*, 11071.

(76) Kennedy, M. L.; Gibney, B. R. *Curr Opin Struct Biol* **2001**, *11*, 485.

(77) Vennesland, B. C., E. E., Knownles, C. J., Westly, J., Wissing, F. *Cyanide in Biology*; Academic Press: London, 1981.

(78) Koenig, R. *Science* **2000**, *287*, 1737.

(79) *Guidelines for Drinking-Water Quality*; World Health Organization: Geneva, 1996.

(80) Weinberg, H. S.; Cook, S. J. *Anal. Chem.* **2002**, *74*, 6055.

(81) Badugu, R.; Lakowicz, J. R.; Geddes, C. D. *J. Am. Chem. Soc.* **2005**, *127*, 3635.

(82) Hudnall, T. W.; Gabbaï, F. P. *J. Am. Chem. Soc.* **2007**, *129*, 11978.

(83) Kim, Y.; Zhao, H.; Gabbaï, François P. *Angew. Chem. Int. Ed.* **2009**, *48*, 4957.

(84) Männel-Croisé, C.; Zelder, F. *Inorg. Chem.* **2009**, *48*, 1272.

(85) Zelder, F. H. *Inorg. Chem.* **2008**, *47*, 1264.

(86) Cho, D.-G.; Kim, J. H.; Sessler, J. L. *J. Am. Chem. Soc.* **2008**, *130*, 12163.

(87) Lee, K.-S.; Kim, H.-J.; Kim, G.-H.; Shin, I.; Hong, J.-I. *Org. Lett.* **2007**, *10*, 49.

(88) Yang, Y.-K.; Tae, J. *Org. Lett.* **2006**, *8*, 5721.

(89) Tomasulo, M.; Raymo, F. M. *Org. Lett.* **2005**, *7*, 4633.

(90) Tomasulo, M.; Sortino, S.; White, A. J. P.; Raymo, F. M. *J. Org. Chem.* **2005**, *71*, 744.

(91) Chow, C.-F.; Lam, M. H. W.; Wong, W.-Y. *Inorg. Chem.* **2004**, *43*, 8387.

(92) Gettler, A. O.; Goldbaum, L. *Anal. Chem.* **2002**, *19*, 270.

(93) Guilbault, G. G.; Kramer, D. N. *Anal. Chem.* **2002**, *37*, 1395.

(94) Mottola, H. A.; Freiser, H. *Anal. Chem.* **2002**, *40*, 1266.

(95) Peng, L.; Wang, M.; Zhang, G.; Zhang, D.; Zhu, D. *Org. Lett.* **2009**, *11*, 1943.

(96) Poland, K.; Topoglidis, E.; Durrant, J. R.; Palomares, E. *Inorg. Chem. Commun.* **2006**, *9*, 1239.

(97) Shan, D.; Mousty, C.; Cosnier, S. *Anal. Chem.* **2004**, *76*, 178.

(98) Smit, M. H.; Cass, A. E. G. *Anal. Chem.* **1990**, *62*, 2429.

(99) Dai, Z.; Boon, E. M. *J. Inorg. Biochem.* **2010**, *In preparation*.

(100) Boon, E. M.; Marletta, M. A. *J. Am. Chem. Soc.* **2006**, *128*, 10022.

(101) Bidwai, A.; Witt, M.; Foshay, M.; Vitello, L. B.; Satterlee, J. D.; Erman, J. E. *Biochemistry* **2003**, *42*, 10764.

(102) Balasubramanian, S.; Lambright, D. G.; Boxer, S. G. *Proc. Natl. Acad. Sci. U.S.A.* **1993**, *90*, 4718.

(103) Fafarman, A. T.; Webb, L. J.; Chuang, J. I.; Boxer, S. G. *J. Am. Chem. Soc.* **2006**, *128*, 13356.

(104) Fafarman, A. T.; Boxer, S. G. *J. Phys. Chem. B* **2010**, *114*, 13536.

(105) Webb, L. J.; Boxer, S. G. *Biochemistry* **2008**, *47*, 1588.

(106) Patchornik, A.; Degani, Y.; Neumann, H. *J. Am. Chem. Soc.* **1970**, *92*, 6969.

(107) Vanaman, T. C.; Stark, G. R. *J. Biol. Chem.* **1970**, *245*, 3565.

(108) Ryu, Y.; Schultz, P. G. *Nat. Methods* **2006**, *3*, 263.

Appendix. Plasmid, Primers and UV/visible spectra for *Tt* H-NOX proteins

pET-20b(+) vector

Tt H-NOX was cloned into pET-20b(+) vector (Novagen) between restriction sites Xho I and Nde I with the 5' starting at Nde I (Figure A1 and A2, adapted from the pET-20b(+) vector map from Novagen).

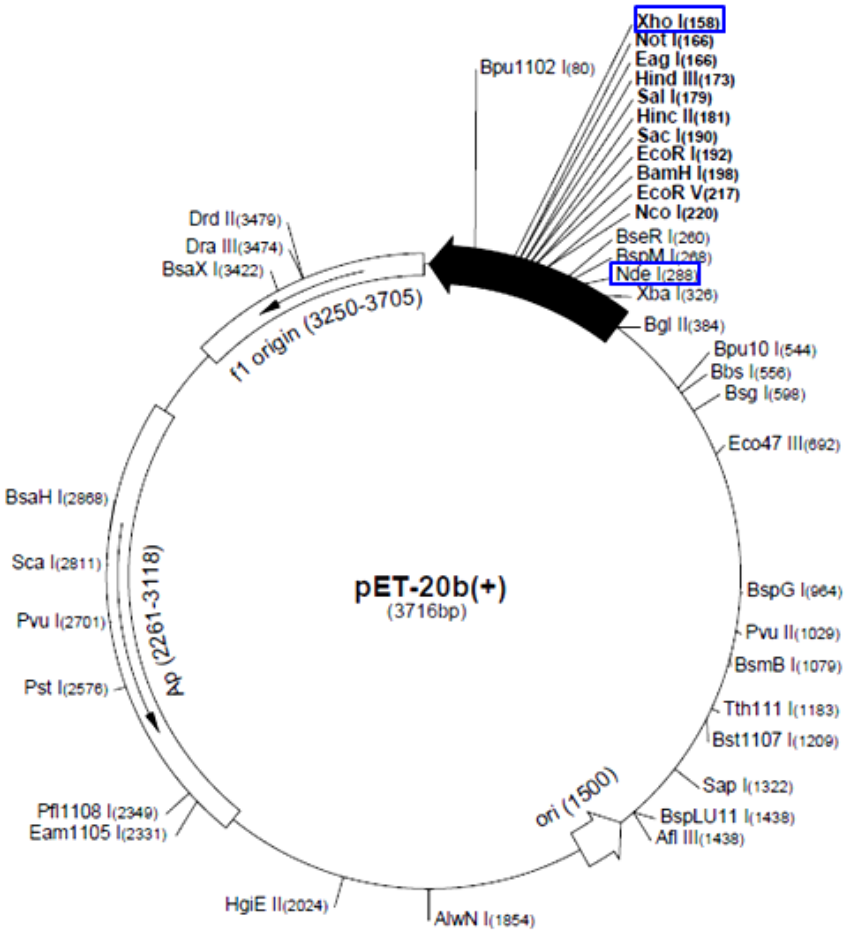

Figure A1. Circle map of vector pET-20b(+).

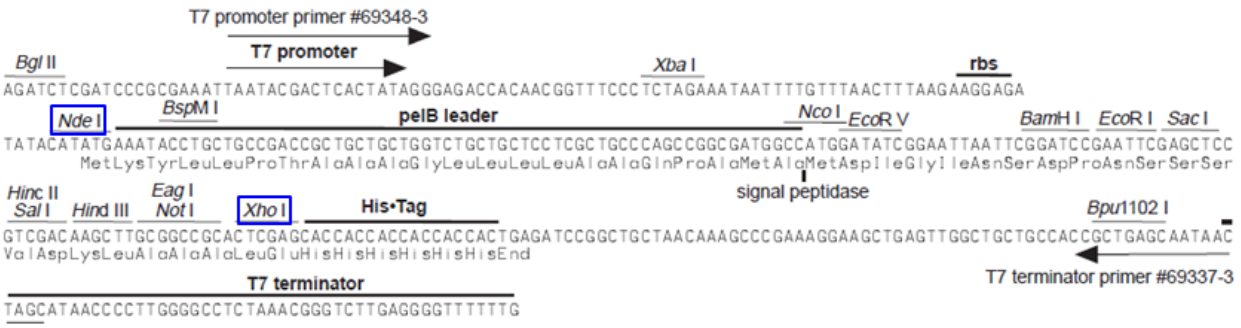

Figure A2. The cloning/expression region of the coding strand transcribed by T7 RNA polymerase in pET-20b(+) vector.

Tt H-NOX DNA and amino acid sequences

Tt H-NOX is located at the N-terminal of a methyl-accepting chemotaxis protein (MCP). *Tt* H-NOX domain includes 188 amino acids with no cysteine residue (Figure A3). The gene sequence of the MCP is shown in Figure A4 and *Tt* H-NOX gene is the part colored in red. The MCP protein is coded with TTE0680 in the NCBI data base and it consists of 1809 base pairs (from 683006 to 684814 in the *T. tengcongensis* genome). The gene sequence for *Tt* H-NOX includes the first 564 base pairs.

1 MKGTIVGTWI KTLRDLYGND VVDESLKSVG WEPDRVITPL EDIDDDEVRR IFAKVSEKTG
61 KNVNEIWREV GRQNIKTFSE WFPSYFAGRR LVNFLMMMDE VHLQLTKMIK GATPPRLIAK
121 PVAKDAIEME YVSKRKMYDY FLGLIEGSSK FFKEEISVEE VERGEKDGFS RLKVRIKFKN
181 PVFEYKKN

Figure A3. Amino acid sequence of *Tt* H-NOX.

1 ATGAAGGGGA CAATCGTCGG GACATGGATA AAGACCCTGA GGGACCTTTA CGGGAATGAT
61 GTGGTTGATG AATCTTTAAA AAGTGTGGGT TGGGAACCAG ATAGGGTAAT TACACCTCTG
121 GAGGATATTG ATGACGATGA GGTTAGGAGA ATTTTTGCTA AGGTGAGTGA AAAAACTGGT
181 AAAAATGTCA ACGAAATATG GAGAGAGGTA GGAAGGCAGA ACATAAAAAC TTTCAGCGAA
241 TGGTTTCCCT CCTATTTTGC AGGGAGAAGG CTAGTGAATT TTTTAATGAT GATGGATGAG
301 GTACACCTAC AGCTTACCAA GATGATAAAA GGAGCCACTC CTCCAAGGCT TATTGCAAAG
361 CCTGTTGCAA AAGATGCCAT TGAAATGGAG TACGTTTCTA AAAGAAAGAT GTACGATTAC
421 TTTTTAGGGC TTATAGAGGG TAGTTCTAAA TTTTTCAAGG AAGAAATTTC AGTGGAAGAG
481 GTCGAAAGAG GCGAAAAAGA TGGCTTTTCA AGGCTAAAAG TCAGGATAAA ATTTAAAAAC
541 CCCGTTTTTG AGTATAAGAA AAATGTCTGG GGAAAGATAC TGGGCTTTGG CTTTATAAGG
601 AGCAACTCTT TTAAACTTGC TTTATGGAGC TTTATCATAG GCTTTTTGGT GGTAGGATTT
661 GTATCTTCAT GGGACCTTCT AAAAAGCTTT TCTGGCGCAT TTATAATAGG AGCTTTTACG
721 TACATATTTT CTTATATTTT GAATATGCCT GCTAAGAATC TTCATGAATT TGTAAAAATC
781 ATGGGAAGCA GAAATTTAGA AGAGGAGTTT AAACTAGAAA GCGGTGACGT TTTTGAAGCT
841 ATTGCAGAGG AGTTAAACAG CGTAAAAGAT ACTATTAAGA AGGACATGCT GTTTTTAAAA
901 GGCGGCACAG ACGACATGCA CAATTTTGTT CACAGGTTTA ATGAGATTGC AGAGAACATG
961 AAGAAGGTGT CTGAAGATAT ATCTTCTGTG GTGAATGATG TAGCTTCTTC TACAGTTCAT
1021 CAGGCAGAAG AGATAGAAAG GGCTGTCGGA ATACTGGACG AAAATATAAA AAAGATAAAT
1081 GAGATTGCAG GAACTAGCAA GGAGAGCAAT GAAAAACTGG AAAATTCTAT AGAAAATATA
1141 AAAAGGGCAA ATACCGATGT AACAGATGTT GCCAAGGAAT TATCACAGGT AGAAGTGGAT
1201 TTTTCTAGTA TATATGAGAT GGGCAAGGTG CTTTCAGATA GCGCTAAAGA TATCATGGCA
1261 ATAGTCACTA CTGTAGAGGA AATTTCAGAT CAGACTAATT TGCTGGCGCT AAATGCGGCT
1321 ATTGAGGCGG CGAGGGCAGG AGAAGCAGGA AGAGGGTTTG CCGTGGTAGC AGAAGAGGTG
1381 AGGAATTTAG CTGAAAATTC GAAAAATGCG GTAAAGACCA TAACAGAAAG CTTAGTCAAT
1441 TTTACAGGTC AGGTGGAGAA TCTAGCAGAG AAGATAAGTG CCCAGTTTGA AAGGCTTAAA
1501 AAGAGCATTT CCACTCTGGA GAAGGTGGTA GAAAAAAATA CAATGGCTAC AGAAGAGGTT
1561 GCAGGGATAT CAAGCGTGAT AGTCGAATCT GCAAACAGGC TTTATGAAGA GGCAGAGAAG
1621 CTTTCAGAGG TCTTCGGACA CCTGGAAAAT CTGGCTGCTA TTTCAGAAGA GAATTCGGCT
1681 TCTTCTGAGG AAATGAGTGC CAATGTTACA GAGTATTCAA ACAGAATAAG GGAATTTATA
1741 GAGCAGATAA AGCAGATGGA GACACTTGTT ACAAACTTTA AGAAGGAGCT TGATAAATAC
1801 AAAGTTTGA

Figure A4. Gene sequence of the MCP protein that contains *Tt* H-NOX. *Tt* H-NOX gene includes the first 564 bases (encoding for 188 amino acids) that are colored in red.

Site-directed mutagenesis of *Tt* H-NOX

A number of point mutations were made to study the structure-function relationship of *Tt* H-NOX. The sense sequences of the primers used to make these mutants are listed in Table A1. The mutant P115A was generated using previously designed primers, and the double mutant M98C/P115A was made by using P115A primers and M98C plasmid.

Table A1. Sense sequence of the primers used to generate various *Tt* H-NOX mutants. The mutation sites are colored in red.

Mutation	Sense sequence for the primers
T4C	5' GAAGGGG**TGC**ATCGTCGGGACATGGATAAAGACCCTGAGGG 3'
F78A	5' GGAAGGCAGAACATAAAAACT**GCC**AGCGAATGGTTTCCCTCC 3'
F78V	5' GGAAGGCAGAACATAAAAACT**GTC**AGCGAATGGTTTCCCTCC 3'
F78Y	5' GGAAGGCAGAACATAAAAACT**TAC**AGCGAATGGTTTCCCTCC 3'
M98C	5' GGCTAGTGAATTTTTTAATGATG**TGC**GATGAGGTACACCTACAGCTTACC 3'
M98A	5' GGCTAGTGAATTTTTTAATGATG**GCG**GATGAGGTACACCTACAGCTTACC 3'
A112C	5' CCAAGATGATAAAAGGA**TGC**ACTCCTCCAAGGCTTATTGCAAAGCC 3'
P115F	5' GGAGCCACTCCT**TTC**AGGCTTATTGCAAAGCCTGTTGC 3'
L144A	5' GAAAGATGTACGATTACTTTTTAGGG**GCT**ATAGAGGGTAGTTC 3'

UV/visible Spectra of *Tt* H-NOX

UV/visible spectra for all ferrous and ferric complexes were collected for *Tt* H-NOX WT, M98C, M98A, A112C, P115A and P115A/M98C. The Soret and β/α bands are summarized in Table A2 and the spectra are shown in Figure A5-A8 (The UV/visible spectra for *Tt* H-NOX WT and P115A have been shown previously in Chapter 2, page 27).

Table A2. The Soret and β/α bands in the UV/visible spectra of *Tt* H-NOX complexes.

Tt H-NOX complex		Soret	β	A
WT	Fe(II)-unligated	431	560	
	Fe(II)-CO	424	545	568
	Fe(II)-NO	419	547	577
	Fe(II)-O_2	415	555	591
	Fe(III)-H_2O	415	552	587
	Fe(III)-CN^-	421	550	-
P115A	Fe(II)-unligated	431	561	
	Fe(II)-CO	423	544	568
	Fe(II)-NO	419	547	577
	Fe(II)-O_2	415	547	583
	Fe(III)-H_2O	405	545	581
	Fe(III)-CN^-	420	550	-
A112C	Fe(II)-unligated	432	564	
	Fe(II)-CO	424	544	569
	Fe(II)-NO	420	543	572
	Fe(II)-O_2	416	555	590
	Fe(III)-H_2O	410	548	592
	Fe(III)-CN^-	421	553	-
M98C	Fe(II)-unligated	434	560	
	Fe(II)-CO	423	541	570
	Fe(II)-NO	419	544	577
	Fe(II)-O_2	415	551	587
	Fe(III)-H_2O	412	542	579
	Fe(III)-CN^-	418	547	-
M98A	Fe(II)-unligated	434	564	
	Fe(II)-CO	423	543	571
	Fe(II)-NO	419	545	577
	Fe(II)-O_2	415	550	587
	Fe(III)-H_2O	413	541	575
	Fe(III)-CN^-	418	545	-
P115A/M98C	Fe(II)-unligated	432	562	
	Fe(II)-CO	423	540	569
	Fe(II)-NO	419	536	569
	Fe(II)-O_2	414	544	580
	Fe(III)-H_2O	401	542	578
	Fe(III)-CN^-	419	546	-

A112C

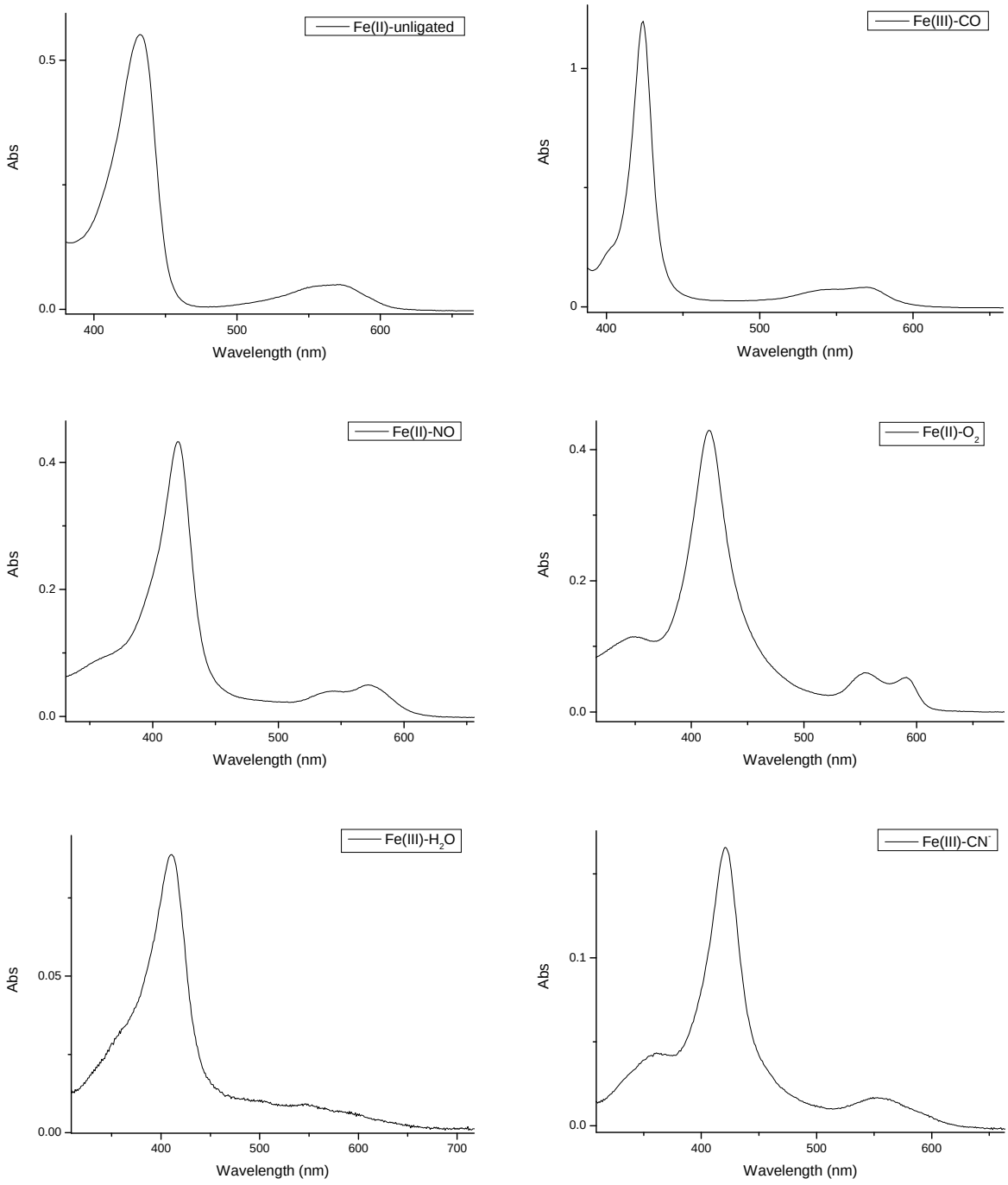

Figure A5. UV/visible spectra for *Tt* H-NOX A112C.

M98C

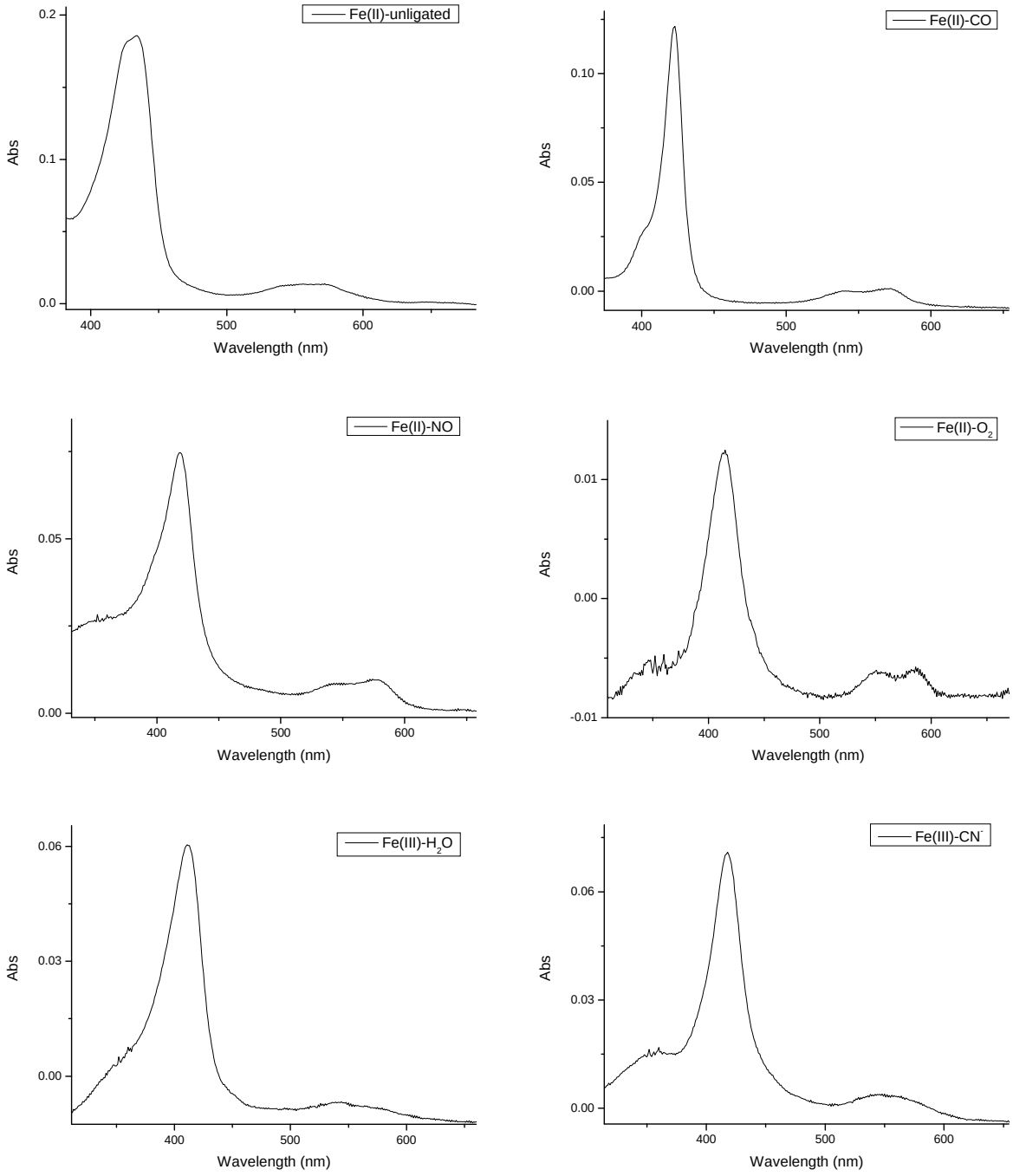

Figure A6. UV/visible spectra for *Tt* H-NOX M98C.

M98A

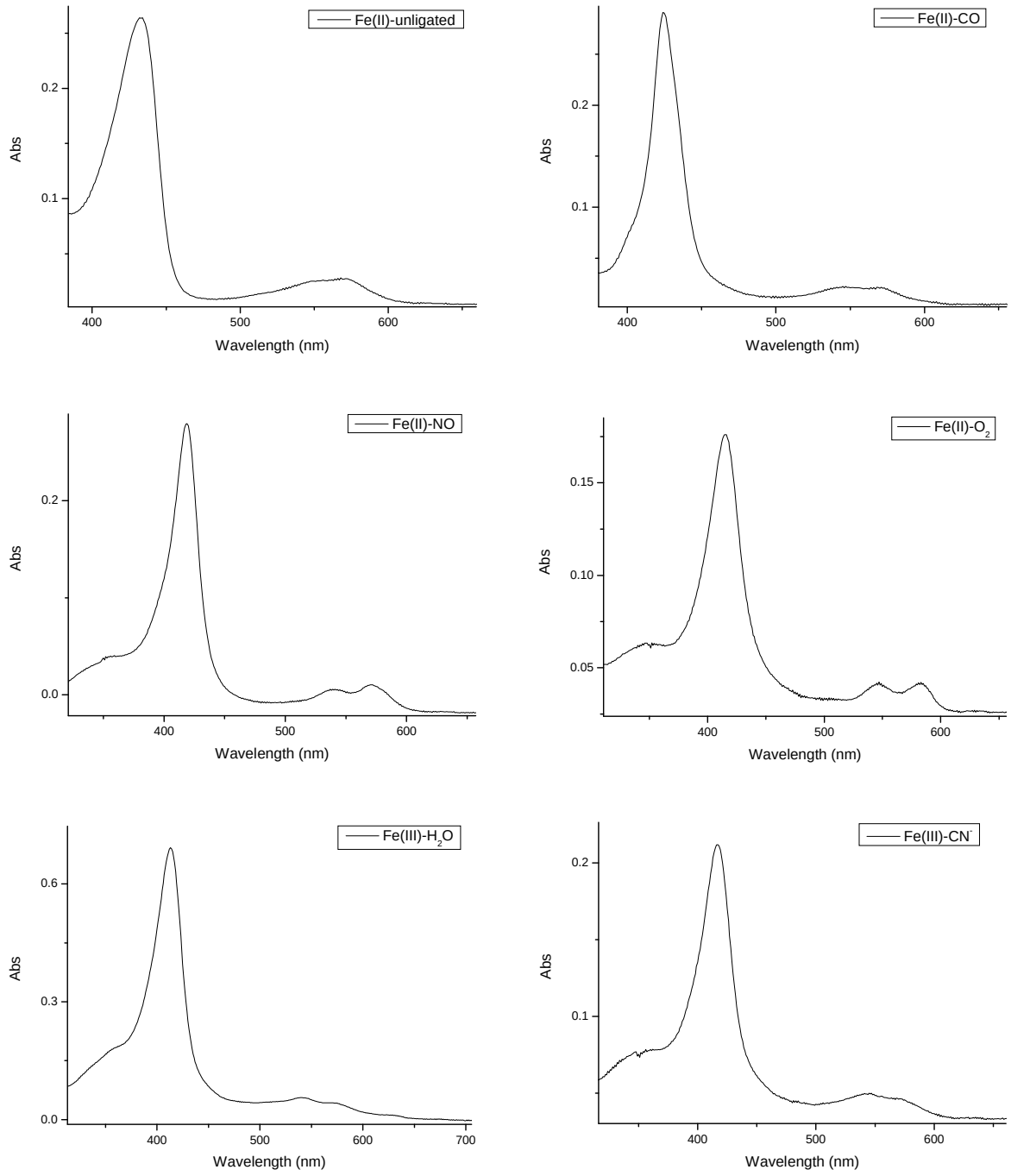

Figure A7. UV/visible spectra for *Tt* H-NOX M98A.

P115A/M98C

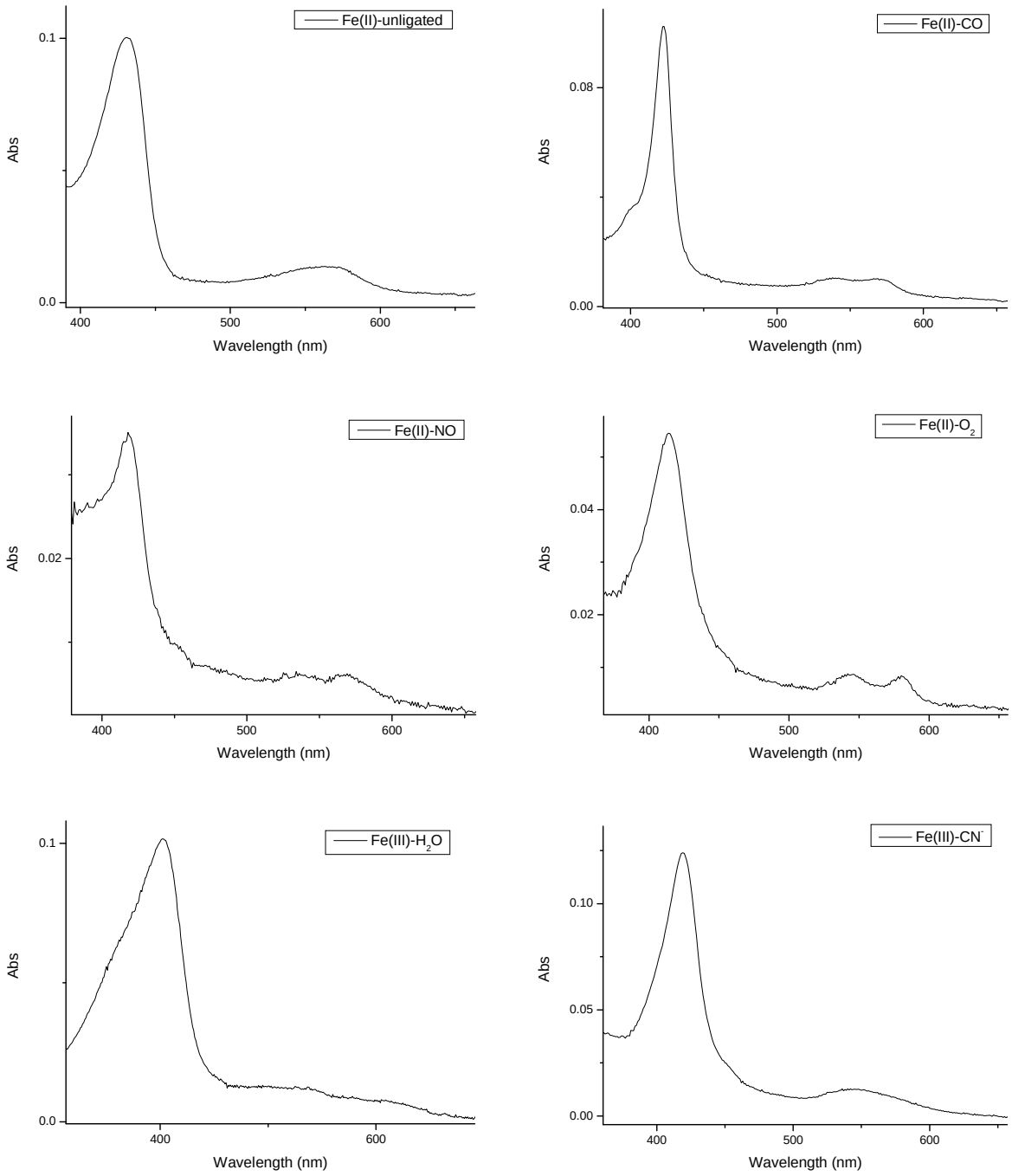

Figure A8. UV/visible spectra for *Tt* H-NOX P115A/M98C.

UV/visible spectra of the ferric complexes (-H_2O and -CN^-) for *Tt* H-NOX F78V, F78Y, P115F and L144A were also obtained. The Soret and β/α bands are summarized in Table A3 and the spectra are shown in Figure A9-A12.

Table A3. The Soret and β/α bands in the UV/visible spectra of *Tt* H-NOX ferric complexes.

Tt H-NOX complex		Soret	β	α
F78V	Fe(III)-H_2O	415	552	587
	Fe(III)-CN^-	420	550	-
F78Y	Fe(III)-H_2O	415	545	581
	Fe(III)-CN^-	420	550	-
P115F	Fe(III)-H_2O	411	544	582
	Fe(III)-CN^-	421	548	-
L144A	Fe(III)-H_2O	413	554	585
	Fe(III)-CN^-	419	552	-

F78V

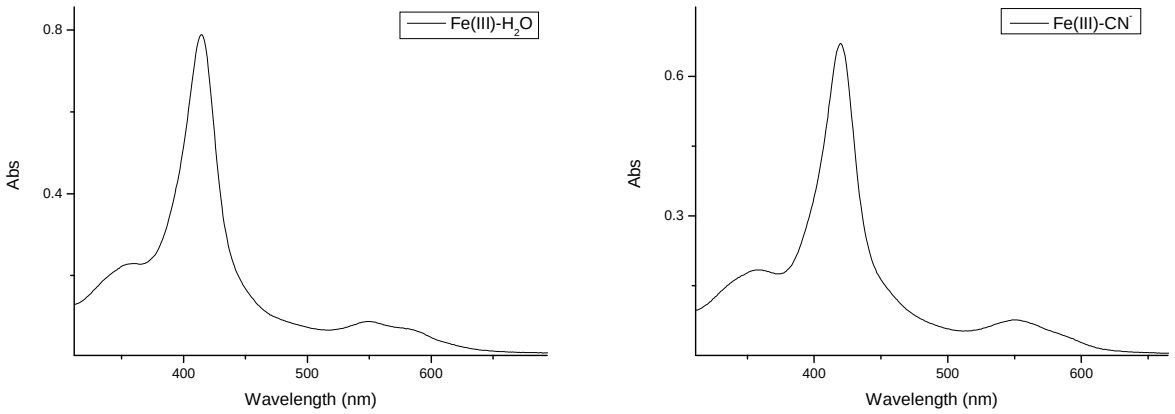

Figure A9. UV/visible spectra for *Tt* H-NOX F78V complexes.

F78Y

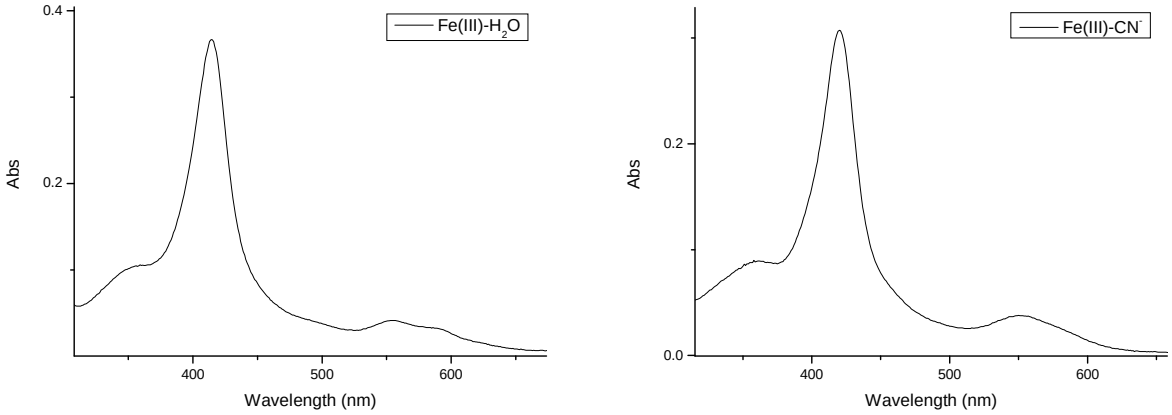

Figure A10. UV/visible spectra for *Tt* H-NOX F78Y ferric complexes.

P115F

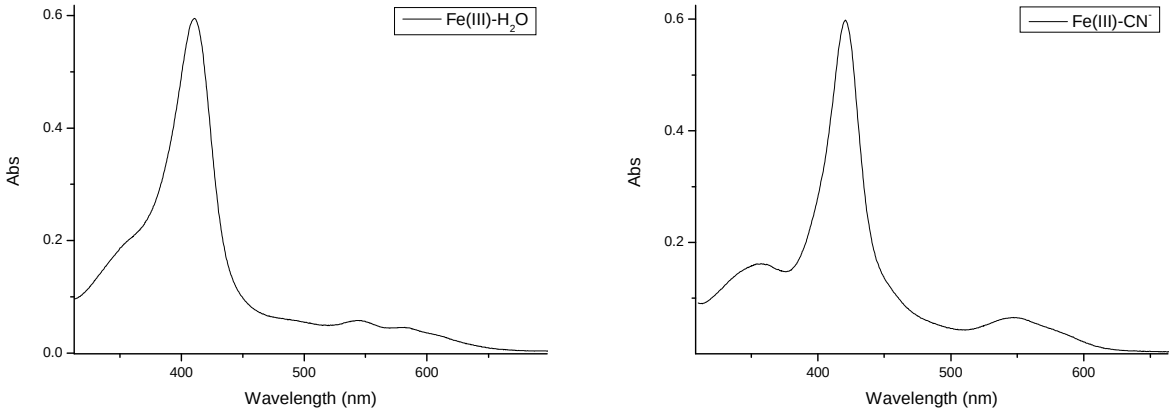

Figure A11. UV/visible spectra for *Tt* H-NOX P115F ferric complexes.

L144A

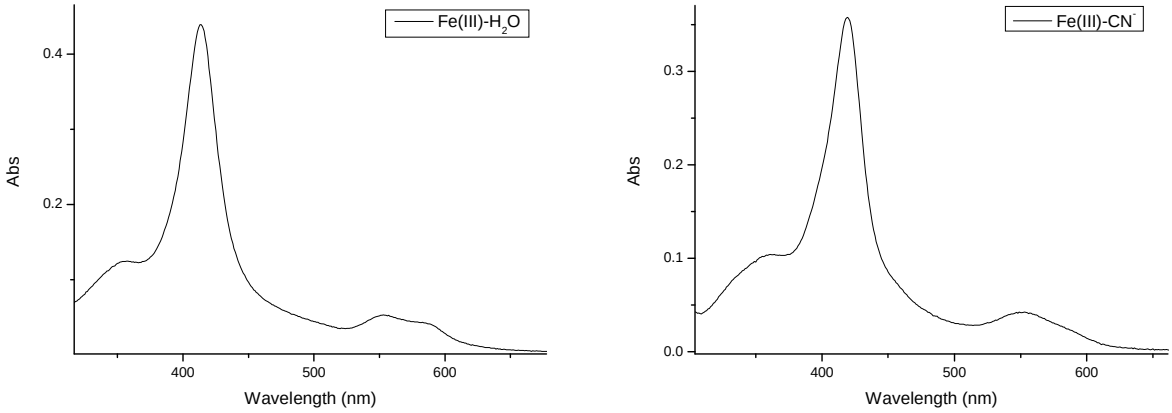

Figure A12. UV/visible spectra for *Tt* H-NOX L144A ferric complexes.